General Disclaimer

One or more of the Following Statements may affect this Document

- This document has been reproduced from the best copy furnished by the organizational source. It is being released in the interest of making available as much information as possible.
- This document may contain data, which exceeds the sheet parameters. It was furnished in this condition by the organizational source and is the best copy available.
- This document may contain tone-on-tone or color graphs, charts and/or pictures, which have been reproduced in black and white.
- This document is paginated as submitted by the original source.
- Portions of this document are not fully legible due to the historical nature of some of the material. However, it is the best reproduction available from the original submission.

Produced by the NASA Center for Aerospace Information (CASI)

48724

NSG-7527
NSG-7592

(NASA-CR-173561) HIGH RESOLUTION HARD X-RAY SPECTRA OF SOLAR AND COSMIC SOURCES Ph.D. Thesis (California Univ.) 118 p
HC A06/MF A01 CSCL 03B
N84-25587
Unclas
G3/93 13461

SPACE SCIENCES LABORATORY

JUN 1984
RECEIVED
NASA STI FACILITY
ACCESS DEPT.

HIGH RESOLUTION HARD X-RAY SPECTRA OF SOLAR AND COSMIC SOURCES

Richard Alan Schwartz

Department of Physics and Space Sciences Laboratory
University of California, Berkeley, California 94720

Ph.D. Dissertation

UNIVERSITY OF CALIFORNIA, BERKELEY

High Resolution Hard X-ray Spectra of Solar and Cosmic Sources

By

Richard Alan Schwartz

B.S. (Carnegie-Mellon University) 1974
M.S. (University of California) 1976

DISSERTATION

Submitted in partial satisfaction of the requirements for the degree of

DOCTOR OF PHILOSOPHY

in

Physics

in the

GRADUATE DIVISION

OF THE

UNIVERSITY OF CALIFORNIA, BERKELEY

Approved: Kinsey A. Anderson 12 April 1984
Chair Date
Jonathan Arons 12 April 1984
Stuart Bowyer 13 April 1984

High Resolution Hard X-ray Spectra of Solar and Cosmic Sources

Richard Alan Schwartz

Abstract

High resolution (~1 keV) hard X-ray (14-300 keV) observations of a large solar flare and the Crab Nebula were obtained during balloon flights on October 18, 1979 and June 27, 1980 using an array of cooled germanium planar detectors. In addition, high time resolution (.128 sec.) high sensitivity measurements were obtained with a 300 cm^2 NaI/CsI phoswich scintillator.

We find that the flare impulsive hard X-ray spectrum **cannot** be produced by thermal bremsstrahlung from a homogeneous Maxwellian electron distribution. Instead, the sequence of 2-20 second hard X-ray bursts over the 3-4 minute impulsive phase implies the acceleration of 10->200 keV electrons by as many as three mechanisms. Below ~30 keV the acceleration varies gradually (20-40 sec.), from ~30-120 keV the acceleration varies rapidly (1-5 sec.), and above 120 keV there is a second-step acceleration which produces a 1-2 second X-ray delay. No more than 1% of these electrons could be accelerated prior to the impulsive phase. Also, repeated low intensity hard X-ray spikes were observed for an additional 13 minutes indicating that electron acceleration continues well past the impulsive phase.

While the impulsive hard X-ray flux seems to be of non-thermal origin, this experiment also discovered a steep super-hot component of the flare hard X-ray spectrum at energies below 35 keV. The spectrum fits closely to that from a Maxwellian electron distribution with a maximum temperature of ~35×10^{6}°K and a peak emission measure of ~$5 \times 10^{48}\,\mathrm{cm}^{-3}$. This emission appears to come from a dense plasma ($n > 10^{12}\,\mathrm{cm}^{-3}$) occupying filamentary loops of total cross-section ~$10^{15}\,\mathrm{cm}^2$ and length ~2.6×10^{9}cm. The super-hot filaments exist in addition to loops with the $10\text{-}20 \times 10^{6}$°K peak temperature characteristic of the usual soft X-ray flare

plasma.

The Crab spectrum from both flights was searched without finding evidence of line emission below 200 keV. In particular, for the 73 keV line previously reported we obtain a 3σ upper limit for a narrow (1 keV FWHM) line of 1.9×10^{-3} and $1.4 \times 10^{-3}\,\mathrm{ph\,cm^{-2}\,sec^{-1}}$ for the 1979 and 1980 flights, respectively.

Acknowledgments

I would like to thank my advisors, Prof. Kinsey Anderson and Dr. Robert Lin, for the time they put into getting this document and me out. I thank Dr. Robert Rosner for sharing some of his insight on coronal loops. I thank the other members of my thesis committee, Professors Arons and Bowyer, for taking the time to read my manuscript. I also give great thanks to my scientific collaborators on this project, Drs. Kevin Hurley, R. Michael Pelling, and Taeil Bai. I also thank Dr. S. R. Kane for the use of the ISEE-3 data. I thank Dr. William Lotko and Dr. John Wygant for their scientific input.

I thank Henry Primbsch, Fred Duttweiller, Rod Jerde, Paul Brissendon, and Pete James for their assistance with the balloon instrumentation and flight operations. I also thank D. Atkinson and W. Mote who provided assistance on the June 1980 flight via the University Expeditions Research Program. I also thank the flight crew at NSBF for two productive safe launches.

My special gratitude goes to the germanium detector group at LBL, Fred Goulding, Dick Pehl, Norm Madden, Don Landis, Gene Haller, Don Malone, Paul Luke, and Chris Cork. They and Henry Primbsch are responsible for an instrument which truly leads the field. I must also thank our skilled technical staff at SSL, Roland and Chris Schultz and Ron Herman, for their work on the flight systems. We also received great help in our metal shop from George, Art, Orlanda, and John.

Great thanks go to Ron Toy, Marge Currie, and Frances Cotter for help with some of the art and paper work. Thanks also go to Theda Crawford, Carolyn Overhoff, and Mary Ann Finnerty for UNIX assistance. I am pleased to have worked with Josh Roth, Jo Pitesky, Steve Wright, John Simmons, and Greg Jung. Muchas gracias Ruth for sending me unerringly on so many journeys.

Of course I cannot thank my family and friends enough for their forbearance during my years here in Berkeley.

This work was supported by the grants NSF/ATM-8119543, NSG 7527, NSG 7592, NGL 05-003-017, and NSF/ATM 79-24559.

Table of Contents

1: Introduction 1

2: Instrumentation 5

3: Flare Electron Acceleration 27

4: Super-Hot Component 67

5: Summary of Flare Results 89

6: Search for the 73 keV Line from the Crab Nebula 93

References 107

ONE

Introduction

Hard X-ray and gamma-ray observations in the ~10 keV to ~1 MeV range have shown that explosive and non-thermal processes commonly occur in the universe. The high resolution spectroscopic measurements which may be obtained with cooled germanium detectors can provide one important means for understanding the fundamental physical processes occurring in the source objects. The precise measurement of the continuum spectra of hard X-ray sources can give detailed information about the emission process and about physical conditions in the emitting region. Continuum spectra characteristic of thermal sources are often so steep as to be unresolvable by scintillation detectors [*Kane and Hudson* 1970, *Lin et al.,* 1981]. Furthermore, a very important practical advantage of the superior energy resolution of germanium detectors is that the source spectrum can be determined uniquely without *a priori* assumption of a spectral model [*Fenimore et al.,* 1982]. Emission lines and narrow absorption features in this energy range are expected from the radioactive decay products of nucleosynthesis, from cyclotron line emission and absorption in the strong magnetic fields of neutron stars, from positron annihilation, and from the collisional excitation of nuclei by cosmic rays.

During a solar flare, from 10^{29} to 10^{32} ergs are released over a time scale of ~10-100 seconds. The energy is believed to be stored in the twisted magnetic field of a solar active region and released through magnetic reconnection in the lower solar corona [*see reviews by*

Svestka 1976, *Kahler et al.* 1980, *Van Hoven et al.* 1980]. A wide range of phenomena may occur during a flare including electromagnetic radiation (ranging from ~10^8–10^{21} Hz), mass motion, particle acceleration, and plasma heating. Of particular interest is the rapid acceleration of large numbers of electrons to energies of 10 to greater than 100 keV. These fast electrons may lose almost all of their energy in collisions with the ambient electrons ($kT << E_e$) while less than .01% of their initial energy would be lost to X-ray producing electron-ion collisions. Under this *non-thermal* interpretation of the hard X-ray emission, the fast electrons carry the bulk of the flare energy [*Lin and Hudson* 1976, *Kane et al.* 1980]. Furthermore, most of the flare phenomena may be understood as resulting from the interaction of these energetic electrons with the solar atmosphere. These fast electrons may be one of the first detectable products of the energy conversion process. Although these electrons cannot be studied *in situ*, the instantaneous electron and hard X-ray spectra are closely related by the Bethe-Heitler bremsstrahlung cross-section. Also, since these X-rays propagate freely through the tenuous overlying solar atmosphere, they are an excellent diagnostic of the electron spectrum in the hard X-ray production region.

The shape of the hard X-ray spectrum is one key to the understanding of the role played by the fast electrons. For example, if the fast electrons can be contained and isolated from the ambient electrons, then the collisions between the fast electrons will only exchange energy within the very hot plasma [*Anderson* 1972, *Smith and Lilliequist* 1979]. Then, radiative losses would dominate, implying that far fewer fast electrons produce the same hard X-ray flux. If this *thermal* interpretation is correct, then the fast electrons would play a much less important role in the flare energy transfer process. Measurements of flare hard X-ray spectra by high resolution germanium detectors can determine whether a spectrum was produced by a single temperature (10^8–10^9°K) plasma. High time resolution is also important because the hard X-rays are produced during a series of bursts which rise and fall on a time scale of a few tenths to a few tens of seconds. Moreover, during these bursts, the spectrum shows a soft-hard-soft evolution. Such temporal evolution is controlled by the competition between the loss and injection of the electrons in the X-ray production region.

On June 27, 1980 we observed a large solar flare in hard X-rays (~15-300 keV) using a balloon-borne germanium spectrometer and a large area phoswich scintillator. In particular we show that the hard X-ray spectrum **cannot** be produced by a single temperature plasma contrary to the conclusions of *Matzler et al.* [1978], *Elcan* [1978], and *Crannell et al.* [1978]. Also, the fast electron lifetime appears to be so short that the evolution of the hard X-ray spectrum is dominated by the acceleration/injection of the energetic electrons. Thus, from the X-ray time profiles, we are able to determine that there may be as many as three electron acceleration mechanisms operating during the flare. The acceleration of electrons up to over 100 keV appears to be very rapid, perhaps taking only a fraction of a second. Conceivably, there are two acceleration processes operating below 100 keV. The number of electrons below 30 keV seems to vary gradually, while at higher energies the number of electrons varies on a much more rapid timescale. We find that this temporal evolution may be interpreted by the superposition of many 'elementary' bursts [*de Jager and de Jonge* 1978] with a soft-hard-soft spectral evolution, or by the combination of a *gradual* (varying over several tens of seconds) acceleration mechanism at low ($E \lesssim 30$keV) and a *rapid* (varying over ~1-5 seconds) acceleration mechanism at higher ($E \gtrsim 30$keV) energies. Also, we have found that electron acceleration continues at a low level for almost 1000 seconds after the end of the main impulsive phase. The third acceleration mechanism appears to be a delayed second-step process which further accelerates the energetic electrons up to several hundred keV and higher. This same mechanism may also rapidly accelerate protons to tens of MeV's in this and other flares [*Bai and Dennis* 1983].

Since the fast electrons seem to carry much of the flare energy they should heat the solar plasma as they lose energy in electron-electron Coulomb collisions. During this flare, spacecraft instruments observed the ususal 10-20 $\times 10^{6\circ}$K soft X-ray plasma, but in addition, we discovered a new super-hot component of the thermal flare plasma with a temperature of $\sim 35 \times 10^{6}$°K and an electron density which may be as high as $10^{12}\,\mathrm{cm}^{-3}$ [*Lin et al.* 1981]. The steep X-ray spectrum from the super-hot component is unresolvable by scintillation detectors. It seems most likely that this super-hot component plasma is found on field lines with a very high level of energy release.

We have also observed the Crab during both the June 27, 1980 flight and during a flight on October 18, 1979 to search for the 73 keV line emission reported by *Ling et al.* [1979]. This line, if real, may be another instance of quantized cyclotron emission in the intense, $B > 10^{12}$ gauss, magnetic field of a neutron star as presumed for Her X-1 [*Trümper et al.* 1978]. This null observation is consistent, however, with the interpretation that this line is strongly produced only in transient bursts.

The chapters are organized as follows: Chapter 2 is a description of the high resolution germanium spectrometer. It has achieved the best resolution, (<700 eV FWHM) of any hard X-ray detector flown to date. A brief description is included of the remaining instrumentation in the balloon payload. Chapters 3,4, and 5 describe the observation of and results from the solar flare hard X-ray burst. Chapter 3 examines the acceleration of the electrons; Chapter 4 discusses the evolution of the new super-hot component, and Chapter 5 links the non-thermal and thermal results together in a summary which describes the relationship of this thesis to other work in the field. Chapter 6 discusses our search for 73 keV line emission in the Crab pulsed and unpulsed spectra.

TWO

Instrumentation

2-A. Instrument Description

In 1979 we began development of a high resolution instrument for hard X-ray spectroscopy. The instrument consists of an array of four ~4 cm diameter × 1.3 cm thick hyperpure planar germanium detectors, cooled by liquid nitrogen and housed within an aluminum vacuum cryostat. In turn this is surrounded by active anti-coincidence scintillator shields. State of the art electronics, including cooled FET preamplifiers with pulsed charge feedback, were used to give an in-flight energy resolution of better than .7 keV FWHM (full width at half maximum) at 50 keV, the best achieved to date for astrophysical instrumentation. This instrument has been flown, along with a 300 cm^2 NaI/CsI phoswich scintillation hard X-ray detector, on two successful balloon flights, one in October, 1979, the second in June, 1980. The scientific targets on the first flight were the Crab Nebula, the supernova remnant Cas A, and the Seyfert galaxy Markaryan 421. The primary target of the second flight was the Sun; several solar hard X-ray bursts, including one very intense flare, were observed. The Crab Nebula was also observed during this flight. Two more flights were launched from Brazil in spring and fall, 1982. Improvements have been made to the instrument based on the experience gained from each flight

Germanium Detector

The detectors are fabricated from *p* type germanium: one face is an n^+ diffused lithium positive high voltage contact, while the other face is a p^+ boron implant signal contact. They are operated as reverse biased diodes with their volumes fully depleted of free carriers and with a field strength of ~1 kV/cm. The detectors are held in boron nitride cups with pressure-loaded indium pads (these pads make the electrical contact to the detector), and are housed in separate aluminum modules for isolation. These sit within an aluminum vacuum cryostat, as shown in Figure 2-1. The detectors are cooled to 95°K with liquid nitrogen. The liquid nitrogen coolant is kept at 12 p.s.i. over the ambient pressure by venting the boiloff gas through a relief valve. Photons enter through a 0.06" thick × 4.5" diameter beryllium window, and pass through 4 cm diameter holes in the cold plate to enter the detectors through their boron implant side.

Shields and Collimator

The active anti-coincidence shield is a modification of a balloon-borne cosmic x-ray experiment designed, built, and flown by Space Sciences Laboratory and C. E. S. R. Toulouse [*Hurley and Duprat,* 1977; *Anderson and Mahoney,* 1974; *Mahoney,* 1974]. The active shield has three parts. The phoswich shield is a central 5 inch diameter × 1/4 inch thick NaI (Tl) scintillator optically coupled to a 5 inch diameter × 2 inch thick CsI (Na) scintillator; a single photomultiplier tube (PMT) views both. The annular shield, a 9 inch outer diameter × 2 1/4 inch long annulus of CsI (Na) viewed by 6 PMT's, surrounds the phoswich crystal. In front of these is the collimator shield with an 8 inch outer diameter and 5 inch inner diameter × 2 inch thick of CsI (Na) viewed by 4 PMT's. All of the shield lower level discriminators are set to ~30 keV. A shield event triggers a 14 μ sec logic signal used for anti-coincidence.

Passive shields are used within the cryostat. Figure 2-2 shows the location of the 0.125 inch thick tantalum shields covered mostly by 0.013 inch of molybdenum to prevent tantalum fluorescent x-rays from reaching the germanium detectors. Indium is used between the Ta cold plate shield and the detector modules to provide good thermal contact and as X-ray shielding. Surrounding the cryostat feedthrough ring and directly above the active shields there is an additional annular shield of 0.125 inch lead.

The graded z slat collimator is made from three 10.1 cm long sections, each consisting of eleven 0.7 mm thick plates, spaced by 1 cm. The plates are of 0.1 mm Ta, covered on both sides by 0.3 mm tin flashed with copper. The collimator walls are lined with 2 mm of lead. Two collimator sections are stacked to define a 2.8° FWHM elevation angle field of view (FOV), while a single orthogonal section defines the 5.6° FWHM cross-elevation angle FOV. Figure 2-3 shows the germanium instrument's collimator transmission as a function of elevation offset angle. Even at zero offset angle, the finite slat thickness reduces the transmission to 85%. The transmission of photons above 300 keV is not zero at offset angles $>2.8°$ because the total cross-section becomes small enough that some photons can pass unscattered and unabsorbed through a line of sight plate thickness of $\sim$0.7 mm/sin 2.6°.

Detector Electronics

Each of the four germanium detectors has an independent signal chain, including a preamplifier, dual shaping amplifiers, pulse stretcher, active baseline restorer, and a 4096 channel pulse height analyzer (PHA). An electronic block diagram is shown in Figure 2-4. Each detector is D.C. coupled to a low noise ($\sim$500 eV FWHM), charge-sensitive preamplifier whose first stage is a Solitron 310 FET operating at $\sim$150°K mounted within the detector module. A key element of the low noise electronics is the pulsed charge feedback reset system [*Landis et al.*, 1982]. During reset, which occurs $\sim$10 times a second, the signal processing electronics are disabled for $\sim$200 μ sec.

The output from the preamplifier goes into dual shaping amplifiers. The slow shaper-amplifier-discriminator ($\sim$10 μsec shaping time) converts the preamplifier signal into a unipolar pulse. The peak is detected and converted to a 12 bit PHA word by a run-down Wilkinson-type analog to digital converter for which a full scale event takes 1 millisecond. The fast shaper-amplifier-discriminator (~400 nsec shaping time) gives fast pulses for detector-detector coincidence, pile-up rejection, timing, and rate accumulations. This dual fast/slow amplifier system, together with the active baseline restorer, allows for single detector count rates in excess of 20,000 counts/second without spectral distortion.

The bias voltage for each germanium detector is supplied through one of four separate high voltage filter boxes, powered in pairs by two separately commandable (on/off only) high voltage supplies. Each detector also has a separately commandable pulse generator. Approximately every three hours during an observation, they are turned on for several minutes with a ~20/second pulse rate for electronic calibration.

Digital Electronics

Each detector event is encoded into the telemetry stream in a 20 bit word, 12 bits for the PHA, 2 bits for the detector identification, 4 bits for fine timing to 0.5 millisecond, 1 bit for pair detector coincidence, and 1 bit for shield coincidence. Those Compton events which trigger two detectors set the pair detector coincidence bit. There are two commandable modes for detector shield anti-coincidence. In one mode, all detector events are analyzed and encoded with the shield coincidence bit either set or null. In the "shield veto enable" mode, the shield logic signal inhibits the PHA's from analyzing any shield coincident events. Polling logic queries each detector's signal ready flip-flop in turn for the next event to encode into the telemetry. The telemetry system can handle up to 500 total germanium detector events/second.

Scintillator events, fast rate scalars, slow rate scalars, and gondola status words are also transmitted. The 16 ten bit fast rate scalars, read out every 0.128 sec., accumulate separately each detector's valid event rate both in coincidence (4 rates) and in anti-coincidence (4 rates) with the active shields, the 3 anti-coincidence shields' rates, and the scintillator's rates over 5 energy ranges 22-33, 33-60, 60-120, 120-235, and >235 keV.

The slow rates, each read out every 8.192 seconds, include each germanium detector's live time and reset rate. During the time a detector's signal chain is available, a 128 kHz crystal oscillator advances its live time counter. Thus, the live time fraction is that count divided by $2^{20} - 1$. The detector reset rates can be replaced by the pair detector coincidence rates on command.

Burst Memory

A burst memory was installed before the June, 1980 flight to store the total germanium detector event rate and the 3 lowest energy scintillator rates. After automatically triggering on an elevated scintillator rate, the memory stores these four fast rates every 8 milliseconds, until the memory is half full, then for 32 msec until filled. This accumulates ~5 minutes of high time resolution rate data in 65,536 10 bit words. Then on command, the memory is read out in 65 seconds, replacing the normal germanium detector telemetry.

Tracking System

The gondola uses an alt-azimuth pointing system referenced to gravitational vertical and the local magnetic field direction. The balloon payload rotates beneath a field aligned magnetometer table to the target azimuth computed on the ground and sent up periodically by command as the balloon changes latitude and longitude. Concurrently, the thermally insulated instrument cage housing the germanium instrument and coaligned phoswich scintillator is rotated to the computed elevation angle. The pointing system automatically tracks a source in between ground commands, which are sent every 15 to 30 minutes.

2-B. Instrument Performance

Efficiency

A photon, energy E_1, normally incident on the detector's front surface, can lose some or all of its energy to the detector by the photoelectric effect or by Compton scattering. For low-energy X-rays, some of this energy can escape the detector by fluorescent X-ray emission. The detector response $r\ (E_2, E_1)$, where E_2 is the pulse height energy, was computed using a Monte Carlo program, which followed the photon until it was either totally absorbed or scattered beyond the active shield. The calculated absolute photoefficiency and the measured relative efficiency are shown in Figure 2-5. The Monte Carlo calculation showed that the shield almost completely suppresses the Compton continuum under 200 keV.

The escape peak response may be computed directly. Consider a low-energy photon which stops in the detector. The ejected K shell photoelectron gives up its energy by elastic scattering to create an electron-hole charge cloud. Then the atom decays, either by emission of another energetic electron in an Auger process, or by the fluorescent emission of a photon at 9.87 or 10.98 keV [*et al.*, 1978]. If the original photon stopped near the front surface of the detector, there is a good probability of the fluorescent X-ray escaping the detector volume, resulting in a pulse height event at the escape peak energy. The probability for escape is given by

$$P\ (E_1, E_2) = (W_2/2)\left\{1 - z\ \log[(1+z)/z]\right\} \qquad (2\text{-}1)$$

where E_1 is the incident photon energy; E_2 is the escape X-ray energy; z is a dimensionless number defined to be $\mu_{PE}\ (E_2)/\mu_{PE}\ (E_1)$, [where $\mu_{PE} =$ photoelectric x-section]; and W_2 is the probability of X-ray emission at E_2. For example, for an incident photon $E_1 =$ 20 keV, the probability of K escape is the sum of $P(20, 9.87) = 7.7\%$ and $P(20, 10.98) = 1.3\%$, for a total of 9.0%.

Two problems modified the germanium detector response during the October, 1979 flight. All four detectors had ~ 220 micron dead layers, which are undepleted front surfaces (regions of low electric field), due to the diffusion of the lithium of the front surface contact. Charge, from ionizing events in the dead layer, has a high probability of recombination before moving into the high field region. The resultant pulse height spectrum has a reduced photopeak and a low energy tail. Only events which actually occur in the dead layer are affected; at 60 keV 80% of the photons will pass through to stop in the fully depleted region. Also, one of the detectors had surface channels [*Haller*, 1982] which cause poor field line geometry; the field lines in the 0.3 cm outer edge of the back contact connected to the side of the detector instead of to the front surface. (The field line geometry was estimated after scanning across the back surface of the detector with a collimated ~60 keV line source. If the X-rays were incident on a region connected by the field lines to the front surface, then the pulse-height response would be at 60 keV.) Charge created in this region moved to the sides where it recombined more readily and was lost from the output current pulse. This resulted in a photopeak efficiency reduced by about 30% for higher energies with a very flat low energy tail. Both of these effects have been modeled and incorporated into a matrix deconvolution routine for the October, 1979 data. Subsequently, we were able to reverse the polarity of our detectors by using a newly developed pulsed reset circuit [*Landis et al.*, 1982], which made the lithium contact the detector back surface. The surface channels did not reappear in the detectors of the modified instrument.

Background, Resolution, Stability, and Linearity

Figure 2-6 shows the background spectrum from 11 to 585 keV during the June, 1980 flight rate from Palestine, Texas. This spectrum is the summed output of all four germanium detectors for a 12,500 seconds' accumulation from 15:30 - 21:00 UT. Most of the observed background lines are listed in

Principal Background Lines at Float	
Energy	Source
23.5 keV	Neutron Activation ^{70}Ge (n,γ) ^{71}Ge^{m}
53.4 keV	Neutron Activation ^{72}Ge (n,γ) ^{73}Ge^{m}
56.3 keV	Ta $K_{\alpha 2}$
57.5 keV	Ta $K_{\alpha 1}$
65.2 keV	Ta K_{β}
66.7 keV	Neutron Activation ^{72}Ge (n,γ) ^{73}Ge^{m}
72.8 and 75.0 keV	Radioactive Cryostat Impurity Pb $K_{\alpha 2}$ and $K_{\alpha 1}$
74.8 and 77.1 keV	Radioactive Cryostat Impurity Bi $K_{\alpha 2}$ and $K_{\alpha 1}$
84.7 keV	Radioactive Cryostat Impurity Pb K_{β}
87.1 keV	Radioactive Cryostat Impurity Bi K_{β}
90 and 93.4 keV	Radioactive Cryostat Impurity Th $K_{\alpha 2}$ and $K_{\alpha 1}$
139.7 keV	Neutron Activation ^{74}Ge (n,γ) ^{75}Ge^{m}
199 keV	Neutron Activation ^{70}Ge (n,γ) ^{71}Ge^{m}
238.6 keV	Radioactive Cryostat Impurity ^{212} Pb
511 keV	Electron-Positron Annihilation

Sources of Principal Background Lines at Float The radioactive cryostat impurity was found in the aluminum detector modules. These lines are characteristic of the Thorium decay chain. Many of the lines from 70 to 95 keV are due to the abnormally high radioactive contamination of the aluminum detector modules. For the spring, 1982 flight, new aluminum modules were fabricated with less than 1% of these contamination levels.

An advantage of the dual fast-slow amplifier/pileup rejection system is that it reduces the background due to the decay of 73 Ge^{m}, which is mainly produced by the neutron activation of 72 Ge. 73 Ge^{m} decays by emitting a 54 keV photon, followed in 2.9 μsec by emission at 13.3 keV of either a photon or a conversion electron (Figure 2-7). This event triggers the fast discriminator threshold set at $\sim$11 keV; this second trigger, if within 30 μsec, will cause the entire decay event to be rejected as pile-up. Figure 2-8 shows the effectiveness of this technique in a spectrum taken from the June, 1980 flight, which shows the spectrum of germanium detector 3 (fast discriminator threshold $\sim$11 keV) versus the spectrum of germanium detector

4 (fast discriminator threshold ~20 keV).

For a germanium detector, the energy resolution is the sum of two components: an energy independent component, due to electronic noise, and an energy dependent component, due to the statistics of the charge collection process within the germanium crystal:

$$FWHM(E) = \sqrt{FWHM^2_{electronic} + (2.35)^2 \epsilon \, F E} \qquad (2\text{-}2)$$

Here ϵ is the average energy needed to create an electron-hole pair (2.63 eV) and F is the Fano factor (~0.12). Initially, three of the germanium detectors had 700 eV FWHM electronic resolution; however, all of these detectors' electronic noise levels increased to 1 keV FWHM by the time of the flight. This increase appeared to be due to slow deterioration of the detectors' electronic ground integrity because of the increase in the cryostat-preamplifier contact resistance which developed in the humid pre-flight conditions in Texas.

Line Sensitivity

The minimum flux, Φ_l (photons/(cm^2/sec)), detectable from a narrow line at the level of n standard deviations (σ) is given by [*Willet et al.*, 1978]

$$\Phi_l = \frac{1.30\, n}{p_T} \left[\frac{\Delta E}{A} \left(\frac{R_s}{T_s} + \frac{R_B}{T_B} \right) \right]^{1/2} \qquad (2\text{-}3)$$

where p_T is the probability that a photon incident at the top of the atmosphere causes a photopeak event; ΔE is the energy resolution in keV (FWHM); T_s and T_B are the source and background observing times; and R_s and R_B are the source and background rates (counts/cm^2 sec keV). Figure 2-9 shows the 3σ sensitivity for the June 27, 1980 Crab Observation (T_s = 6076 sec and T_B = 4571 sec).

Total Performance

In Figure 2-10 we see the previously discussed detection efficiency and energy resolution together with the transmission functions for photons through the atmosphere at 3 g/cm^2 and the 50 mil Be window. The 3σ line sensitivity for a narrow line was computed for a narrow line for 10^4 sec on source and 10^4 sec on background. For comparison, the spectra of Her X-1, the Crab, and a typical several-per-day-occurence solar flare are shown.

2-C. Spectral Analysis

The X-ray flux from an astrophysical object is modulated by pointing the telescope alternately at the source and then at a source free background location on the sky. Typically, a single observation of a source or background location lasts for about 20 minutes; an entire observation of a cosmic source lasts for 4 - 6 hours. The counting rate (counts/sec) in a detector channel i due to a source is given by:

$$C_i = \int_{E_i}^{E_{i+1}} dE_3 \int_0^{\infty} g(E_2, E_3) dE_2 \int_0^{\infty} A \; r(E_2, E_1) \, f(E_1) \, t \, (E_1) \, \Phi(E_1) \, dE_1 \qquad (2\text{-}4)$$

where $\Phi(E_1) =$ source flux at the top of the atmosphere (photons $\mathrm{cm}^{-2}\,\mathrm{sec}^{-1}\,\mathrm{keV}^{-1}$), $t\,(E_1) =$ probability of transmission through the atmosphere and overlying materials, $f(E_1) =$ collimator transmission, $r(E_2, E_1) =$ probability of an energy loss E_2 for an incident photon of energy E_1, $A =$ detector area, and $g\,(E_2, E_3) =$ pulse height shape for an energy loss E_2.

To solve for the source flux Φ incident on the atmosphere, the first step is to convert the integral equation ((2-4)) into an algebraic equation. The narrow field of view of the collimator effectively eliminates any contribution from source flux scattered by the atmosphere. The active shielding rejects almost all of the partial energy Compton scatter events which would otherwise mimic lower energy source photons. The response simplifies to delta functions at the photopeak and at the escape peaks. The observed counting rates are essentially unbroadened by the convolution with $g(E_2, E_3)$ because the FWHM of 1 keV is less than the scale size of the variations of the detector incident flux. Since only fluorescent X-ray escape contributes non-diagonal matrix elements connecting photon and pulse height spectral energies, thus, above 30 keV, the integral equation reduces to

$$C_i = \Delta EA \; r_1 \, f \, t \, \Phi \Big|_{E_i} \tag{2-5}$$

where $\Delta E = E_{i+1} - E_i$ and r_1 is the photopeak efficiency (includes all full energy loss events) where r_1 and t are evaluated at E_i. Including the X-ray escape (showing only the 9.87 keV term to simplify the expression) we have

$$C_i = \Delta EA \; f \left[r_1 \, t \, \Phi \Big|_{E_i} + r_1 \, t \, \Phi \, P_{9.87} \Big|_{E_i + 9.87} \right] \tag{2-6}$$

Above 30 keV the source flux is obtained from

$$\Phi_i = C_i / (\Delta EAf \; r_1 \, t)$$

At lower energies the solution for Φ_i is obtained by starting at $E_i = 30$ keV and recursively solving the equation

$$\Phi_i = C_i - \Delta EA \; f \frac{(r_1 \, t \, \Phi \, P_{9.87}) \Big|_{E_i + 9.87}}{\Delta EA \; f r_1 \, t \Big|_{E_i}} \tag{2-7}$$

Thus, source photon spectra may be determined uniquely by directly inverting the background subtracted source spectra. Any narrow spectral lines which would be broadened instrumentally can be fit to determine their intrinsic parameters. This is in contrast to scintillation detectors, where a candidate source spectra is chosen *a priori* and convolved through the response matrix and then compared with the observed count rates.

Figure Captions

Figure 2-1 Vacuum cryostat housing germanium detectors.

Figure 2-2 Inside of the cryostat showing shields and germanium crystals.

Figure 2-3 Aperture response computed for the collimator at low and high energy.

Figure 2-4 Block diagram of electronic signal chain showing the principal functional units.

Figure 2-5 Calculated absolute photoefficiency of the germanium spectrometer and the measured relative efficiency.

Figure 2-6 Background spectrum accumulated over 12,500 seconds during June 27, 1980 flight in Palestine, Texas. The two sharp lines near 75 keV are separated by 2 keV from peak to peak which shows the excellent detector stability and high resolution. This spectrum is the sum of the output of all four crystals.

Figure 2-7 Decay scheme for 73 Ge^m.

Figure 2-8 The spectra from detectors 3 and 4 during June 27, 1980 flight showing effectiveness of the pile-up rejection technique for both the lines and continuum from 54 to 67 keV. Note that the spectrum from detector 4 contains additional background lines that from detector 3 because the fast discriminator threshold for detector 4 had to be set to an energy too high to detect the 14 keV transition. The difference spectrum ('4'-'3') clearly shows the lines at 54 and 67.

Figure 2-9 Three σ sensitivity for narrow lines for the June 27, 1980 Crab Observation.

Figure 2-10 Instrument sensitivity and resolution. At balloon altitude the low energy response is limited by the 3 g/cm^2 of overlying atmosphere as shown. At the bottom, the sensitivity for lines narrower than the instrument resolution is shown for a 10^4 sec total on source/10^4 sec total on background observation. The dash line is corrected for atmospheric transmission to give the sensitivity to photons incident at the top of the atmosphere. Cosmic and solar spectra (at 3 g/cm^2) are shown for comparison.

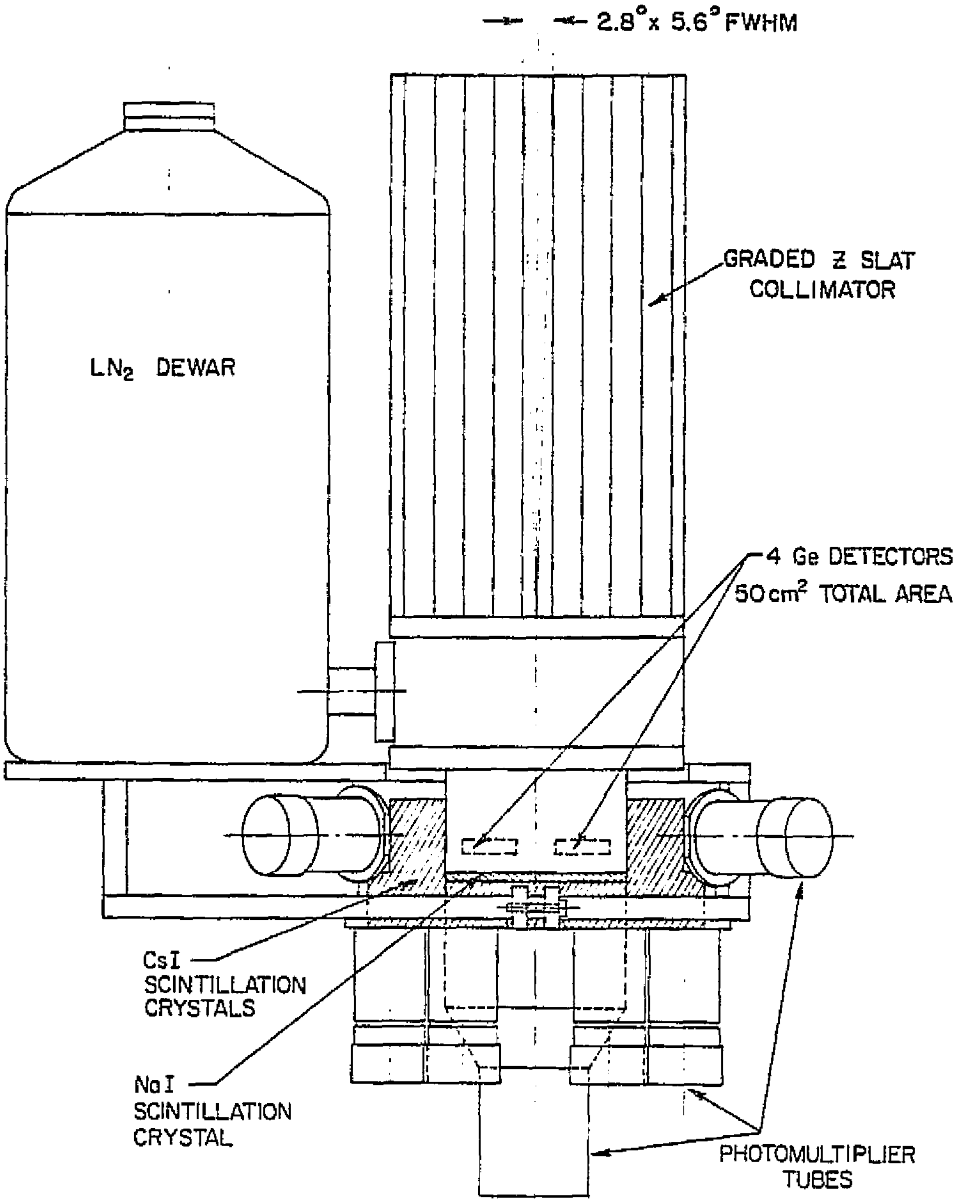
2.8° x 5.6° FWHM
GRADED Z SLAT COLLIMATOR
LN$_2$ DEWAR
4 Ge DETECTORS
50 cm^2 TOTAL AREA
CsI SCINTILLATION CRYSTALS
NaI SCINTILLATION CRYSTAL
PHOTOMULTIPLIER TUBES

HIGH RESOLUTION X-RAY BALLOON INSTRUMENT

Figure 2-1

ORIGINAL PAGE IS
OF POOR QUALITY

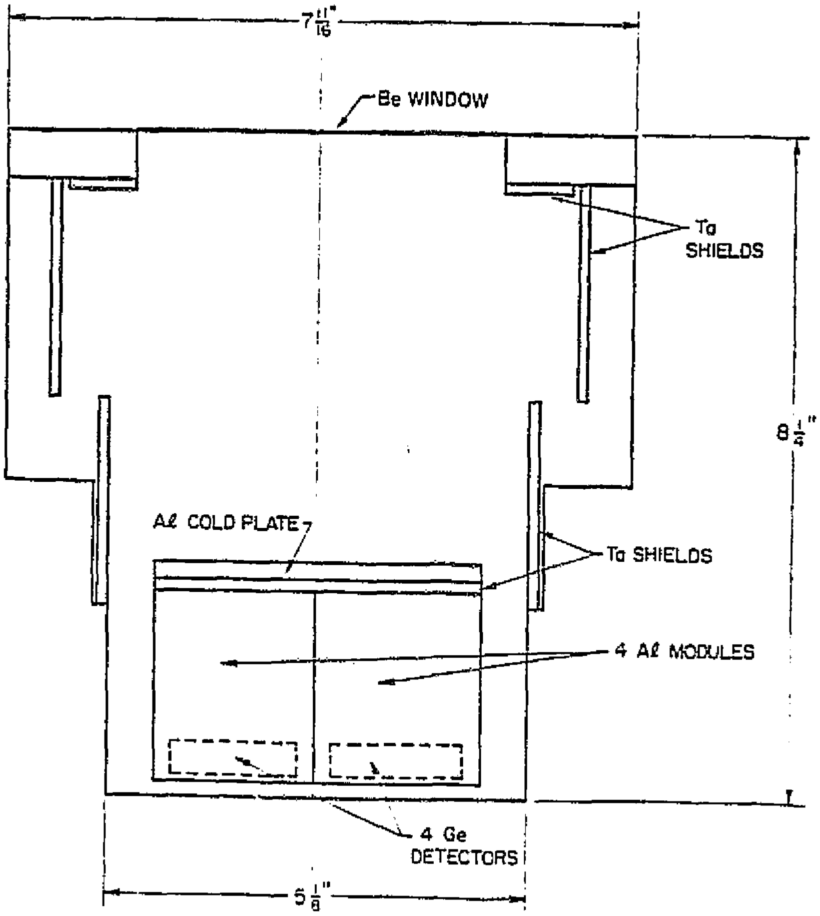
$7\frac{11}{16}''$
Be WINDOW
Ta SHIELDS
$8\frac{1}{4}''$
Aℓ COLD PLATE
Ta SHIELDS
4 Aℓ MODULES
4 Ge DETECTORS
$5\frac{1}{8}''$

Figure 2-2

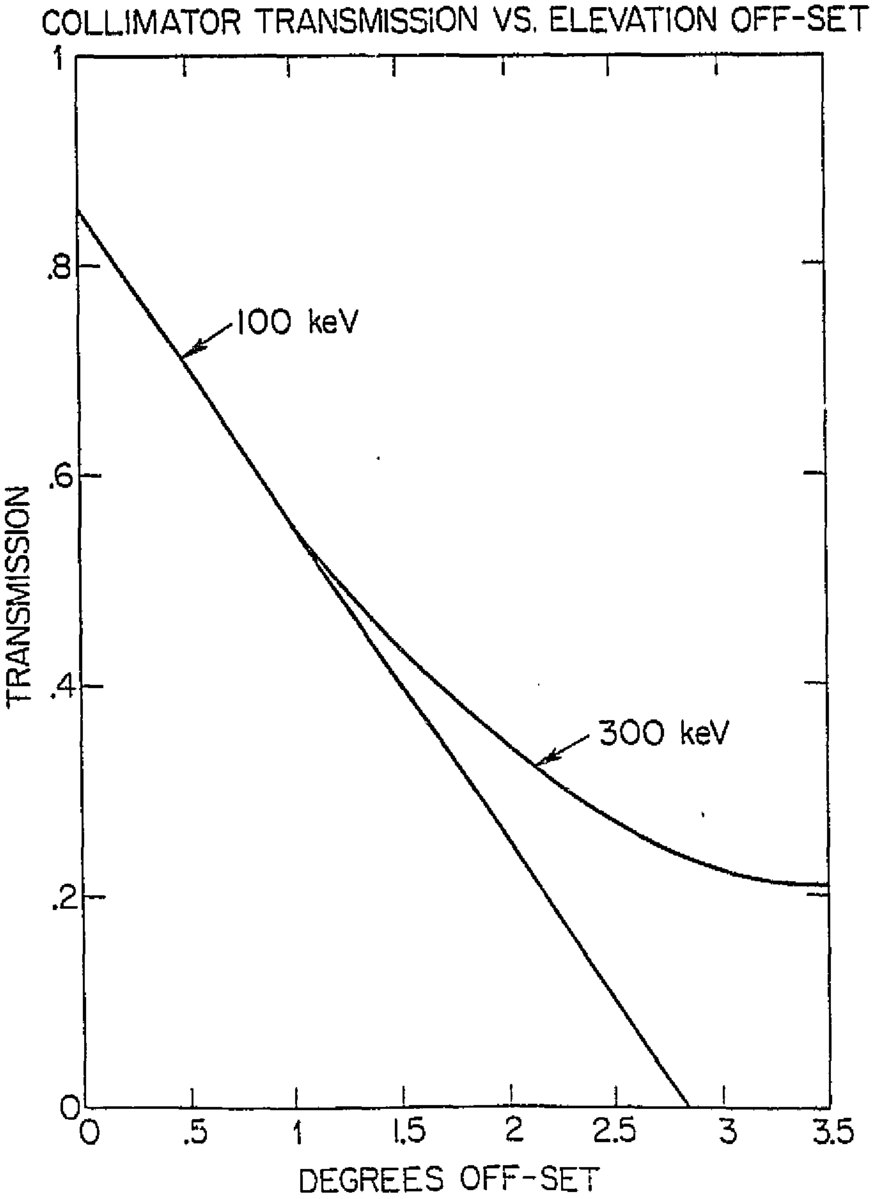
COLLIMATOR TRANSMISSION VS. ELEVATION OFF-SET
TRANSMISSION
1
.8
.6
.4
.2
0
DEGREES OFF-SET
0
.5
1
1.5
2
2.5
3
3.5
100 keV
300 keV

Figure 2-3

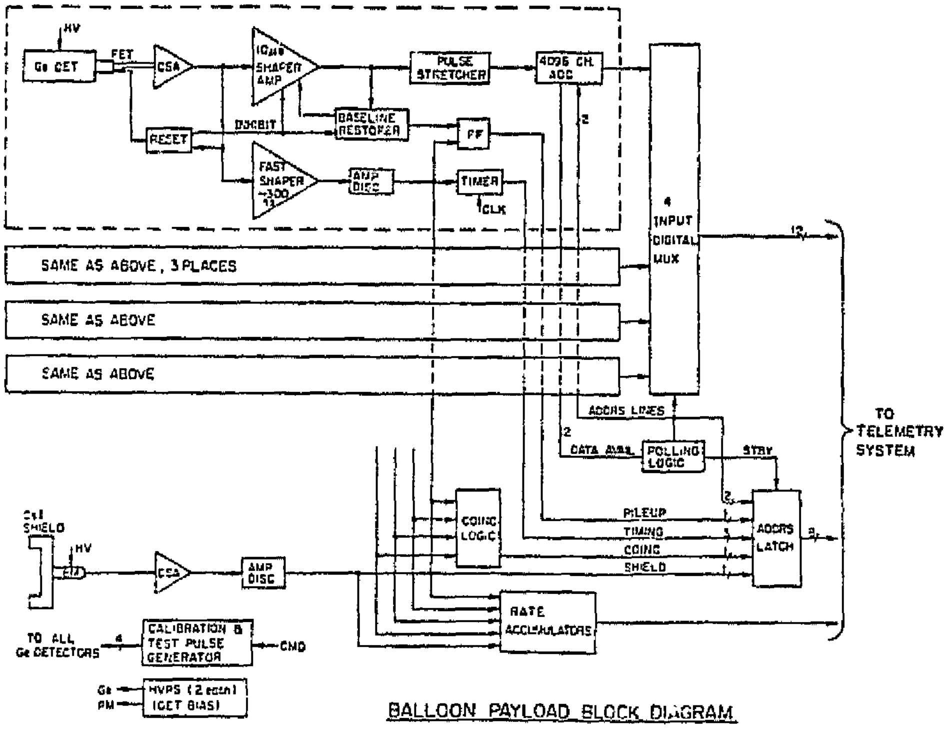
HV
Ge DET
FET
CSA
10µs SHAPER AMP
PULSE STRETCHER
4096 CH. ADC
RESET
DISCBIT
BASELINE RESTORER
FF
2
FAST SHAPER ~300 ns
AMP DISC
TIMER
CLK
4 INPUT DIGITAL MUX
12
SAME AS ABOVE, 3 PLACES
SAME AS ABOVE
SAME AS ABOVE
ADDRS LINES
2
DATA AVAIL
POLLING LOGIC
STBY
TO TELEMETRY SYSTEM
CsI SHIELD
HV
PM
CSA
AMP DISC
COINC LOGIC
PILEUP
TIMING
COINC
SHIELD
ADDRS LATCH
8
RATE ACCUMULATORS
TO ALL Ge DETECTORS
4
CALIBRATION & TEST PULSE GENERATOR
CMD
Ge
PM
HVPS (2 each) (DET BIAS)

BALLOON PAYLOAD BLOCK DIAGRAM

Figure 2-4

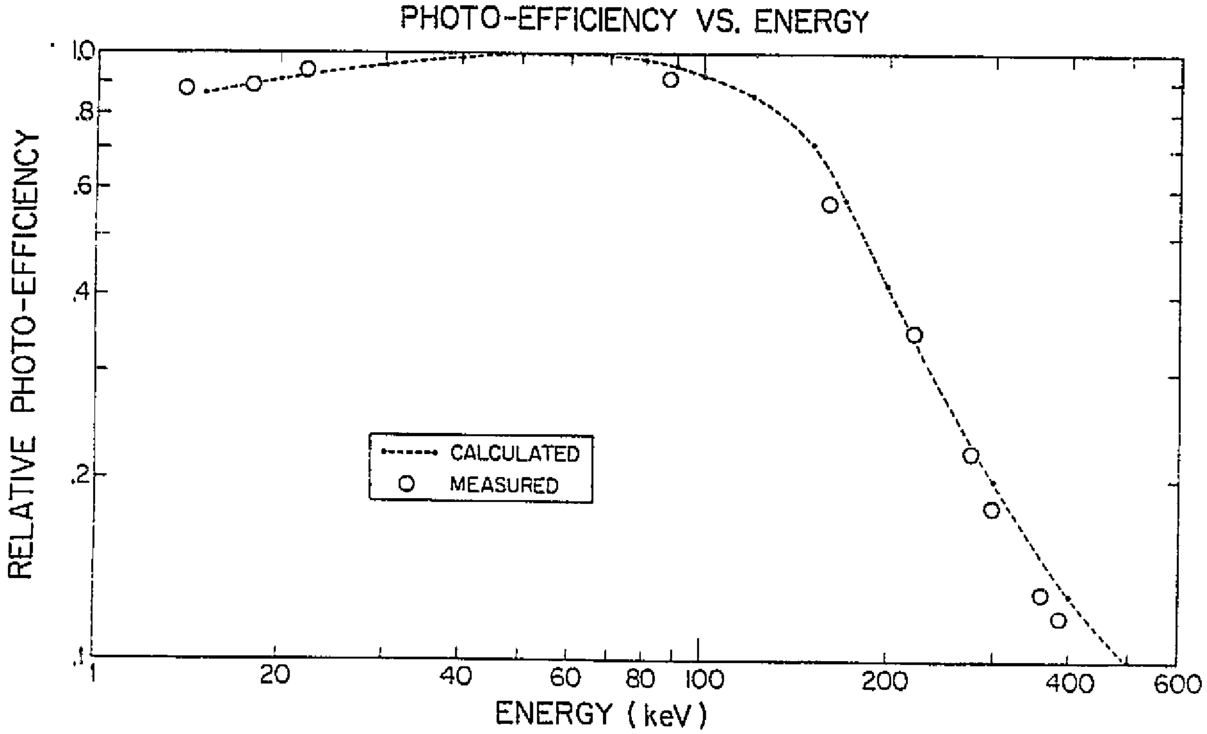
PHOTO-EFFICIENCY VS. ENERGY
RELATIVE PHOTO-EFFICIENCY
1.0
.8
.6
.4
.2
.1
1
20
40
60
80
100
200
400
600
ENERGY (keV)
CALCULATED
MEASURED

Figure 2-5

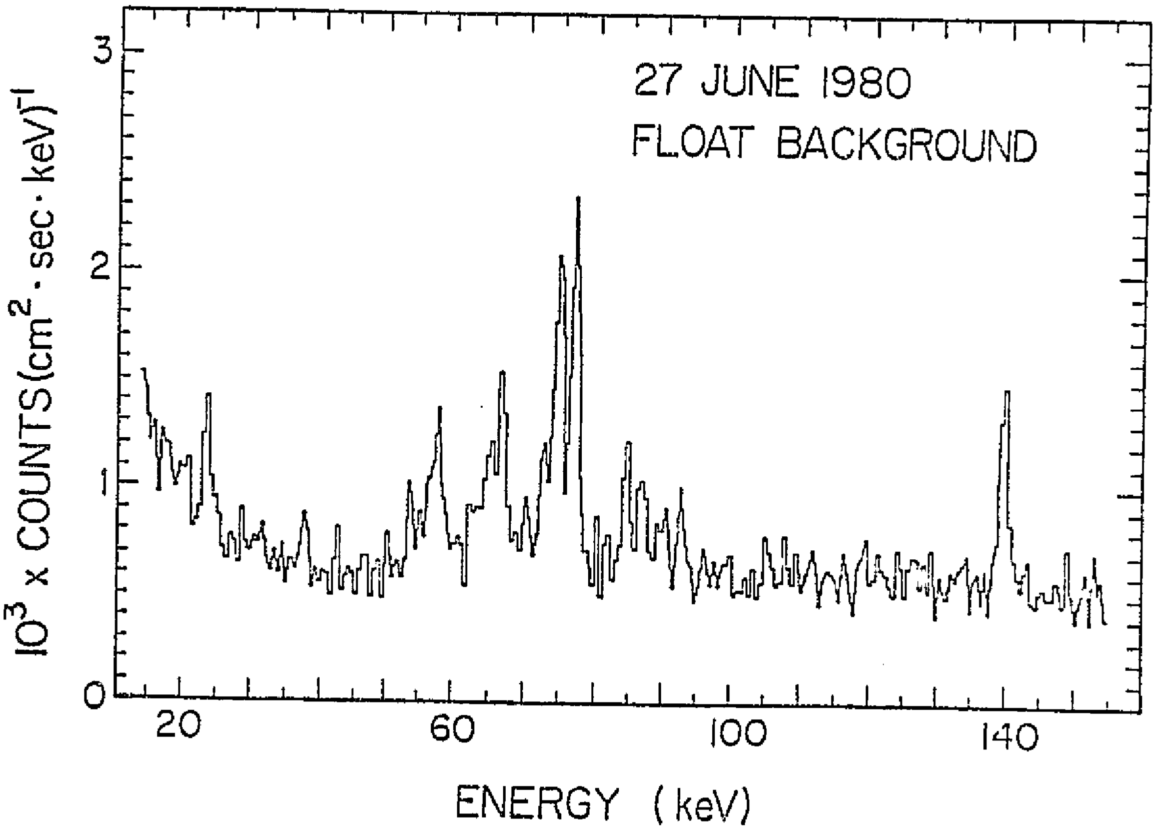
27 JUNE 1980
FLOAT BACKGROUND
10^3 x COUNTS(cm^2 · sec · keV)$^{-1}$
0
1
2
3
20
60
100
140
ENERGY (keV)

Figure 2-6

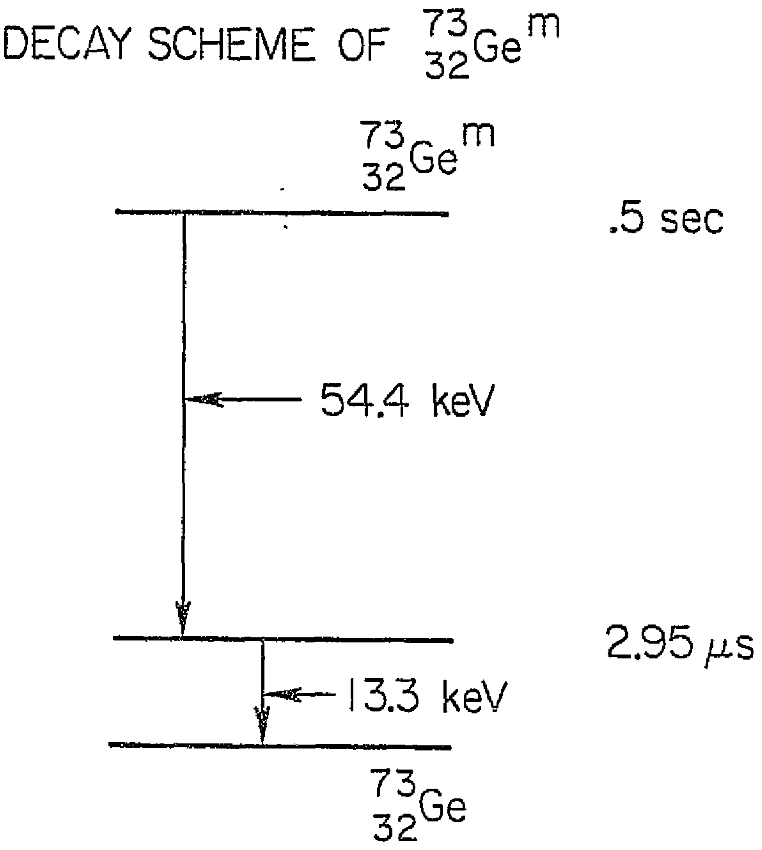
DECAY SCHEME OF $^{73}_{32}\mathrm{Ge}^{m}$
$^{73}_{32}\mathrm{Ge}^{m}$
.5 sec
54.4 keV
2.95 μs
13.3 keV
$^{73}_{32}\mathrm{Ge}$

Figure 2-7

ORIGINAL PAGE IS
OF POOR QUALITY

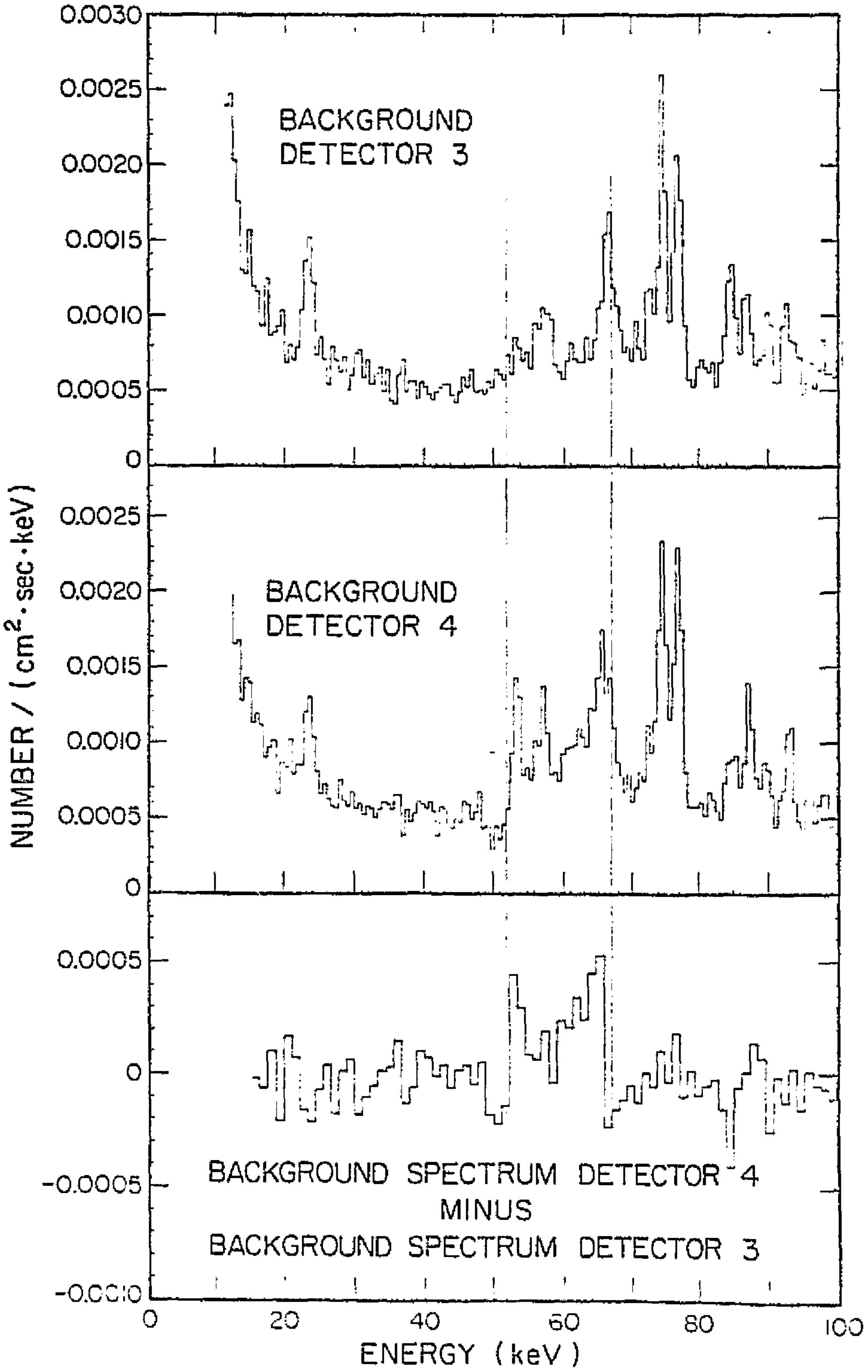

Figure 2-8

ORIGINAL PAGE IS
OF POOR QUALITY

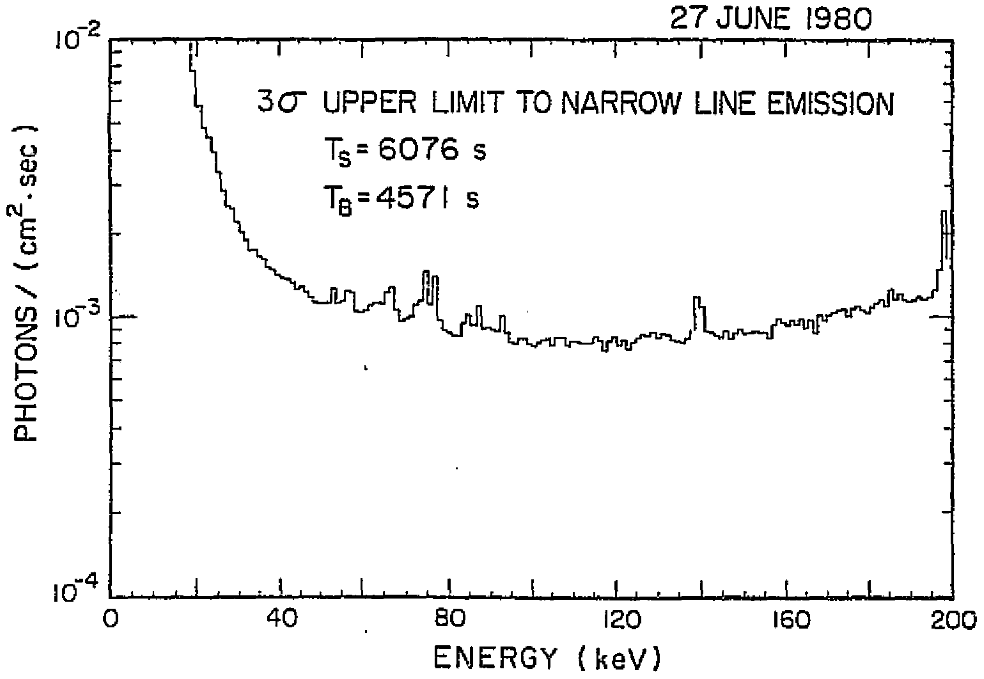

Figure 2-9

ORIGINAL PAGE IS
OF POOR QUALITY

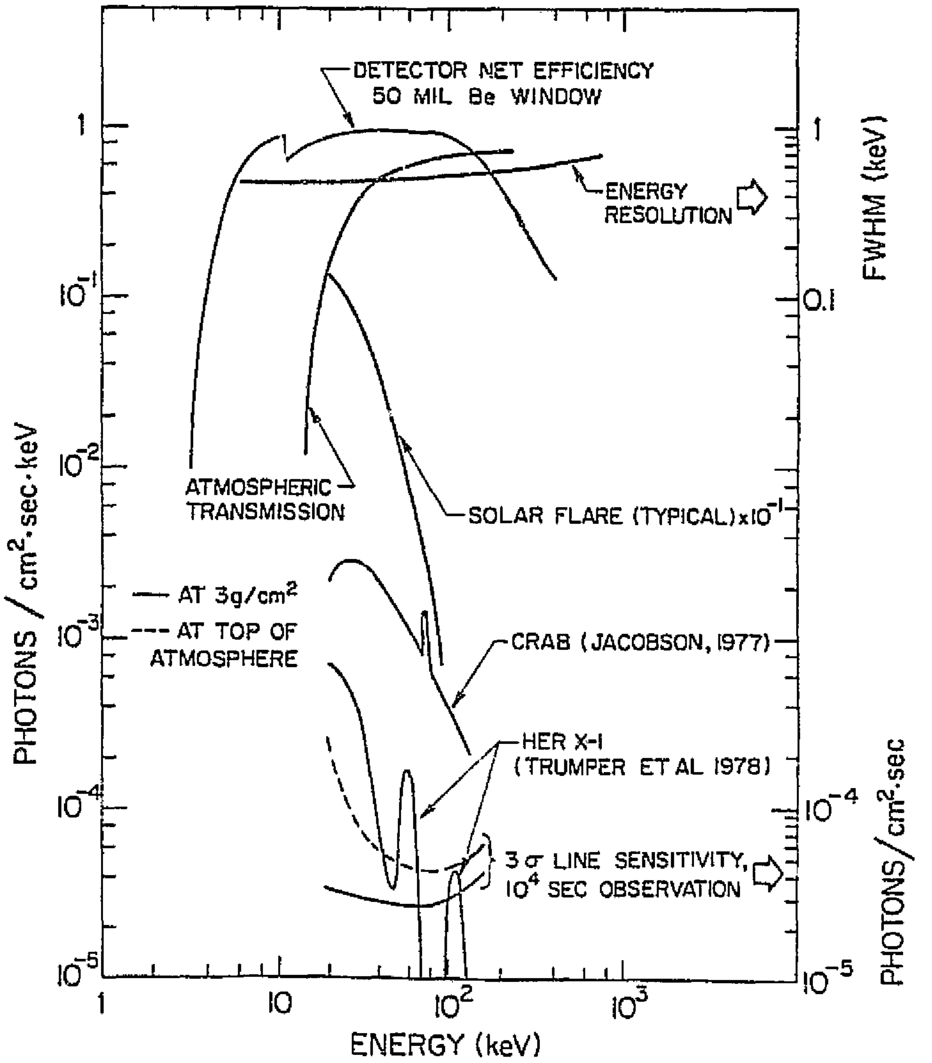

Figure 2-10

THREE

Flare Electron Acceleration

3-A. Introduction

One of the most remarkable aspects of the flare process is that large numbers of electrons appear to be accelerated to 10-100 keV within seconds. These fast electrons may lose almost all of their energy to collisions with cold ambient electrons and less than .01% of their initial energy will be lost to X-ray producing electron-ion collisions. Over a series of bursts lasting $\sim$100 seconds the electrons may carry from $\sim 10^{29}$ to 10^{32} ergs. Under this hypothesis *Lin and Hudson* [1976] and *Duijveman* [1982] both found that the acceleration process may convert at least 10-50% of the flare energy into fast electrons as opposed to heat or mass motion. The flare electrons cannot be measured *in situ*, but the instantaneous electron and X-ray spectra are related by the Bethe-Heitler bremsstrahlung cross-section. Because hard X-rays propagate freely through the tenuous overlying solar atmosphere, they are an excellent probe of the physical conditions in the electron source and/or the electron interaction region.

On June 27, 1980 we observed an intense solar flare in hard X-rays using a germanium spectrometer and large area phoswich scintillator. With our unprecedented spectral and temporal resolution we can address a number of important questions about the flare process. Is the fast electron population in the X-ray production region thermal or non-thermal? How many different electron acceleration mechanisms are there? When and how are the electrons accelerated? Where do the fast electrons deposit their energy?

Figure 3-1 shows the entire flare from 1612 until 1633 UT over the five scintillator rate channels, 22-33 keV, 33-60 keV, 60-120 keV, 120-235 keV, and >235 keV. Here we see a series of intense bursts of a few to a few tens of seconds in duration over the impulsive phase from 1613:30-1617:30 UT. The ISEE-3 spacecraft data [Kane private comm.] show that the 5-6 keV soft X-rays begin to rise at 1612 UT. After 1617:30 UT a gradual hard X-ray decay begins, but there are at least four impulsive bursts between 1618 and 1631 UT.

We found that the falling low energy, $\lesssim 30$ kev, flux after 1617:30 UT is dominated by emission from a super-hot component [*Lin et al.* 1981]. The spectrum in Figure 3-2, 1617:00-1617:10 UT, shows a steep increase at low energy which distinguishes the super-hot component from the impulsive component (For the four parameter model fit, $\chi^2_{104} = .78$). This new component is the radiation from an ~ 30 million degree nearly isothermal electron plasma with an emission measure over 10^{48} cm^{-3}. It is first seen shortly after the overall flare peak is reached at 1616:08 UT. We emphasize that only by using a high resolution instrument can the super-hot component be accurately measured and identified. The super-hot component is discussed in the next chapter.

Below 120 keV, the spikes show the typical flare hard X-ray soft-hard-soft spectral evolution described by *Kane et al.* [1980]. Also, the spikes peak simultaneously (within .128 sec.) for all energies below 120 keV. This is consistent with the electrons rapidly losing their energy in a high density region where the electron lifetime is short, less than 1/4 sec. If true, the temporal evolution of the photon flux mirrors the electron acceleration profile. Two interpretations are offered of the underlying acceleration process:

1. Below 120 keV a single acceleration mechanism is repeated in a succession of 'elementary' bursts [*de Jager and de Jonge* 1978].
2. As an alternative we hypothesize that the hard X-rays are produced from the superposition of the flux from two non-thermal electron components. The *gradual* component, important below

50 keV, varies over 10-20 seconds while the *rapid* component, important from ~30-100 keV, varies over ~1-4 seconds.

The X-ray flux profile above 120 keV is delayed by 1-2 seconds with respect to the lower energy X-ray flux. Such delays could be produced if the collisional electron lifetime for the >120 keV electrons is ~2-4 seconds longer than for the ~60 keV electrons since the X-ray producing electron population is approximately given by the injection rate integrated over an electron lifetime [*Bai and Ramaty* 1979, *Vilmer et al.* 1982]. However, our high sensitivity observations can rule out the low energy (<120 keV) delays expected for this mechanism, so we conclude that it is the injection/acceleration of the high energy electrons which is delayed. The observed spectral variations are consistent with the delayed high energy electrons having been accelerated by a first-order Fermi mechanism operating on electrons injected by the initial acceleration mechanism.

3-B. Acceleration of 15-120 keV Electrons

Hard X-ray Spectra

The accurate determination of the hard X-ray spectrum is important for the understanding of the role played by the fast electrons in the flare energy release process. In a non-thermal interpretation the observed hard X-rays are from the bremsstrahlung of fast electrons streaming through a cold plasma ($kT_e << E_e$). These fast electrons suffer electron-electron Coulomb collision losses 10^4-10^5 times as great as the radiative losses. For the observed X-ray fluxes this low radiative efficiency implies that a large fraction of the flare energy would be initially contained in the fast electrons [*Lin and Hudson* 1976, *Duijveman* 1982]. Alternatively, in a thermal model the hard X-rays are produced by thermal bremsstrahlung from a very hot, 10^8-10^9°K, plasma. If the hot thermal electrons can be confined and isolated from the cooler surrounding medium, the collisions between the fast electrons will only exchange energy within the very hot plasma [*Smith and Lilliequist* 1979]. Then, the radiative losses would dominate implying that far fewer fast electrons produce the same time integrated X-ray flux. However, isolating these ultra-high temperature electrons from their surroundings is difficult, so that some of their energy must be lost through conduction and convection. *Kiplinger et al.* [1983] show for observed burst rise times of ~100 msec that a thermal model will be more efficient only for plasma densities in excess of 1.6×10^{11} cm^{-3}.

The fast electrons of a high density plasma quickly approach a Maxwellian distribution in a time $\tau_{coll}=3.8\times 10^{10}/n$ for an average electron energy of 20 keV and electron density n [*Spitzer* 1962]. Such a plasma at a single temperature produces a characteristic hard X-ray spectrum [*Mätzler et al.* 1978]. Previous broad resolution observations indicated that the impulsive hard X-ray spectrum is a falling power-law at low energy (with a spectral index between -2.5 and -7) which steepens further somewhere above ~50-100 keV. It is important to note that these measurements could not exclude a single temperature source for the hard X-rays [*Elcan* 1978, *Mätzler et al.* 1978]. Using the high resolution spectral data, we can determine from the shape of the impulsive spectra whether a single temperature plasma can be the source.

We first consider the photon spectrum over the six 20-30 second intervals in Figure 3-1b. These are long enough to have good count rate statistics. Here we are interested in the accelerated electrons so we exclude the flux from the super-hot component which first appears after 1616 UT. Since the super-hot component is very steep at low energies we can select the impulsive energy range by inspection (see Figure 3-2). The energy ranges are given in Table 3-1

Three models for the hard X-ray emission are compared with the data. One model is an ultra-hot single temperature thermal plasma where kT_e ranges from ~10-30 keV and includes a back-scattered contribution [*Mätzler et al.* 1978]. Basically, the photon spectrum is nearly proportional to $(1/E)\times e^{(-E/T)}$ in this model. The other two models are non-thermal: the single power-law,

Table 3-1 Comparison of Spectral Models to Flare Spectra

Comparison of χ^2_ν for Model Spectra						
Time	1614:40 15:00 UT	1615:00 15:23 UT	1615:23 16:00 UT	1616:00 16:20 UT	1616:20 16:50 UT	1616:50 17:20 UT
Spectrum	I	II	III	IV	V	VI
Range (keV)	15-290	15-290	15-290	20-290	25-290	29-290
Data Pts.	24	21	26	23	22	18
Test for Goodness of Fit						
Model	χ^2_ν					
Thermal	19.2	39.7	39.2	9.9	8.3	7.4
Power-Law	6.2	10.5	9.2	2.3	1.5	1.4
Double Power-Law	1.07	1.25	1.65	0.6	0.33	1.30
F Test	44	64	44	30	33	1.4
Double Power-Law Parameters						
A (10^6)	.20	.77	2.0	.30	.93	.28
E_b keV	38±5	25±2	42±5	45±15	59±23	NA
$\gamma 1$	3.3	3.6	3.7	2.9	3.3	3.1
$\gamma 2$	3.8	4.9	4.6	3.5	3.9	NA
Thick-Target Power						
Power 10^{28} (ergs/s)	1.0	1.8	4.8	4.8	5.2	1.9

Spectrum labels (I-VI) correspond to the labels on the spectra in Figure 3-3. Time intervals indicated in Figure 3-1b.

$$A \times E^{-\gamma},$$

and the double power-law,

$$A \times E^{-\gamma 1} \text{ for } E < E_b \text{ and}$$
$$(A \times E_b^{-\gamma 1})\ E^{-\gamma 2} \text{ for } E \geqslant E_b.$$

These three model functions were fit to the spectra for the six time intervals, and Table 3-1 summarizes the comparison of the reduced Chi-square statistic, χ^2_ν [*Bevington* 1969], for the best fits of the free parameters for these model functions. The χ^2_ν statistic measures the squared deviation of the model function from the data points normalized by the expected statistical errors and the degrees of freedom for the fit. For the thermal model there are two free parameters, the temperature and the normalization constant. For the single power-law the free parameters are A and γ and for the double power-law the free parameters are A, E_b, $\gamma 1$, and $\gamma 2$. ν, the degrees of freedom, is given by the difference between the number of data points less the number of free parameters. The number of data points for each spectrum is given in

Figure 3-3.

Examining Table 3-1 we see that the double power-law model is an acceptable fit to all the spectra since the χ^2_ν statistic is always around 1. The best ultra-high single temperature model always gives an unacceptably large χ^2_ν of 7 or more. Moreover, in Figure 3-3I-VI we see that the best non-thermal model really matches the data points. (Small values of the χ^2_ν statistic can be produced from a poor model by using a data set with very large error bars.) The inset in Figure 3-3II shows that even for the steepest spectrum observed the thermal model falls off too quickly at energies greater than 40 keV. The two additional parameters of the double power-law are significant if the reduction in χ^2_ν satisfies the F test [*Bevington* 1969]. The computed values of F in Table 3-1, for the first five intervals, are all well over 10 which justifies the additional parameters, while interval VI is adequately fit by the single power-law. The change in slope between $\gamma 1$ and $\gamma 2$ ranges from .5 to 1.3, and even spectrum VI, (Figure 3-3VI) shows some steepening at high energy. The break energy, E_b, is usually between 30 and 40 keV, although the break energy cannot be constant throughout the whole impulsive phase. (The intervals quoted for E_b are 90% confidence intervals [*Lampton et al.* 1976] for a four parameter fit.)

So far the analysis has been over the major features of the impulsive phase, but the rate channel ratios, Figure 3-4, exhibit the characteristic soft-hard-soft spectral variation through each individual burst [*Kane et al.* 1980]. Could the double power-law be produced by the superposition of true single power-law or isothermal spectra? Since the spectra turn down at high energy we can exclude a sum of single power-laws. However, a sum of thermal spectra can mimic a non-thermal spectrum over a finite energy range. When the spectra are fit over two second intervals the double power-law is still the superior fit with the parameters for the three models covering about the same range as in Table 3-1. Therefore, the impulsive hard X-ray source is not an evolving single temperature plasma, but the superposition of several isothermal sources cannot be excluded.

To find the minimum amount of energy in the fast electrons, we assume that the the non-thermal electrons are injected into a region (known as a thick target) where the electrons are completely stopped. Clearly, if the fast electrons had escaped through a thin target region, they would have initially contained more energy to produce the same X-ray flux. We can adequately approximate the injection electron spectra with a double power-law [*Kane et al.* 1983]. The electron spectral indices are given by $\gamma 1+1$ and $\gamma 2+1$ at low and high energy respectively while the break point energy is 20 keV above the photon break. The normalization is obtained by using the single power-law conversion coefficient ($\approx 10^{33}$ electrons ph^{-1} cm^{-2} at 60 keV for $\gamma 2=4$) from *Hudson et al.* [1978] for the high energy electron spectrum at the electron break. Then the low energy electron spectrum is matched at the break. Using this approximation, the average power injected into the fast electrons is calculated for each interval and listed in Table 3-1. The total energy injected must be at least 5×10^{30} ergs over these six intervals.

Note that the injected power remains nearly unchanged from spectrum III through V in Table 3-1 from 1615:23-1616:50 UT. This is despite the fact that the X-ray spectrum is more intense and harder from 1616:00-1616:20 UT (see Figure 3-4) than at any other time during the flare. This is because the harder X-ray spectrum is the bremsstrahlung from an electron spectrum of fewer, although more energetic, electrons. (The more energetic electrons have a higher radiation yield, on average, before stopping.) So although the X-ray spectrum is rapidly varying over spectrum III through V in Figure 3-3, the input rate of energy into the electrons hardly changes over 90 seconds. It is also interesting to repeat this analysis over the rise of a single peak. We have divided the rise of the most intense burst in the flare into three, four second time intervals from 1615:58 to 1616:10 UT. We fit these spectra to double power-law models and obtain the data in Table 3-2. Here we see that the injected power, for a 15 keV electron cutoff, seems to drop at the flare peak. Figure 3-5 shows the thick target electron power through the whole impulsive phase compared to the 33-60 keV X-ray count rate. Of course, the actual injected power depends critically on the true low energy cutoff. We only

Table 3-2 Thick-Target Power for Burst Rise at Flare Peak

Thick-Target Power Near Flare Peak			
UT	1615:58 - 16:02	1616:02 - 16:06	1616:06 - 16:10
Φ_{15} ph cm^{-2} sec^{-1} kev^{-1}	130	125	120
Φ_{50} ph cm^{-2} sec^{-1} kev^{-1}	2.5	3.0	4.4
$\gamma 1$	3.27	3.11	2.74
P_{15} (10^{28} erg/s)	4.3	3.5	2.7

Φ_{15} is the X-ray flux at 15 keV. P_{15} is the thick-target power for a 15 keV electron cutoff.

know that the impulsive hard X-ray spectrum extends to 15 keV for this flare. Table 3-2 illustrates that one must take care when interpreting the variation in the hard X-rays as a variation in the power injected into the fast electrons.

Burst Evolution

The X-ray flux profiles of Figure 3-1b are directly proportional to the instantaneous population of fast electrons in the X-ray production/energy loss region. The temporal evolution of this fast electron population is principally determined by the variation of the injection rate and the fast electron lifetime. The fast electrons may be lost either by energy loss or by escape from the interaction region. If the electron lifetime is short compared to the e-folding time for the injection rate, then the injection rate profile will be closely reflected in the X-ray count profile.

The fast electron energy loss rate will be at least as high as the electron-electron Coulomb collision loss rate given by [*Trubnikov* 1965]

$$\frac{dE}{dt} = -4.9 \times 10^{-9}\, n\, E^{-.5} \text{ keV } s^{-1} \tag{3-1}$$

for an electron energy E (keV) in a region with a cold electron density n. So the electron lifetime, τ_e, will be no longer than

$$\tau_e < (1/E)(dE/dt) = 2 \times 10^{8}/n \; sec. \tag{3-2}$$

Any burst profile governed by collisional energy loss (3-2) would harden as the flux decreases.

This variation is in sharp contrast to the softening depicted by the count rate channel ratios of Figure 3-3. We believe then, that the burst evolution is dominated by the variation of the electron injection spectrum because the fast electron lifetime is short compared to the time scale for the burst evolution.

The fastest burst decay time during this flare is ~1 second in the 120-235 keV count rate. We know that the profile is injection dominated, but such short electron lifetimes are possible possible either through Coulomb collisions in a high density region where the target density exceeds 2.6×10^{11} cm^{-3} (by (3-2)) or by escape through a thin target. Since a 60 keV electron travels ~120,000 km in one second, outward travelling fast electrons moving along open field lines could easily escape the denser corona within a few tenths of a second. However, this model implies an even greater number of initially accelerated electrons. In addition, spacecraft measurements in the interplanetary medium usually show that typically the number of escaping electrons are less than 1% of the total number of electrons accelerated under the non-thermal interpretation of the spectrum [*Lin* 1974]. The thick target interpretation suggests that the higher energy electrons reach the chromosphere where $n > 10^{12}$ cm^3. Electrons with an energy E (keV) will be stopped by a column density $(nL) > 2\times 10^{17}\times E^2$ (cm^2) where n is the ambient electron density averaged over the path length L (cm). So for a reasonable coronal density of 2×10^{10} cm^3 and L<40,000 km, almost all of the >20keV electrons would reach the chromosphere if, as the rapid high energy decay suggests, there is no significant electron trapping within the corona.

'Elementary' Bursts vs. Two Component Picture

De Jager and de Jonge [1978] have advanced the idea that flare time profiles are composed of a series of 'elementary' impulsive bursts. These bursts appeared to narrow with increasing energy as $t \propto E^{-.68\pm.05}$ for the bursts they observed. The complex bursts observed here agrees well with this picture at energies below 120 keV. The spikes run together at low energy and are more clearly separated at higher energies (Figure 3-6a). The narrowing with increasing energy (see spike at 1615:28 UT in Figure 3-6a) is exactly equivalent to the soft-hard-soft spectral evolution. This, then, is a fundamental property of the acceleration mechanism within the thick target picture. As an example, the 60-120 keV rate in Figure 3-6b is decomposed into a set of possible 'elementary' bursts. Under the 'elementary' burst interpretation, the start of a rise to a peak is obscured by decay of the previous peak, i. e., the bursts overlap. This is particularly true at lower energy where the bursts must be broader for this interpretation to be consistent with the observations.

Suppose, instead, that the low energy X-ray profile is smoother because the injection of lower energy electrons is slowly varying and a separate mechanism for the spiky bursts which inject the higher energy electrons. We hypothesize that there is a *gradual* component varying over 10-20 seconds and a *rapid* component varying over 1-4 seconds. The *gradual* component dominates the flux below 30 keV and falls off very steeply above that energy while the *rapid* component dominates at higher energy and produces the numerous bursts. Possibly these two components are produced by different acceleration mechanisms with their own spectral and temporal characteristics. In Figure 3-6c the 60-120 keV rate is decomposed into possible *rapid* and *gradual* components. The *rapid* high energy component must be non-thermal, but what about the *gradual* component? From 1615:15-18 UT there are no apparent bursts, so this interval might have the closest to a purely *gradual* component This spectrum is still a double power-law with a spectral index of 3.7 below 26 keV and 5.2 above, and not a single temperature thermal. Thus, we conclude that the *gradual* component is non-thermal. Could the *gradual* component electrons, which are at lower energy, be a trapped remnant of the *rapid* component electrons? This scenario seems unlikely because the 60-120 keV *gradual* component electrons/X-rays appear to decay more rapidly than the 22-33 keV *gradual* component electrons during the dip in the flux around 1615:10 UT in Figure 3-7. As before, faster decay at high energy indicates that the X-rays are produced by the continuous injection of fast electrons rapidly losing their energy.

Figure 3-7a and Figure 3-7b show a hypothetical temporal evolution of the *gradual* component in the 22-33 keV and 60-120 keV channels through the impulsive phase. The *gradual* component might comprise about 60-70% of the 22-33 keV flux (exclusive of the super-hot component) and about 10-20% of the flux from 60-120 keV. Since the *gradual* component would probably be relatively stronger below 15 keV, greater than 70% of the non-thermal energy would be in the *gradual* component electrons.

Both the 'elementary' burst and two component pictures are consistent with the data, but have different implications for the physics of the flare process. The 'elementary' burst picture has several important elements which may be characteristic of the acceleration process: the soft-hard-soft spectral evolution and the fact that the start of the bursts follow within a time of the order of the burst duration. It may be that one burst acts as a trigger for the succeeding burst. The most important implication of a two component picture is that there are two mechanisms for accelerating the 10-100 keV electrons. However, the spectral evolution is no longer strictly due to a single acceleration process, but is attributed, in part, to the changing ratio of the injection of two processes which produce very different spectra. In a non-thermal thick target picture the total fast electron energy depends only upon the total photon spectrum, which is not changed. Although the total energy does not change, this picture implies that the *gradual* component is more energetically important than the more dramatic *rapid* component.

Pre-Flare Acceleration

Elliot [1965] proposed that flares could be the result of a sudden precipitation of energetic ions stored high in the corona where their lifetime is long. Electrons, too, might be stored in a low density region where their collision loss rate would be low and then precipitated during the flare. This scenario allows the acceleration of electrons over a much longer time scale at a much lower rate. The stored electrons, however, would radiate via bremsstrahlung. Using the high sensitivity of these detectors we have set upper limits to the preflare flux from 1600-1610 UT. The three sigma upper limit to the flux at 20 keV is $8.3\times10^{-4}\ \mathrm{ph\,cm^{-2}\,sec^{-1}}\,kev^{-1}$. This gives an upper limit to the power-law emission measure [*Hudson, Canfield, and Kane* 1978] $N_{20}\,n_i < 2.4\times10^{39}\mathrm{cm}^{-3}$, where N_{20} is the average number of electrons above 20 keV at any instant of time in a region with an ion density n_i. Conceivably, the electrons could be stored very high in the corona where the density could be as low as $1\times10^{5}\mathrm{cm}^{-3}$. This would give a 50 hour collisional lifetime for a 20 keV electron. Then up to 2×10^{35} electrons could have remained undetected. This is about the number of fast electrons in the small early burst at 1614:00 UT and it is less than about 1% of the total accelerated electron population (see Figure 3-1). So while it is possible that a stored population could have triggered one of the early small bursts, the vast majority of the flare electrons could not have been stored in the corona but must be accelerated during the impulsive phase.

Post-Impulsive Phase Acceleration

In Figure 3-1 we see that at ~1617:30 UT the >60 keV X-ray flux falls to <1% of its intensity at the flare peak. Also, the 22-33 keV rate, mostly from the super-hot component, is falling more slowly. Of greater interest for this discussion of electron acceleration is the series of impulsive bursts most clearly seen in the 33-60 keV rate in Figure 3-1. We shall call this time from 1617:30 to past 1630 UT the Post-Impulsive phase. Because other flare hard X-ray observations have been made with detectors of poorer sensitivity [*Kane et al.* 1980], the discussion of impulsive phenomena has been limited to the more intense fluxes which are typically found in the usual impulsive phase which for this flare lasts only 3-4 minutes. However, the post-impulsive phase exhibits impulsive bursts, which are a strong signature of electron acceleration, for an additional 13 minutes. Several questions can be explored during this period. Are electrons accelerated during the post-impulsive phase or is the non-thermal emission due to a stored remnant of fast electrons accelerated in the impulsive phase? Are fast

ORIGINAL PAGE IS
OF POOR QUALITY

electrons accelerated at this time? Is the process the same as during the intense impulsive bursts?

First, our very high sensitivity measurements show that there are impulsive bursts throughout the post-impulsive phase. In order to enhance the bursts' contrast, the 22-33 and 33-60 keV rates have been filtered by subtracting a portion of the 80 second running average for each rate. Figure 3-8 shows these impulsive components together with the 60-120 keV rate. At least 10 spikes are evident with four complex bursts at 1618:45-1619:15, 1620:10-1621:00, 1623:40-1624:10, and 1629:30-1630:15 UT.

Post-Impulsive Phase Bursts			
----- BURST 1 1620:16-54 UT -----			
Time	1620:16-24	1620:41-45	1620:12-54 UT
Type	Spike	Spike	Total Burst
Relative Rates			
22-30 keV	85±20	90±20	40±10
33-60 keV	19±2	43±5	20±3
60-120 keV	6.2±2	11±4	6±1
γ	>5	~4.5	~4.5
-- BURST 2 1623:29-24:14 UT --			
Time	1623:40-44	1623:57-61	1623:29-24:14 UT
Type	Spike	Spike	Total Burst
Relative Rates			
22-33 keV	51±9	54±9	36±3
33-60 keV	27±5	31±5	22±1.5
60-120 keV	7±2	13±3	6±1
γ	~4.3	~4.0	~4.2
-- BURST 3 1629:30-30:14 UT --			
Time	1628:31-29:29	1629:45-53	1629:30-30:14 UT
Type	Pre-Burst	Spike	Total Burst
Relative Rates			
22-33 keV	6.5±.5	24±3	14±1.5
33-60 keV	2.4±.7	19±2	10.7±.7
60-120 keV	1.5±.7	4.5±2	3.6±.7
γ	>4.5	~3.4	~3.5

Post-Impulsive Phase Bursts lists the properties of the three later bursts. These bursts are similar to the impulsive phase bursts. All three bursts have a comparable peak intensity of about .5% of the largest impulsive phase peak. All three bursts have fast spikes which rise and fall in 4-10 seconds. The spectral index γ, uncertain due to the large low energy continuum rates, is obtained by comparison with the count rates during the impulsive phase. These values are consistent with a non-thermal spectrum as are the bursts in the impulsive phase. For the last burst, the spike is clearly harder than the pre-burst emission from 1628:30-1629:31 UT. Certainly, this continual bursting is evidence of electron acceleration throughout the post-impulsive phase.

To search for a stored remnant from the impulsive phase we must look for a spectrum which hardens as the flux decays. The power-law index (from the spectrometer data), of Figure 3-9 does not harden systematically from 1618 through 1624 UT. To gain additional high energy sensitivity we also compare the scintillator 60-120 keV rate with the germanium spectrometer non-thermal 33-60 keV flux in Figure 3-9a. The only hardening occurs during the times of the discrete bursts. Figure 3-8 does not show any obvious spikes from 1625 through 1629:30 UT, so we can examine the spectrum at this time to look for a low-level continuously emitting stored remnant. Integrating over this time reveals a net spectrum with a power-law index γ somewhere between 4 and 5. Again, this seems too soft to be a decayed trapped population from the impulsive phase. Thus, the post-impulsive phase non-thermal emission is unlikely to be from a stored remnant from the impulsive phase, but rather is more probably from electrons accelerated during the post-impulsive phase.

We can interpret this post-impulsive phase emission within the 'elementary' burst or the two component picture. The 'elementary' burst picture is suggested by the fast spikes which are similar to the spikes of the impulsive phase because they come in groups and are of comparable duration. The statistics are too poor to discern the soft-hard-soft spectral evolution. The low-level emission from 1625-1629:30 UT could be produced by numerous small unresolvable 'elementary' bursts. Of course this same soft continuous emission is very suggestive of the soft *gradual* component of the two component hypothesis. Finally, assuming that the decay phase emission above 35 keV extends to as low as 15 keV, as during the impulsive phase, implies that the non-thermal electrons of the decay phase contain ~3% as much energy as the impulsive phase electrons.

3-C. Acceleration of Electrons to >120 keV

We have already seen that, below 120 keV, the flux at all energies rises to virtually simultaneous peaks. However above 120 keV, in Figure 3-10a and Figure 3-10b, the most intense and the hardest bursts are always delayed from .3 to 2 seconds after the low energy bursts. We show that because the low energy peaks are nearly simultaneous, the delays at high energy are inconsistent with a simple collisional loss process. A second-step acceleration process [*Bai and Ramaty,* 1976 and 1979] is considered. In this process some of the fast electrons are further accelerated within a few seconds. Their subsequent appearance in the interaction region produces the delayed X-ray profile. The second-step acceleration interpretation is more consistent with the observation, and we show that first-order Fermi acceleration mechanism is consistent with the observed spectral variations.

Time Delays

Figure 3-10a is a smoothed plot of the 60-120 keV and 120-235 keV rates during the impulsive phase. The smoothed rate during each .128 sec interval is computed by averaging the rate over the surrounding bins using a Gaussian weighting function with a .5 sec FWHM for the 60-120 keV rate and with a 1. sec FWHM for the two rates above 120 keV. This filters out the high frequency fluctuations, both real and statistical, but does not move the bursts' centroids. The 120-235 keV peaks are delayed for the bursts marked A,B,C, and E. In Figure 3-10b we see that the >235 keV rate is delayed with respect to the 60-120 keV rate for the bursts D and F as we have already reported [*Bai et al.* 1983]

In order to quantify the delays at high energy and to place limits on low energy delays we compute the cross-correlation function between the rate pairs (22-33 keV,60-120 keV), (60-120 keV,120-235 keV), and (60-120 keV, >235 keV) for these six bursts. The smoothed rates were used only for the rates above 120 keV. The cross-correlation function between two rates R_i and R_j is

$$CCF(t)_{ij}=\frac{\sum_{n=1}^{N-u}(R_i\,(n)-\overline{R}_i)\;(R_j\,(n+u)-\overline{R}_j)}{[\sum_{n=1}^{N-u}(R_i\,(n)-\overline{R}_i)^2\;\sum_{m=n+u}^{N}(R_j\,(m)-\overline{R}_j)^2]^{1/2}} \qquad (3\text{-}3)$$

where $t=u\times.128$sec. The results are plotted in Figure 3-11. From these functions the delay time is obtained and listed in Table 3-3. For the burst at 1616:38 UT, the >235 keV rate is too low to accurately determine a centroid. The delay listed between the 22-33 keV and 60-120 keV rates is an upper limit based on the count rate statistics. Only burst C, at 1615:52 UT, has a real delay at low energy of .128 seconds. Above 120 keV, all of these bursts show real delays. There is a delay of ~1-2 seconds for the 120-235 keV rate for the medium sized and shorter duration bursts A, B, C, and E. For the two most intense and longest duration bursts, D and F, the longest delay is for the >235 keV rate with only a smaller delay for the 120-235 keV rate. We note that these two intense and spectrally hard burst show this upward shift of the delay energy.

Delay Mechanisms

A high energy X-ray delay is produced because the high energy electron population peaks after the low energy population within the X-ray production region. The delays may be produced by one, or both, of two processes: injection or decay. If the injection rate peak of high energy electrons is delayed with respect to the low energy injection, then a delay will result

Table 3-3 Cross-Correlation Delays

Cross-Correlation Delays						
Burst	A	B	C	D	E	F
Time after 1600 UT	14:48	15:37	15:52	16:08	16:38	17:02
(22-33,60-120 keV)	<.05	<.05	<.20	<.05	<.05	<.05
(60-120,120-235 keV)	.8±.5	1.1±.5	1.9±.5	0.4±.25	0.9±.5	.2±.25
(60-120,>235 keV)	-	-	-	1.5±.5	-	1.8±.5
Delay Expected For Collisional Loss Process						
(22-33,60-120 keV)	.13	.13	.60	.12	.26	.15

between the peak of the X-ray profiles. Alternatively, lower decay rates at high energy produce a delay from simultaneous injection profiles because the electron population is nearly given by integrating over a decay time.

Using a simple model we can illustrate the delayed decay process and quantify the delay as a function of the lifetime. The instantaneous particle population, $N(t)$ changes with time as

$$\frac{dN(t)}{dt} = -\left\{\frac{1}{\tau_e}\right\} N(t) + q(t) \tag{3-4}$$

where τ_e is the particle lifetime and $q(t)$ is the injection rate. $N(t)$ may be roughly approximated by integrating $q(t)$ over a single lifetime, τ_e.

$$N(t) \sim 1/2\, \tau_e \left\{ q(t-\tau_e) + q(t) \right\} \tag{3-5}$$

To find the time of the peak population set $\frac{dN(t)}{dt}$ in (3-4) to zero and use $N(t)$ given by (3-5) to obtain

$$q(t) \sim q(t-\tau_e) \tag{3-6}$$

For a symmetric injection profile about t_0, the population peak occurs at a time

$$t = t_0 + \tau_e/2 \text{ since } q(t_0 - \tau_e/2) = q(t_0 + \tau_e/2) \tag{3-7}$$

Thus, the population peak occurs about half a particle lifetime after the injection peak. This model holds over discrete energy intervals even though the electrons which are lost from one interval by collisional loss move to a lower energy interval. This downward electron flux (in energy space) is not included in the model, but it is small compared to the injection rate because the electron injection spectra are steep.

Thus, for two simultaneously peaking electron injection profiles at energies E_1 and E_2, the delay decay between the respective X-ray profiles is about $1/2 \left\{ \tau_e(E_1) - \tau_e(E_2) \right\}$. Moreover, this relationship is roughly independent of the variation with energy of the injection time scale. Using the collisional lifetime, (3-2) for a constant ambient electron density, we extrapolate the observed delays at high energy to obtain a consistent delay between the 22-33 keV and 60-120 keV rates. We use the lower energy bound of the rate channel to compute these lifetimes. Table 3-3 lists this extrapolated delay and it is significantly greater than the upper limit determined using the cross-correlation function. Additionally, for decay to be the dominant process, the X-ray rate profile at high energy must decay more slowly than an electron lifetime. For the burst C at 1615:52 UT (Figure 3-10a), the 120-235 keV X-ray flux decay time is ~2 seconds. The observed delay implies a lifetime of at least 4 seconds which is longer than the burst profile allows. Since this condition is violated, and because there are no low energy delays observed as would be expected for collision decay delay, we conclude that it is the injection of the >120 keV electrons which is consistently delayed throughout this flare.

One type of injection delay would occur if there were a difference in the electrons' time of flight from the acceleration region to the X-ray production region. Since higher energy electrons are faster, the observed delay has the wrong sign for a common thick target X-ray region. Even if the effective thick target is different for low and high energy electrons, the >100 keV electrons ($v > 1.6 \times 10^{10}\,\mathrm{cm\,sec^{-1}}$) will be stopped within a few tenths of a second. Thus, for a simultaneous acceleration, differential time of flight cannot produce 1-2 second high energy X-ray delays.

Instead, the delays may be produced if a second mechanism accelerates some of the fast electrons over 1-2 seconds and then these electrons are injected into the X-ray production region. The rate profiles may be produced by an admixture of both the initial and second accelerations. This blend of simultaneous and delayed injection might account for the apparent shift in delay energy for the two most intense bursts D and F. These bursts are also the hardest, so the electrons from the initial acceleration may dominate the signal of the additional acceleration mechanism at a higher energy than for the softer bursts.

The need for a second acceleration mechanism to boost the fast electrons to energies from .1 to greater than 1 MeV has been recognized for many years. Observations showed that for some larger flares the production of these higher energy electrons occurred in close association with other phenomena: Type II and IV radio bursts and the injection into the interplanetary medium of energetic ions of several to several tens of MeV [*Ramaty et al.* 1980]. All of the high energy particles were thought to be accelerated over several minutes during a second phase which immediately followed the impulsive phase. The process energized protons far more easily than electrons because the observed electron to proton ratio above 1 MeV was probably less than 1% [*Ramaty et al.* 1980]. It was believed that the particle acceleration was by repeated scattering off the coronal shock waves which produce the Type II radio emission [*Wild, Smerd, and Weiss* 1963, *de Jager* 1969]. Since this scattering gives equal velocity boosts to both electrons and protons, this picture is consistent with the higher mass protons being accelerated to higher energy. Also, shock waves in the solar wind are known to produce super-thermal protons [*Gosling et al.* 1981].

The best timing signature of the acceleration of the high energy ions is found in the impulsive gamma-rays produced when the ions collide with other particles in the solar atmosphere. The very large and well-studied flare of August 4, 1972 produced the first solar gamma-ray line measurements. These seemed to support the picture of a second phase of acceleration minutes after the impulsive phase [*Bai and Ramaty* 1976]. Recent measurements of gamma-ray flares by the Solar Maximum Mission [*Forrest et al.* 1981, *Chupp* 1982] have shown that in many flares the protons must be accelerated within a few seconds of the 10-100 keV electrons. For most of the gamma-ray line flares, there is also a delay of several seconds seen in the >130 keV X-rays relative to the lower energy X-rays. *Bai and Dennis* [1983] showed that both the gamma-ray producing ions and the .1 to 1 MeV electrons might be accelerated by a second-step mechanism.

The second-step acceleration process requires the injection of energetic particles from a first-step process. It must accelerate the particles to their peak energy within seconds since the time profile of the higher energy particles is as spiky as the <100 keV hard X-ray profiles of the impulsive phase. This is very different from the second phase picture where the acceleration takes place over minutes. Also, the time profiles of particles accelerated during a second phase vary much more slowly than the impulsive hard X-ray profiles [*Bai* 1982].

First-Order Fermi Acceleration

Consider two shock fronts moving up both ends of a flux tube. An energetic particle caught between the two fronts will be seen to approach one of the shock fronts. In the shock rest frame, the particle will be magnetically reflected by the shock's higher field with no change in energy but with a change in the particle direction of motion. Transforming back to the flux tube frame there is an energy gain for this single collision given by

$$dE = 2v_p \, \mu \, v_S \frac{W}{c^2} \qquad (3\text{-}8)$$

where v_p is the particle velocity, μ is the cosine of the pitch angle, v_S is the speed of the shock front along the field lines, and W is the total particle energy Γmc^2. Repeated collisions with the approaching fronts continue to accelerate the particles. This is first-order Fermi acceleration where the particles gain energy with each collision.

We follow *Bai et al.* [1983] to find the net energy gain from successive collisions. The time averaged distance, d, between the shocks is the half-length of the flux tube. So the average time interval between successive collisions is

$$dt = d\,(v_p < \mu >)^{-1} \qquad (3\text{-}9)$$

Combining ((3-8)) and ((3-9)) gives the energy gain rate for $v_S << v_p \sim c$:

$$\frac{dE}{dt} = 2\,E < \mu^2 > \; ((\Gamma + 1)/\Gamma) \; (d/v_S)^{-1} \qquad (3\text{-}10)$$

The electron kinetic energy $E = (\Gamma - 1) \times 511\,\text{keV}$. For a 100 keV electron, with $< \mu^2 > = .5$ and $(d/v_S) = 2$ sec., dE/dt is 92 keV/sec., which is quite substantial. Here we have identified the shock transit time (d/v_S) with the delay time. Typically, one might expect $v_S \sim 1000$ km sec^{-1} so that 2 sec. corresponds to a loop length of 4000 km for the shock propagation. Since there will be collisional losses, too, there will be some injection energy above which electrons gain more energy than they lose. This is determined from the gain rate (3-10) and the loss rate (3-1).

$$(1-\beta^2)^{-1/2}\,\beta^3 = 3\times 10^{-13}\, n <\mu^2>^{-1} (d/v_S) \qquad (3\text{-}11)$$

For $n = 3\times 10^{10}\,\mathrm{cm}^{-3}$ the injection speed is $\beta \sim .32$ so $E_{inj} = 26\,\mathrm{keV}$. Then, dE/dt at 100 keV will be 77 keV sec^{-1} which is still very large.

The high resolution spectra may show evidence of this second-step. In Figure 3-12 there are five spectra which were accumulated over the intervals marked in Figure 3-10. The evolution is similar over both bursts. At low energy the slope is fairly constant over the burst, but at high energy the spectrum hardens. We see that the double power-law becomes single power-law although we do not have the counting rate sensitivity to observe the hardening in detail. For example, an important question is: Does the spectrum harden by increasing E_b or by raising the whole high energy spectrum? Delayed injection of high energy electrons would produce the trend we have found that the decay side is harder at high energy energy than the rising side of the burst. Note, though, that the high energy spectral exponent does not become less than the low energy spectral exponent. This holds true throughout the impulsive phase and may be an important clue to the underlying acceleration mechanism.

We can estimate the evolution of the electron spectrum due to first-order Fermi acceleration using a simple model. Assume that the electrons are perfectly trapped within a volume where the density is low enough that the collision losses ((3-1)) and other losses are small compared to the energy gain given by (3-10). Furthermore, approximate $(\Gamma+1)/(\Gamma)$ by 2 ($E \leq 200\,\mathrm{keV}$) and ignore the change in $<\mu^2>$ despite the increasing parallel component of velocity. The trajectory, $E(t)$, of a single electron initially at E' is determined by integrating the energy gain (3-10).

$$E(t) = E' e^{\alpha t} \tag{3-12}$$

where $\alpha \sim 4 <\mu^2> (v_S/d)$. The spectral evolution is determined by a continuity equation for the electrons with no source term:

$$\frac{\partial N}{\partial t}(E,t) + \frac{\partial}{\partial E}[N(E,t)\frac{dE}{dt}] = 0 \quad (\mathrm{el}\, kev^{-1}\, \mathrm{sec}^{-1}) \tag{3-13}$$

To find the correct $N(E,t)$ consider the electrons between E' and $E'+dE'$ at $t=0$. These electrons will all move to an interval between E and $E+dE$ at a time t, where E is given by (3-12). Therefore,

$$N(E',t=0)dE' = N(E,t)dE \tag{3-14}$$

and $dE = N(E')\, e^{-\alpha t}$. Substituting for E' and dE' in (3-14) yields

$$N(E,t) = N(E',t)\, e^{-\alpha t} \tag{3-15}$$

For a single power-law at $t=0$, $N(E')=A\ E^{-\gamma}$, the spectrum at a later time t will be

$$\begin{aligned} N(E,t) &= A\ (E\, e^{-\alpha t})^{-\gamma}\, e^{-\alpha t} \\ &= A\ E^{-\gamma} e^{(\gamma-1)\alpha t}. \end{aligned} \tag{3-16}$$

We can also determine the evolution of an initial double power-law spectrum,

$$\begin{aligned} N(E,0) = {} & A\ E^{-\gamma 1} && ;E<E_{b_0} \\ & [A\ E_{b_0}^{\gamma 2-\gamma 1}]\ E^{-\gamma 2} && ;E \geqslant E_{b_0}. \end{aligned}$$

The electrons just below the initial break point energy must all follow the trajectory given by (3-12) and their spectrum must evolve exactly as for a single power-law with a spectral index $\gamma 1$. Electrons initially below E_{b_0} clearly cannot exceed $E_{b_0}\, e^{\alpha t}$. Similarly, the electrons initially above E_{b_0} will all be above $E_{b_0}\, e^{\alpha t}$ at t with a spectrum given by the single power-law solution for the high energy index, $\gamma 2$. Therefore, the total electron spectrum as a function of t is given by

$$\begin{aligned} N(E,t) = {} & A\ E^{-\gamma 1}\, e^{(\gamma 1-1)\alpha t} && ;\ E<E_{b_0}\, e^{\alpha t} \\ & [A\ E_{b_0}^{(\gamma 2-\gamma 1)}]\ E^{-\gamma 2}\, e^{(\gamma 2-1)\alpha t} && ;\ E \geqslant E_{b_0} e^{\alpha t} \end{aligned} \tag{3-17}$$

Substitution verifies that this function is a solution for (3-13) and that the electron spectrum is continuous at the changing break point energy.

So this simple model predicts that the high energy electron spectral exponent can never become smaller than the initial lower energy spectral exponent. Also, an initial double power-law spectrum remains a double power-law with an increasing break energy. Furthermore, the intensity of the high energy spectrum increases more rapidly than the intensity of the lower energy spectrum. This model does not include escape, collisions, or radiation. We have noted that the ~40-100 keV spectral exponent (Figure 3-12) does not become lower than the low energy spectral exponent either during or after the peak of any burst. This limit to hardening is just as expected from this simplified model. But we do not have the count rate sensitivity to determine whether E_b increases in the manner predicted by this model. Also, the delays are found at energies above 120 keV where we do not have sufficient counts to watch the spectrum evolve. At low energy the density of first-step fast electrons is too high to be changed by the injection of a few second-step electrons. But at high energy where the initial electron density is very low, the shock accelerated electrons may be the dominant component and the delay time might really be the time it takes to accelerate the electrons to higher energy.

This scenario requires a shock wave for each of the six delayed bursts from 1614:48 through 1617:02 UT. Shock waves could be created by the flare explosion process which is initiated by the rapid transfer of energy to the chromosphere by the fast electrons [*Brown* 1973, *Lin and Hudson* 1976]. The target atmosphere responds by an increase in temperature. As the temperature increases the emissivity of the atmosphere above 100,000 K rapidly decreases. Therefore, the atmosphere cannot radiate away this additional energy flux. At some fast electron flux level, the conductive losses will be small compared to the input power. Then, much of the beam power will go into the explosive expansion of the target plasma. Computer simulations [*Fisher et al.* 1984] indicate that an energy flux greater than $3 \times 10^{10} \mathrm{ergs\,cm^{-2}\,sec^{-1}}$ over 5 seconds will initiate a shock wave within a rigid flux tube model. We can estimate the area covered by the flare hard X-rays from the H_α optical measurements of 1.5–$3. \times 10^{18}\,\mathrm{cm}^2$. Using the larger area as an upper limit to the flux tube foot points, we find a lower limit average energy flux of 1.3×10^{10} ergs cm^{-2} sec^{-1}. The energy flux during a single spike could be much higher if each burst occurs over a distinct flux tube with a much smaller cross-section. So it is possible that the start of each intense fast electron burst could trigger the explosion which initiates the shock waves for the second-step acceleration.

There is an intense Type II radio burst seen at 1620 UT in meter waves which indicates a shock propagating out through the corona. Although we have not examined the radio records to search for multiple shocks, this emission is consistent with an event starting sometime during the impulsive phase and moving with a velocity ~500–1500 km sec^{-1}. Undoubtedly the second-step acceleration process is much more complicated, but the data do, at least partially, support the rapid acceleration of electrons by the first-order Fermi process.

The second-step will also accelerate protons which are detectable by the gamma-ray line emission they produce, or by *in situ* measurements by spacecraft in the interplanetary medium. The June 27, 1980 flare did produce 8×10^{30} protons (>10 MeV) in interplanetary space [*Bai et al.* 1983] which left the sun within a half hour of the start of the flare.

Energetic protons collisionally excite ions in the solar atmosphere, some of which decay by positron emission [*Ramaty et al.* 1982, *Ramaty et al.* 1983]. The positrons slow down, and subsequently annihilate to produce line emission at 511 keV. Our germanium spectrometer is capable of detecting this line with high spectral resolution (~1.5 keV *FWHM*). The spectrum at 511 keV, Figure 3-13 indicates a flux at the Earth of 3 ± 2.7 ph cm^{-2} over the entire flare. This compares to a total flux of 35 ph cm^{-2} for the giant August 4, 1972 flare. This implies a 3σ upper limit of 10^{33} to the number of protons, E>30 MeV, hitting the sun. Therefore, the escape fraction lies between .001 and 1 which is consistent with other observations [*Ramaty et al.* 1980, *Lin and Hudson 1976*]. If we extend the thick target model electron injection spectrum to high energy, we find that the proton to electron ratio is greater than 10^{2}. As expected for a process where the average non-relativistic particle receives the same velocity boost, ions are accelerated to higher energies than electrons.

A second-step acceleration process thus, in principle, seems most compatible with the delays observed during this flare. First-order Fermi acceleration is an attractive mechanism because it can rapidly boost both electrons and protons to higher energies. We have shown that the first-order Fermi process is consistent with both the physical conditions in the fast electron environment and the hard X-ray data from this flare.

Figure Captions

Figure 3-1 (a)Large area scintillator counting rates during June 27, 1980 flare from 16:12:00 through 16:33:00 UT and (b) from 1614:24 through 1617:24 UT. High resolution spectra are accumulated over the intervals marked in (b) with Roman numerals. Count rates are corrected for detector live time and the aperture response of the collimator.

Figure 3-2 High resolution flare X-ray spectrum from 1617:00-1617:10 UT. The steep increase at low energy is the emission from a thermal plasma while above ~20 keV we see a spectrum which is nearly power-law in shape. For the four parameter model fit, $\chi^2_{104} = .78$.

Figure 3-3 High resolution spectra with best model fit for six time intervals during the impulsive phase. The inset in (II) shows the best ultra-high temperature thermal fit.

Figure 3-4 Scintillator rate channel ratios and 60-120 keV scintillator rate. Maxima occur at the counting rate peaks showing the soft-hard-soft evolution of the bursts.

Figure 3-5 Thick target electron power above 15 keV. Also shown is the 33-60 keV X-ray count rate for the scintillator. For this low energy cutoff, the X-ray peaks and power peaks are sometimes anti-correlated.

Figure 3-6 Hard X-ray bursts (a) decomposed into possible 'elementary' burst profiles (b) and into the *gradual* and *rapid* components (c).

Figure 3-7 Hypothetical temporal evolution of the *gradual* component at 22-33 keV and at 60-120 keV. The fast fluctuations would be due to the *rapid component*. Also included is the 15-20 keV photon flux. Early in the impulsive phase the 15-20 keV flux is almost completely due to the non-thermal *gradual* component. After ~1616:10 UT, the lowest energies are dominated by the emission from the thermal super-hot component.

Figure 3-8 Post-Impulsive phase scintillator counting rates. (a) 60-120 keV rate corrected for collimator transmission. (b) 22-33 keV and 60-120 keV rates with slowly varying component removed to enhance fast spikes.

Figure 3-9 (a) 33-60 keV photon flux in excesss of the super-hot component vs. 60-120 keV scintillator counting rate. (b) single power-law spectral index γ.

Figure 3-10 Delayed bursts for photon energies >120 keV. (a)Delay of 120-235 keV profile with respect to 60-120 keV rate. (b)Delay of >235 keV rate with respect to 60-120 keV rate.

Figure 3-11 Cross-correlation functions for the six bursts which show delay between X-rays below 120 keV and above 120 keV.

Figure 3-12 Five spectra taken from bursts at 1616:08 UT and 1617:02 UT. Spectra show evolution of high energy component through bursts.

Figure 3-13 High resolution X-ray spectrum around 511 keV from germanium spectrometer. The $\sim 1\sigma$ excess is not statistically significant.

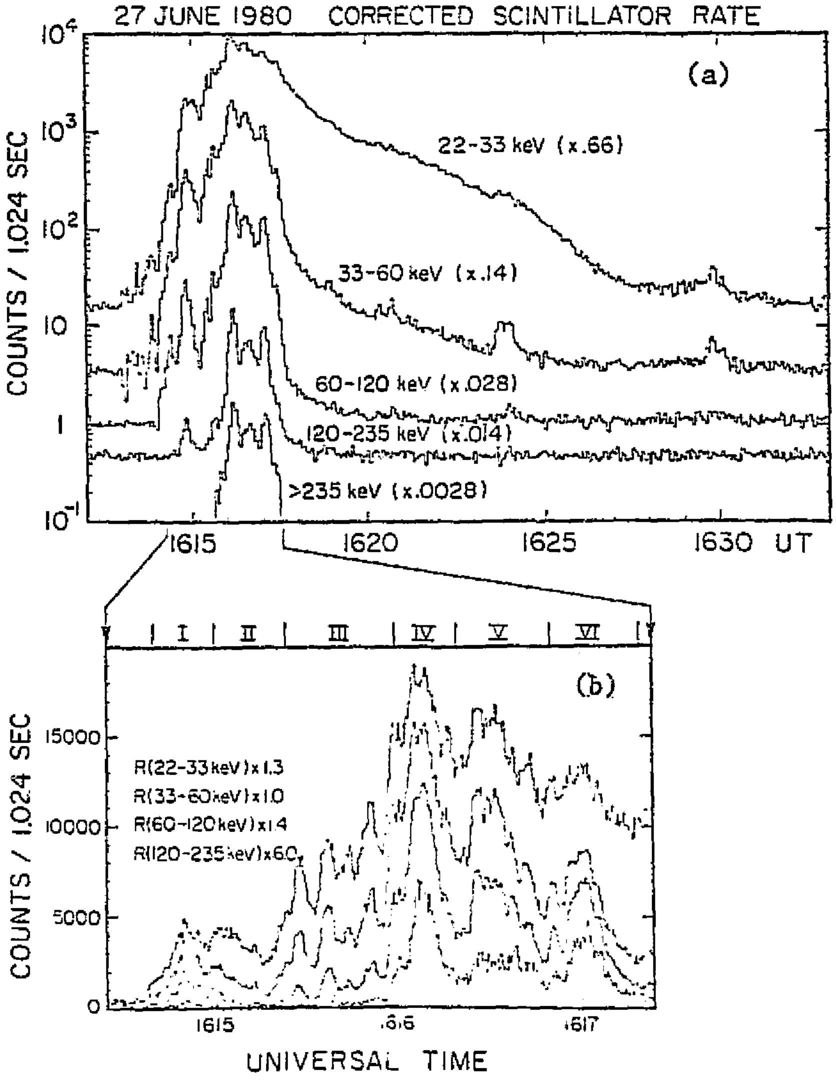
27 JUNE 1980 CORRECTED SCINTILLATOR RATE
(a)
COUNTS / 1.024 SEC
10^4
10^3
10^2
10
1
10^{-1}
22-33 keV (x.66)
33-60 keV (x.14)
60-120 keV (x.028)
120-235 keV (x.014)
>235 keV (x.0028)
1615
1620
1625
1630 UT
I
II
III
IV
V
VI
(b)
COUNTS / 1.024 SEC
15000
10000
5000
0
R(22-33keV)x1.3
R(33-60keV)x1.0
R(60-120keV)x1.4
R(120-235keV)x6.0
1615
1616
1617
UNIVERSAL TIME

Figure 3-1

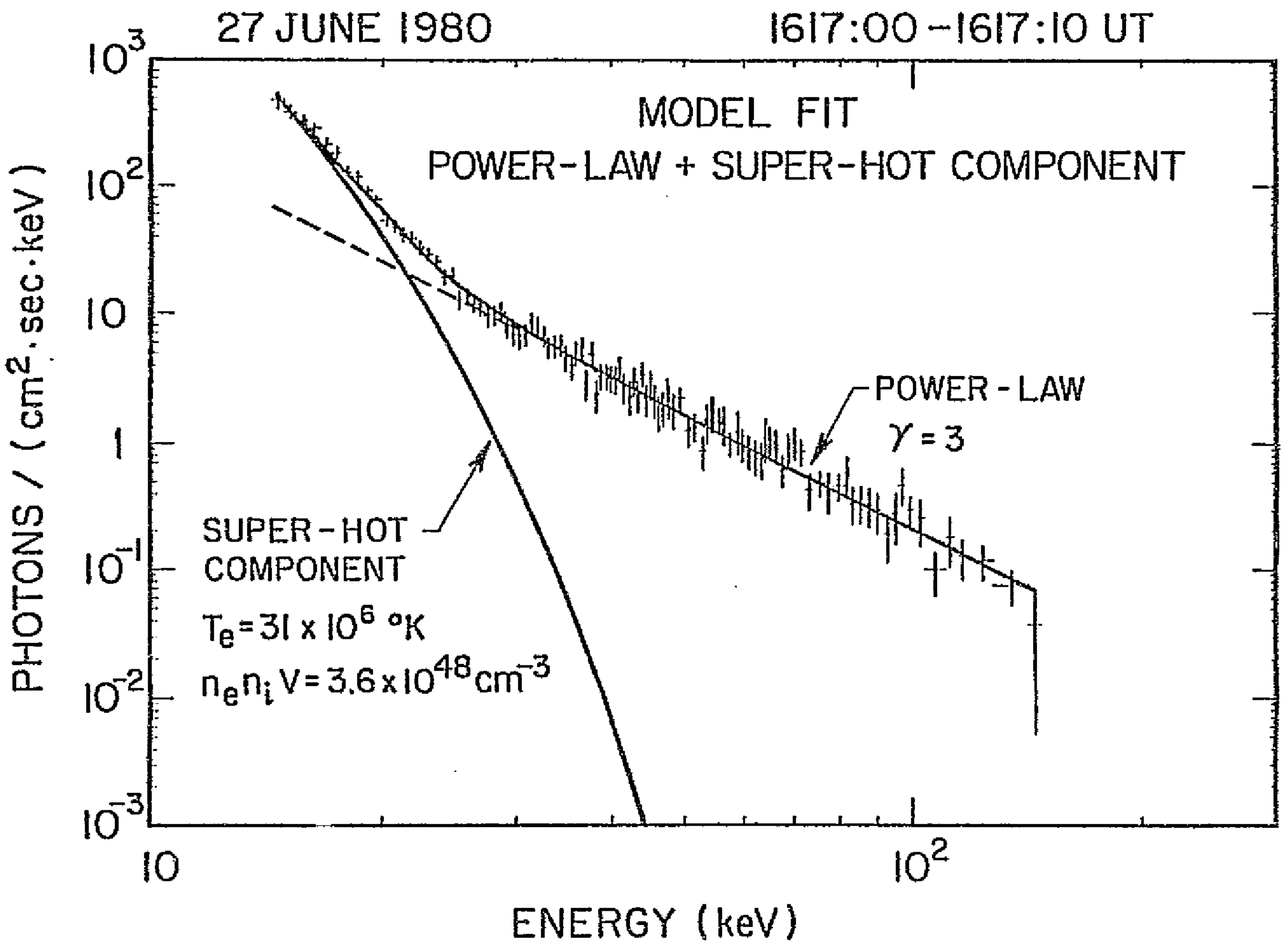
27 JUNE 1980
1617:00 – 1617:10 UT
MODEL FIT
POWER-LAW + SUPER-HOT COMPONENT
POWER-LAW
$\gamma = 3$
SUPER-HOT COMPONENT
$T_e = 31 \times 10^6$ °K
$n_e n_i V = 3.6 \times 10^{48} cm^{-3}$
PHOTONS / (cm^2·sec·keV)
10^3
10^2
10
1
10^{-1}
10^{-2}
10^{-3}
10
10^2
ENERGY (keV)

Figure 3-2

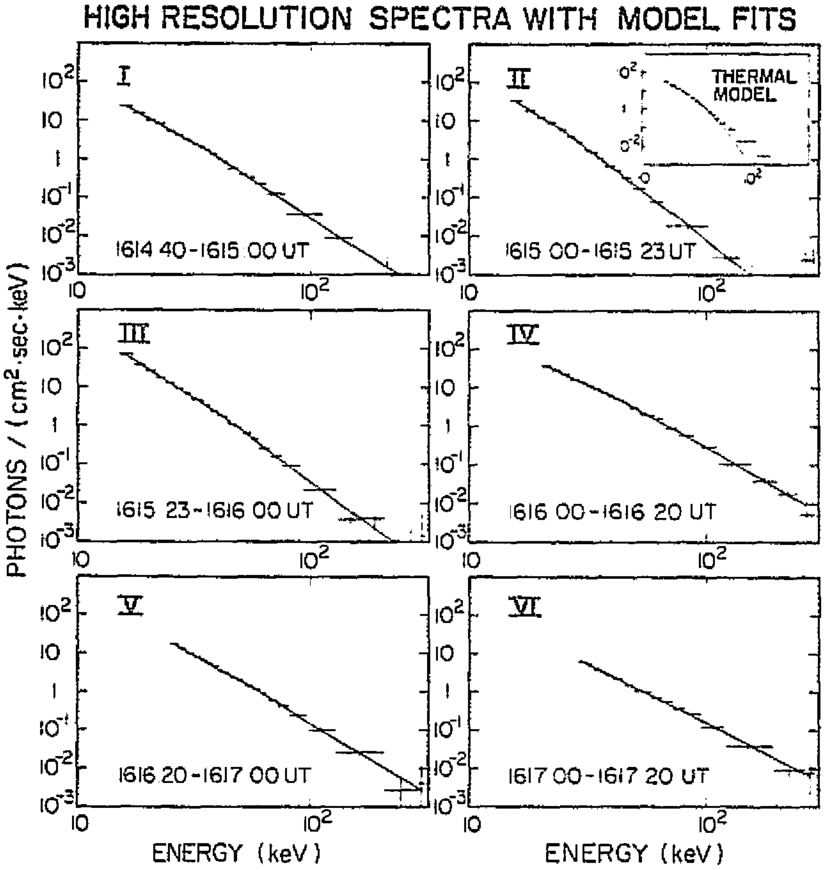
HIGH RESOLUTION SPECTRA WITH MODEL FITS
PHOTONS / (cm^2·sec·keV)
ENERGY (keV)
10
10^2
10^2
10
1
10^{-1}
10^{-2}
10^{-3}
I
1614 40-1615 00 UT
II
1615 00-1615 23 UT
THERMAL MODEL
III
1615 23-1616 00 UT
IV
1616 00-1616 20 UT
V
1616 20-1617 00 UT
VI
1617 00-1617 20 UT

Figure 3-3

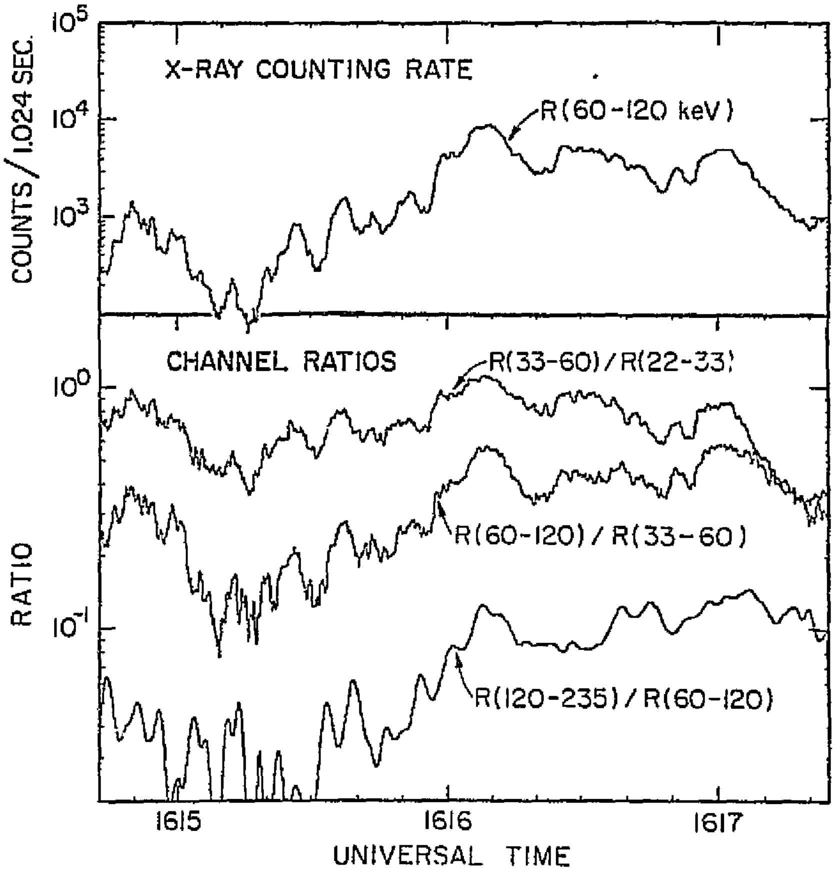
X-RAY COUNTING RATE
R(60-120 keV)
COUNTS/1.024 SEC.
10^5
10^4
10^3
CHANNEL RATIOS
R(33-60)/R(22-33)
R(60-120)/R(33-60)
R(120-235)/R(60-120)
RATIO
10^0
10^{-1}
1615
1616
1617
UNIVERSAL TIME

Figure 3-4

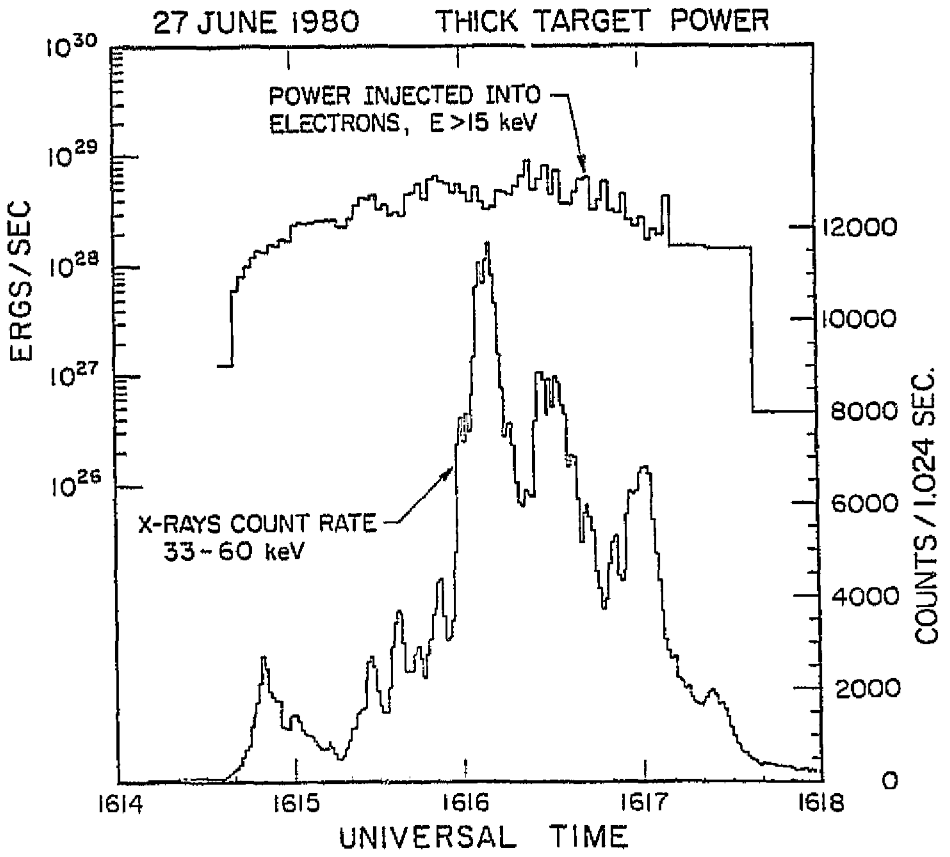
27 JUNE 1980
THICK TARGET POWER
POWER INJECTED INTO ELECTRONS, E >15 keV
X-RAYS COUNT RATE 33-60 keV
ERGS/SEC
10^{30}
10^{29}
10^{28}
10^{27}
10^{26}
COUNTS/1.024 SEC.
12000
10000
8000
6000
4000
2000
0
1614
1615
1616
1617
1618
UNIVERSAL TIME

Figure 3-5

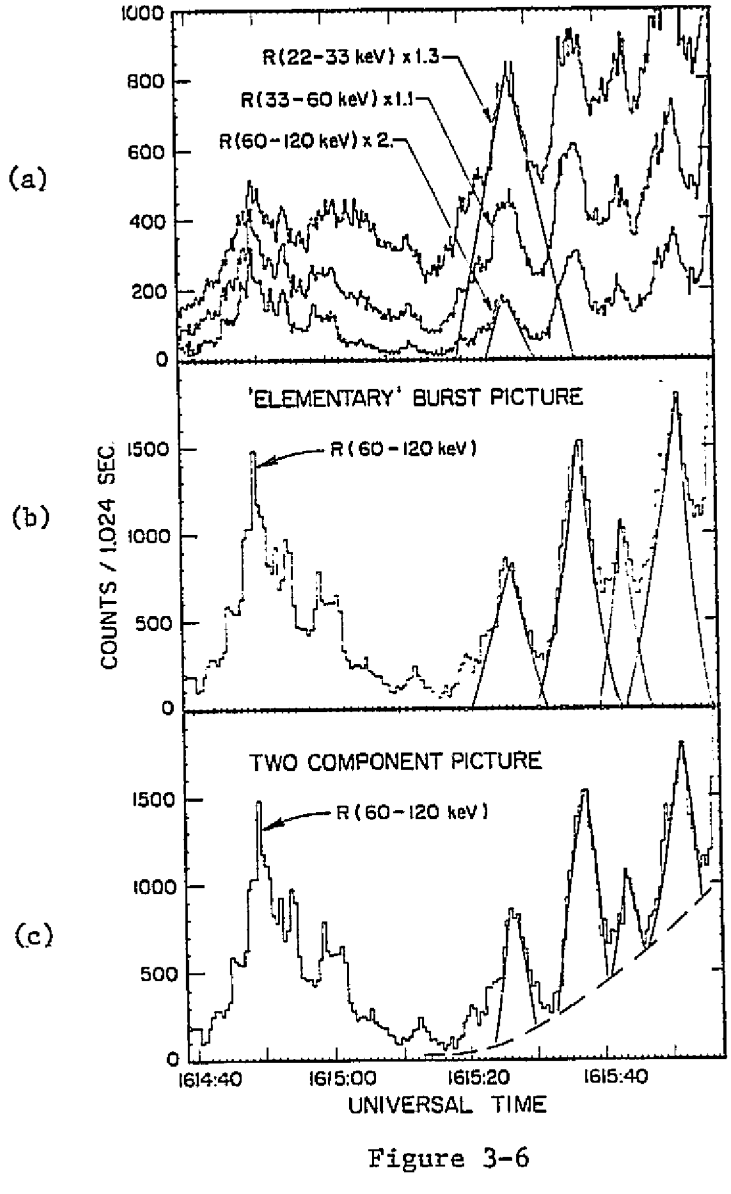
(a)
(b)
(c)
1000
800
600
400
200
0
R(22-33 keV) x 1.3
R(33-60 keV) x 1.1
R(60-120 keV) x 2.
'ELEMENTARY' BURST PICTURE
R(60-120 keV)
1500
1000
500
0
COUNTS / 1.024 SEC.
TWO COMPONENT PICTURE
R(60-120 keV)
1500
1000
500
0
1614:40
1615:00
1615:20
1615:40
UNIVERSAL TIME

Figure 3-6

ORIGINAL PAGE IS
OF POOR QUALITY

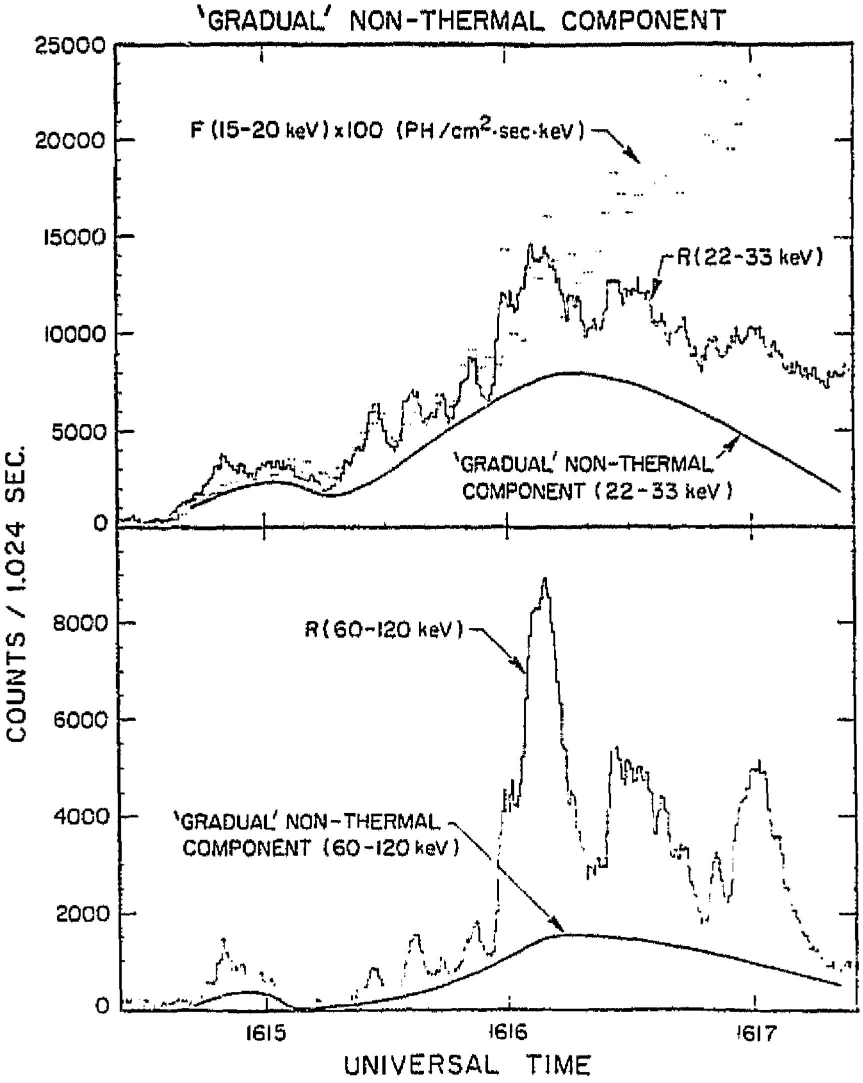

Figure 3-7

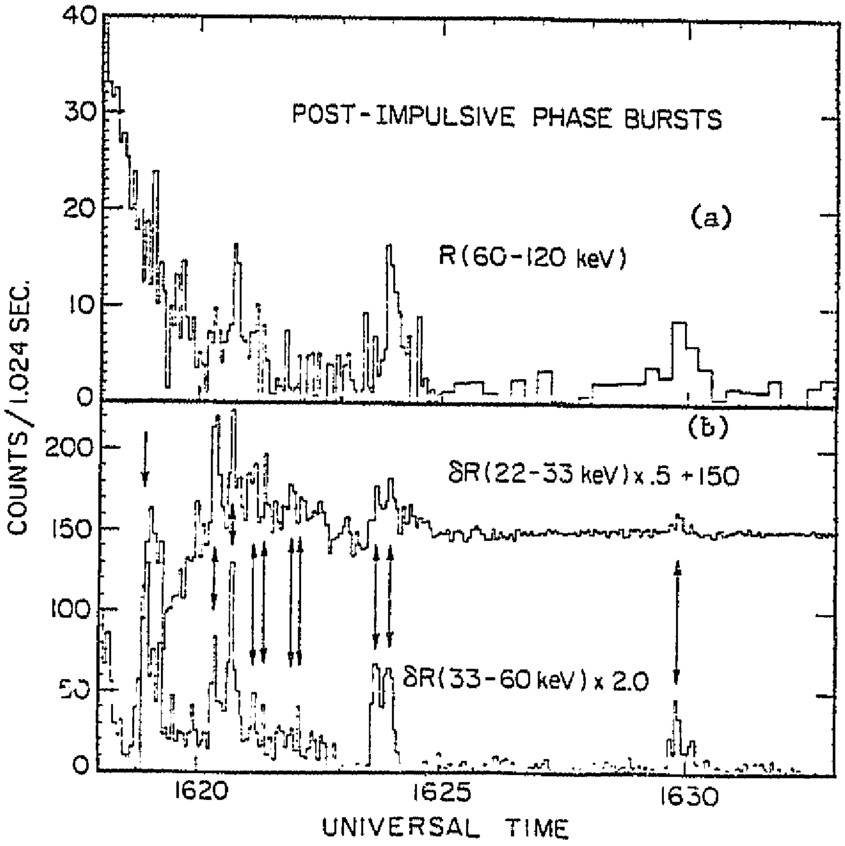
POST-IMPULSIVE PHASE BURSTS
(a)
R(60-120 keV)
(b)
δR(22-33 keV) x .5 +150
δR(33-60 keV) x 2.0
COUNTS/1.024 SEC.
40
30
20
10
0
200
150
100
50
0
1620
1625
1630
UNIVERSAL TIME

Figure 3-8

ORIGINAL PAGE IS
OF POOR QUALITY

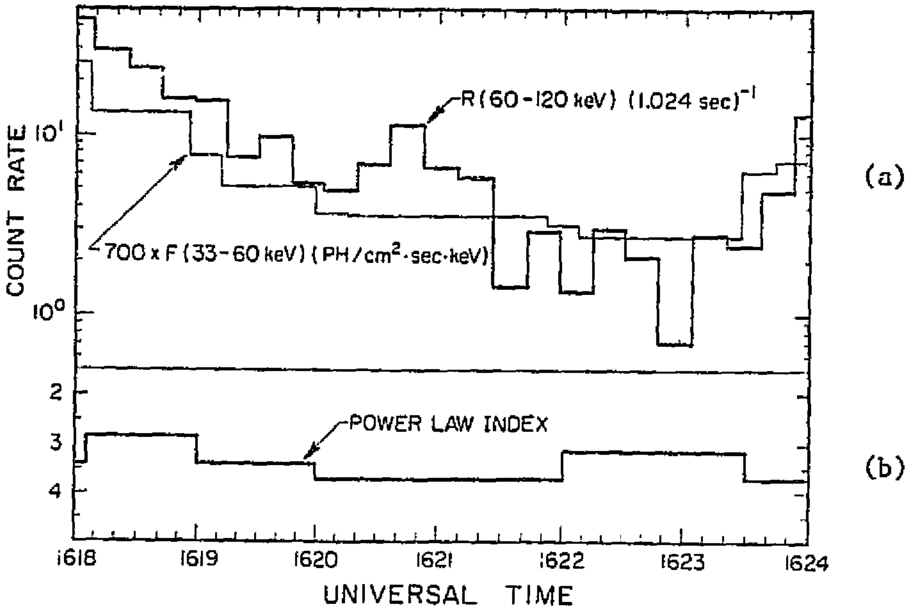

Figure 3-9

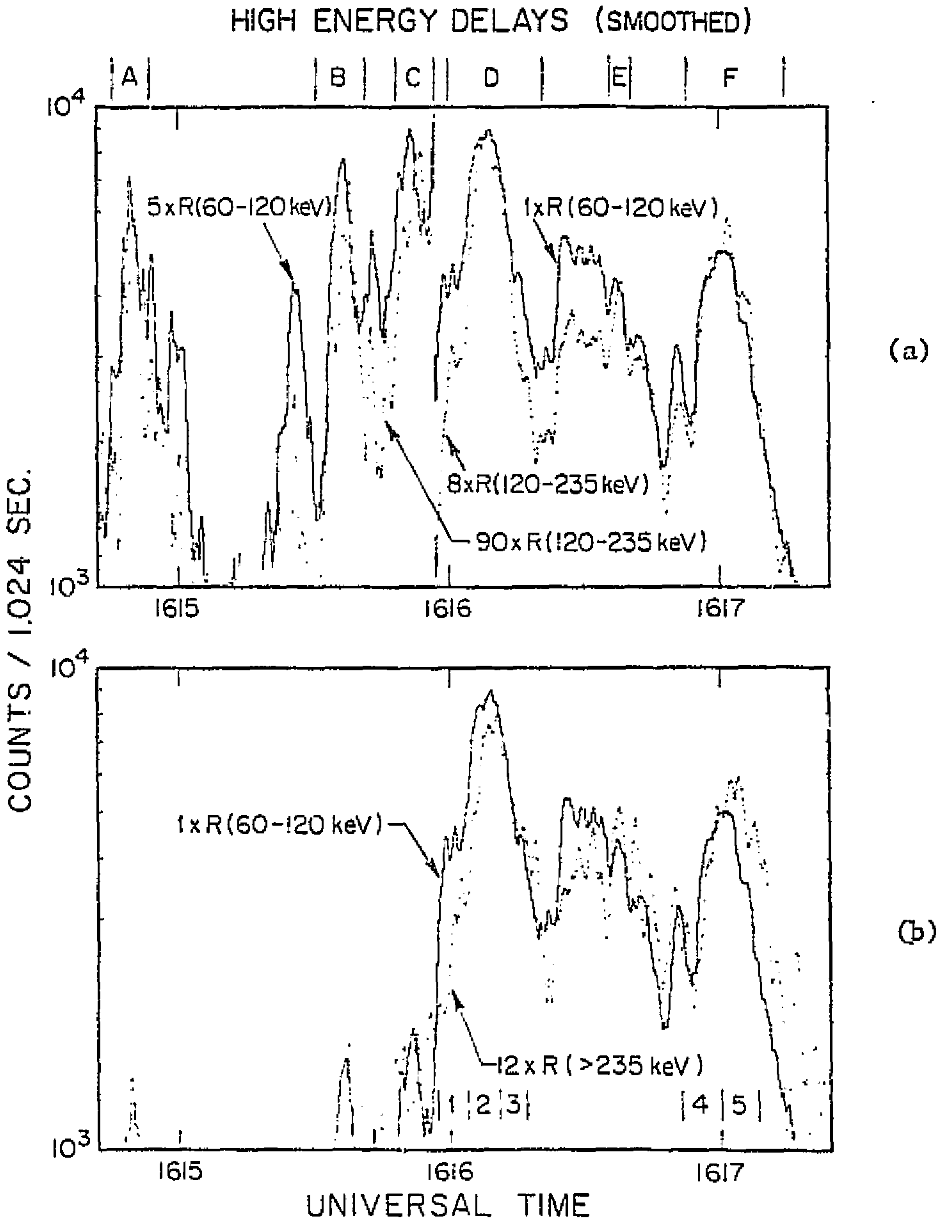
HIGH ENERGY DELAYS (SMOOTHED)
A
B
C
D
E
F
10⁴
10³
5xR(60-120 keV)
1xR(60-120 keV)
8xR(120-235 keV)
90xR(120-235 keV)
1615
1616
1617
(a)
COUNTS / 1.024 SEC.
10⁴
10³
1xR(60-120 keV)
12xR(>235 keV)
1
2
3
4
5
1615
1616
1617
(b)
UNIVERSAL TIME

Figure 3-10

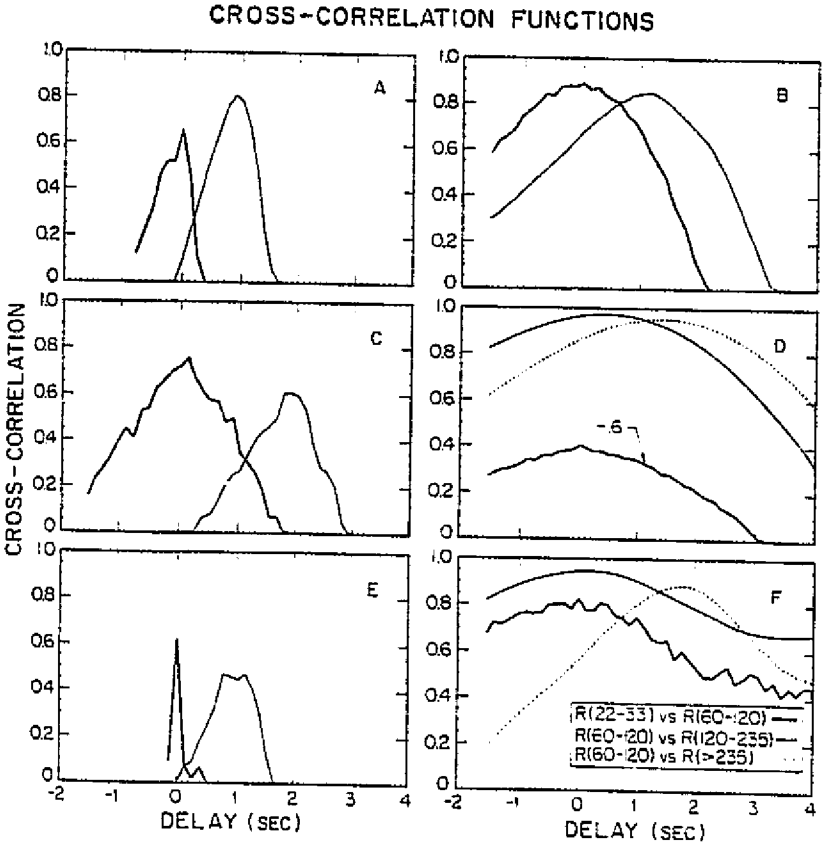
CROSS-CORRELATION FUNCTIONS
A
B
C
D
E
F
-.6
CROSS-CORRELATION
DELAY (SEC)
DELAY (SEC)
0
0.2
0.4
0.6
0.8
1.0
-2
-1
0
1
2
3
4
R(22-33) vs R(60-120)
R(60-120) vs R(120-235)
R(60-120) vs R(>235)

Figure 3-11

ORIGINAL PAGE IS
OF POOR QUALITY

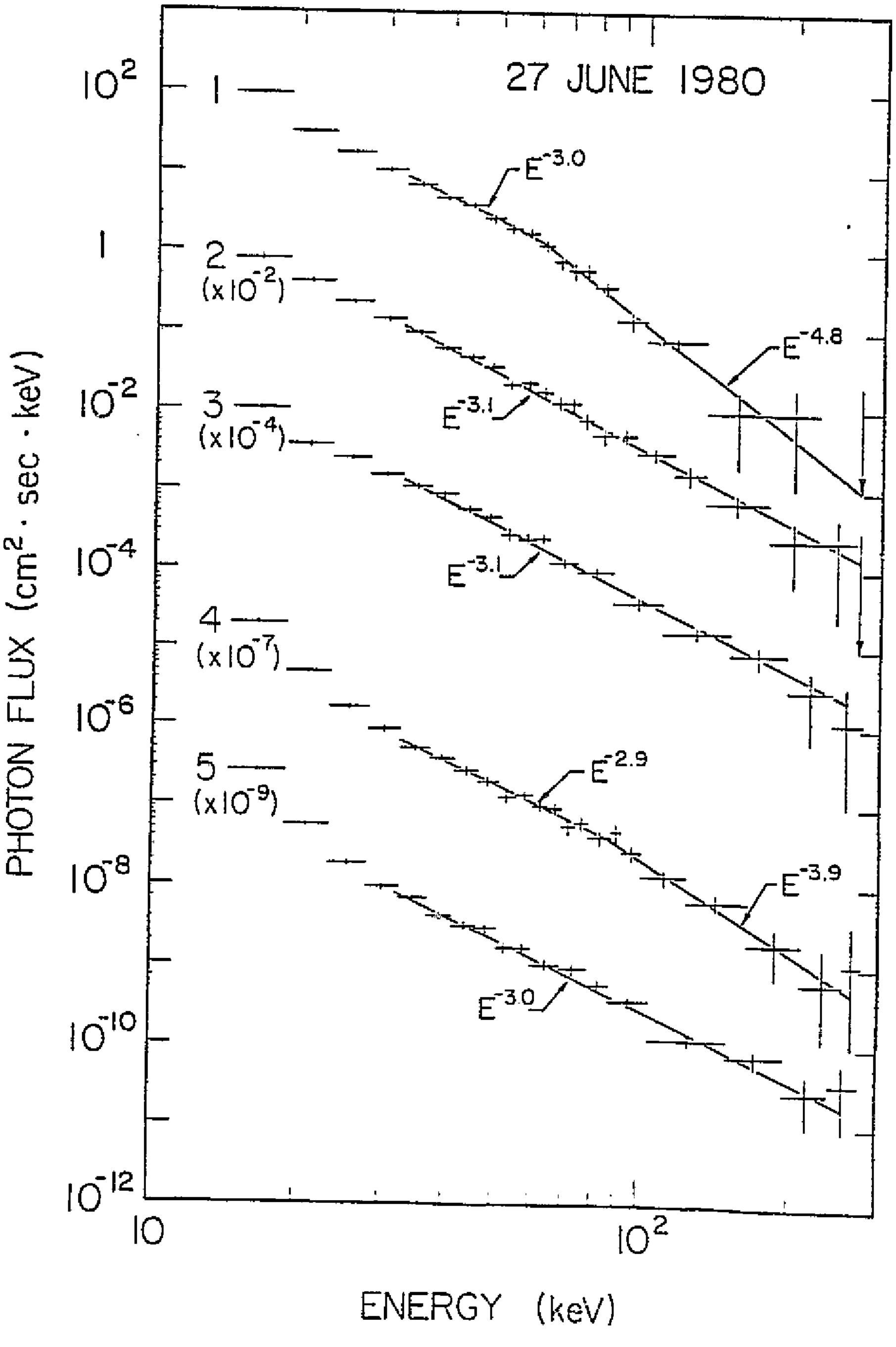

Figure 3-12

ORIGINAL PAGE IS
OF POOR QUALITY

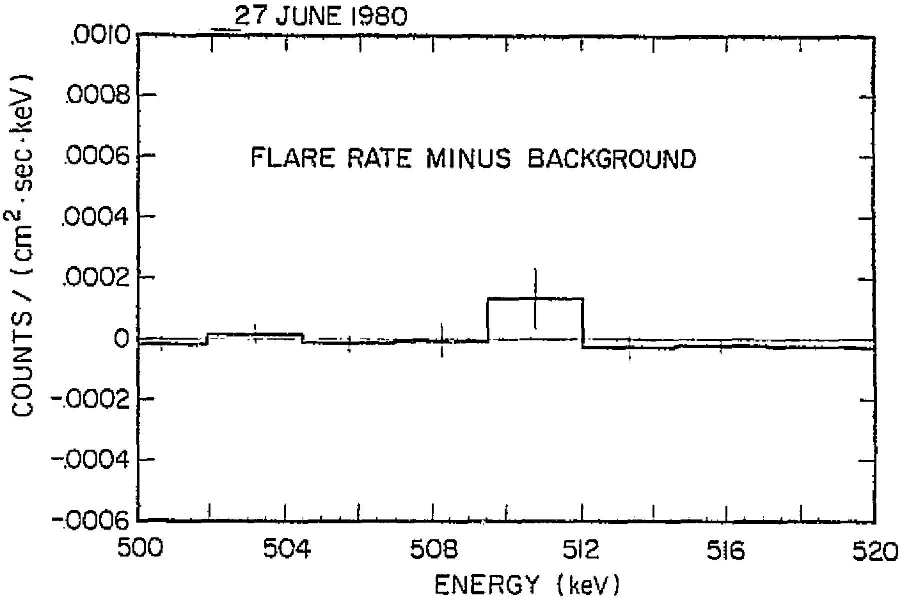

Figure 3-13

FOUR

Super-Hot Component

4-A. Introduction

Solar flares produce hot thermal plasmas which are contained in loops [*Moore* 1980]. Prior to our observations, it was believed that the highest temperatures reached within these loops was 20—25 × 10^{6}°K. With our high resolution measurements of the flare hard X-ray spectrum, we discovered a super-hot flare plasma component with a peak temperature of close to 35 × 10^{6}°K. This was present at the same time that soft X-ray monitors (GOES 2 ionization chambers) showed the usual much cooler flare plasma at 10—20 × 10^{6}°K. This super-hot component is likely to be the hottest truly thermal plasma in the flare. This chapter explores the role of this super-hot component within the flare.

4-B. Observations

To examine the longer term evolution of the flare, the germanium spectrometer data were accumulated over the 15 time intervals of Figure 4-1 The corresponding highly accurate photon spectra are displayed in Figure 4-1 with the data binned to 1.12 keV at low energies. At higher energy, the bins are wider for increased statistical accuracy. At the start of the event, the spectra are accurately power-law ($\gamma \sim 3.5$) from 13 to ~40 keV, with a steepening at higher energies.

Beginning near the peak of the event at ~1616 UT, a new, very steep component is observed at low energies, superposed on the power-law. At its steepest, this new component has a power-law index g~11, where $(dJ/dE) \propto E^{-\gamma}$. Such a steep spectrum is unresolvable by scintillation detectors. This steep component appears to vary much more slowly than the power-law component. After the rapid drop of the power-law component at ~1617 UT, it can be seen that the new steep component has a curved exponential like spectral shape. We have fit the X-ray spectrum to a combination of that expected from a single temperature Maxwellian electron distribution,

$$dn/dE_e = 2\pi\, n_e\, (\pi\, k\, T_e\,)^{-3/2}\, E_e^{1/2}\, e^{-E_e/kT_e}$$

at low energies, and a power-law at high energies. Here n_e and E_e refer to the electron number density and kinetic energy, respectively. The power-law component contributes insignificantly to the flux below ~30 keV. The X-ray spectrum from this distribution was computed for solar coronal abundances ($\overline{Z^2}$ = 1.8) using the differential X-ray flux $Is(E,T)$ in units of $\mathrm{ph\,cm^{-2}\,sec^{-1}\,keV^{-1}}$

$$Is(E,T) = 1.07 \times 10^{-42}\, \overline{Z^2}\, EM\, \frac{g(E,T)\, \exp^{(-E/T)}}{E\ T^{1/2}} \qquad (4\text{-}1)$$

where the photon energy E and electron temperature T are in keV, the emission measure EM is in $\mathrm{cm^{-3}}$, and the dimensionless Gaunt factor g(E,T) is taken from *Mätzler et al.* [1978].

Figure 4-2 shows the detailed fit for one of the time intervals. We have estimated the significance of the isothermal fit to the data below 33.5 keV, using the parameter estimation technique of *Lampton, Margon, and Bowyer* [1976]. The 90% confidence (χ^2_ν fit with 16 degrees of freedom) region in the temperature/emission measure plane is also shown in Figure 4-2. The best-fit temperature is 30.1×10^{6}°K, and the emission measure is $2.5 \times 10^{48}\,\mathrm{cm^{-3}}$. We call this plasma and its hard X-ray emission the super-hot component (SHC). Good fits to isothermals are obtained throughout the decay phase (>1618 UT) of the event. Thus, the

SHC spectrum is consistent with that of an isothermal electron distribution essentially throughout its existence. The evolution of this component is shown in Figure 4-3. The maximum temperature of 33.6×10^{6}°K is reached at ~1617:15 UT, and the maximum emission measure of $5 \times 10^{48}\,\mathrm{cm}^{-3}$ is attained at ~1617:30 UT. Although this component is present after ~1616:20 UT, we exclude the fits prior to 1616:50 UT because there may be a significant distortion of the fit due X-ray emission around 15 keV from an intensely emitting lower temperature plasma. Also, we know from the ISEE-3 proportional counter data [Kane, private communication] that the SHC is present until at least 1636 UT. (The ISEE-3 proportional counter had two channels at ~10-14 keV which are well suited for detecting the very late decay phase when the observable emission falls below the balloon detectors' atmospheric cutoff of 14 keV.) After 1626:50 UT, the statistical uncertainty in the temperature and emission measure fit becomes too large to be included in a detailed examination of the temporal evolution.

To investigate the relationship of this SHC to the soft X-ray producing thermal flare plasma which has been studied previously [*Moore et al.* 1980], we have used 1-8 Å and 0.5-4 Å ionization chamber data from the GOES 2 spacecraft [R. Donnelly, private communication]. We shall refer to this flare plasma as the soft X-ray plasma (SXR). The GOES data were fit to a single temperature and emission measure using the GOES 2 chambers' response functions [*Donnelly, Grubb, and Cowley* 1977] and the calculated X-ray emission as a function of temperature for an isothermal coronal gas [Wendt, private communication; *Mewe* 1972; *Tucker and Koren* 1971]. The maximum temperature reached by the SXR is 19×10^{6}°K, well below that of the SHC, and maximum emission measure is $4 \times 10^{49}\,\mathrm{cm}^{-3}$, a factor of ~ 10 larger. In our energy range (>13 keV) the X-ray emission of this flare plasma is usually negligible compared to the observed X-ray flux (Figure 4-2). Since the SXR usually consists of a continuous distribution of emission measures with temperature [*Moore et al.* 1980], the SHC identified here may be the highest temperature portion of this distribution. In that case, these observations show that the SXR at least occasionally extends up to ~35 $\times 10^{6}$°K. Both the emission measure and temperature of the SHC, however, show temporal variations quite different from those of the SXR (Figure 4-3). Note the fall in the SHC temperature from ~1617:20 to 1618 UT, quite independent of the slow smooth increase in temperature of the flare plasma from 1615 to 1618 UT. The SXR plasma cools significantly from 1618 to 1622 UT as its temperature falls from ~19 × 10^{6}°K to ~13 × 10^{6}°K, while over this same time the SHC maintains a temperature very close to 30 × 10^{6}°K but drops in emission measure by a factor of four. This cursory analysis suggests that the SHC is not simply the hottest portion of the soft X-ray emitting loops. If they occupy the same loop, then their relationship is determined mainly by thermal conductivity, plasma emissivity, and energy input.

Below we consider several models for producing the SHC and the SXR emission. In the first model all of the SHC and SXR plasma is contained within a single loop of uniform cross-section with the foot-points anchored in the cool chromosphere. The size of the SHC is estimated from observations by HXIS, the hard X-ray imaging instrument on the Solar Maximum Mission spacecraft. We compute the loop pressure, assumed uniform along the loop, from the SHC emission measure and the SHC volume. From the pressure the density is obtained as a function of temperature, which allows us to estimate the radiated power from the loop. We find, though, that this model is inconsistent because the downward heat flux from the SHC is much greater than the computed radiated power from the rest of the loop. To resolve this problem we try a second model where all of the SHC and SXR plasma is confined within a collection of identical, dense filamentary loops. These filaments are distributed throughout the HXIS volume, but fill only ~1/60th of this volume. The plasma density is chosen to be high enough to radiate all of the downward heat flux. While this is a more consistent model, the SHC energy loss rate seems too high to be compatible with the observed decay and possible energy inputs. In the third model we consider a collection of dense filaments which have a distribution of peak temperatures. Using the quasi-static model of *Rosner et al.* [1978] for the structure of the SHC loops, we obtain a decay rate which is compatible with the observation. In this isobaric (along the loop but changing in time) constant cross-section model, the loop structure is determined analytically by balancing the local radiative losses, the change in internal energy, and the change in conductive flux. The total cross-section for the SHC loops is obtained by matching the model hard X-ray flux to that observed. We find that only about 20% of the SXR plasma is contained in these SHC loops, with the rest contained in other loops with lower peak temperature.

4-C. Single Loop Model

HXIS Data

The HXIS instrument on the SMM spacecraft [*Van Beek et al.* 1980] images solar flare X-rays with moderate angular and energy resolution from 1-30 keV. Unfortunately, SMM was in earth shadow until just after 1630 UT, but HXIS did observe the flare during the time immediately following 1631:27 UT. The counts in each pixel (coarse field 32"x32" per pixel) over 23.5 seconds for the 11.5-16 keV and 8-11.5 keV channels are shown in Figure 4-4. Because the fields of the pixels overlap, it is possible to determine the extent of the source within a single pixel from the relative count rate of the neighboring pixels. As an example, consider a source which is uniformly bright over the field (FWHM) of a single pixel. Because the collimator response function is triangular, 32" FWHM, and overlaps the neighboring pixels, each of the horizontal and vertical neighbors would have 1/6th the counting rate of the bright pixels. Applying this reasoning to the data in Figure 4-4, we have estimated that the source in both of these channels subtends a solid angle of ~12"x36".

We can estimate the relative contributions to the HXIS count rates from the SHC and from the cooler SXR at 1631:30 UT. Table 4-1 shows that the SHC flux dominates above 11.5 keV while the SXR flux may be nearly as intense in the 8-11.5 keV channel. Thus, we conclude that we are actually estimating the size of the SHC with the 11.5-16 keV data.

Table 4-1 HXIS intensity as a function of T_e and energy.

Flux from Soft X-ray Plasma vs. Super-Hot Component	SXR	SHC
Temperature	11.6×10^{6}°K	22×10^{6}°K
EM	$3 \times 10^{48}\ \mathrm{cm}^{-3}$	$1 \times 10^{47}\ \mathrm{cm}^{-3}$
Energy	Flux ph $\mathrm{cm}^{-2}\ \mathrm{sec}^{-1}\ \mathrm{keV}^{-1}$	Flux
8 KeV	64	104
11.5 keV	1.1	9.5
16 keV	.0065	.27

The active region of this flare is located on the sun at 67°W and 27°S. If the source is thin and lies parallel to the surface then we may see only 38% of the true area. However, the long direction of the image is in the N-S direction and may not be appreciably distorted. Taking these errors into account the scale size of the SHC is $\sim 1-4 \times 10^9$ cm.

Physics of Hot Coronal Loops

Before we can discuss our three specific models for the SHC and the SXR, we need to understand the physics of these hot plasmas. The SHC is in some ways a hotter version of the SXR which, as we know from Skylab pictures [*Moore et al.* 1980], is configured into a loop structure defined by the magnetic field. The magnetic field inhibits any mass or heat transport perpendicular to the field so the physics is essentially one-dimensional provided the confining field is sufficiently strong

The thermal conductive flux F_c is given by the *Spitzer* [1962] formula

$$F_c = -10^{-6} T^{5/2}\, dT/ds \quad (\mathrm{ergs\ cm^{-2}\ sec^{-1}}) \tag{4-2}$$

Here s is the coordinate which runs along the magnetic field and runs from s=0 at the base to s=L/2 at $T_{\max}$ for our symmetric loop. Note that F_c is independent of the plasma density. F_c is derived from classical diffusion where the mean free path, l, of the energy carrying electrons is much smaller than the temperature gradient scale length. The density drops out of the heat flux because the number of carriers varies as the density, but the range of the carriers varies as the inverse of the density. The range is important because the difference in the energy flux at

s scales with the difference in average energy of the carriers at the site of their last collision, $s-l$ and $s+l$. Later we show that our loop probably has a density high enough that l is sufficiently small, compared to the temperature gradient scale, for this diffusion approach to be valid.

Our model also requires that the pressure, p, be nearly uniform throughout the loop. The hydrostatic pressure gradient is not important because the temperature scale height is so large ($H > 10^{11}$ cm for $T_e = 3 \times 10^{6\circ}$K). Moreover, if large pressure gradients were maintained over time, then we expect that large velocities would develop. We can estimate the bulk velocity within the SHC over the time from 1618-1623 UT when the emission measure falls by ~4 within ~270 seconds. Since we believe that the volume of the SHC remains nearly constant through the decay, n must drop by 2 so that there must be a flow which covers $1/2\,(\mathrm{L}_{SHC}/2)$ in ~270 seconds. From the HXIS data we compute $\mathrm{L}_{SHC} = 36'' \times 7.28 \times 10^7 = 2.6 \times 10^9$cm. Thus, for the velocity at the SHC-SXR boundary we obtain $v_{SHC} \sim 25$ km sec^{-1} which is well below the ion sound speed (~ 500 km sec^{-1}). We determine the loop gas pressure p from

$$\mathrm{p} = 2\, n_e k\, (T_i + T_e) \tag{4-3}$$

The equipartition time for ions and electrons [*Spitzer* 1962] is given by

$$\tau_{eq} = (10/n)\, T_e^{3/2}$$
$$= 165 \text{ sec for } n = 10^{10} \text{ cm}^{-3} \text{ and } T_e = 30 \times 10^{6\circ}\text{K}.$$

The HXIS image also gives us a crude upper limit to the loop cross-sectional area $\mathrm{A} \lesssim \pi \times (6'' \times 7.28 \times 10^7 \text{ cm})^2$ which yields $\mathrm{A} \lesssim 6 \times 10^{17}$ cm^2. From the SHC emission measure, EM_{SHC}, at 1618 UT of 3.9×10^{48} cm^{-3} we obtain $n \gtrsim 5 \times 10^{10}$ cm^{-3}. Therefore, τ_{eq} must be less than 30 seconds which is short compared to the time scale of the decay. So we take $T_e = T_i$ for the loop at all times.

Our first model is of a single loop of constant cross-section which contains all of the SHC and SXR. The loop volume completely fills the HXIS "image". The pressure is nearly uniform throughout the loop. The pressure is computed from the temperature, volume, and emission measure of the SHC. The conductive flux out of the SHC is estimated using the scale length from HXIS. The SXR radiative loss rate is estimated using its emission measure times the radiative loss function, $R(T)$ [*Rosner et al.* 1978]. For this model to be self-consistent, the cooler portion of the loop, designated EUV for extreme ultra-violet, must be dense enough to radiate the heat flux flowing out of the SXR loop. The power radiated by the EUV portion of the loop is calculated by integrating $R(T)$ over the estimated differential emission measure.

First, estimate F_c leaving the SHC. Crudely dT/ds is given at $25 \times 10^{6\circ}$K by

$$dT/ds \sim \frac{(30 \times 10^{6\circ}\mathrm{K} - 25 \times 10^{6\circ}\mathrm{K})}{(\mathrm{L}_{SHC}/2)} \tag{4-4}$$

which is $\sim 3.8 \times 10^{-3}\,\mathrm{cm}^{-1}$ for $\mathrm{L}_{SHC} \sim 2.6 \times 10^{9}$cm. Thus by Equation (4-2), $F_c \sim 1.2 \times 10^{10}\,\mathrm{erg\,cm^{-2}\,sec^{-1}}$ which should be accurate to within a factor of ~ 2. For $\mathrm{A} = 6 \times 10^{17}\,\mathrm{cm}^2$, the conductive energy flow from the SHC is $2F_c\mathrm{A} \sim 1.5 \times 10^{28}\,\mathrm{erg\,sec^{-1}}$.

The power radiated from the SXR is

$$P_{SXR} = n\ n\ R(T_e)\ dV = EM_{SXR}\ R_{SXR}$$

R_{SXR} is the emissivity averaged over $R(T)$ assuming a flat differential emission measure with T. Based on the GOES response functions, $5 \times 10^{6\circ}\mathrm{K} \lesssim T_{SXR} \lesssim 25 \times 10^{6\circ}\mathrm{K}$. We estimate $R_{SXR} \sim 3 \times 10^{-23}\,\mathrm{erg\,cm^3\,sec^{-1}}$, so that at 1618 UT, when $EM_{SXR} = 4 \times 10^{49}\,\mathrm{cm}^{-3}$, $P_{SXR} \sim 1.2 \times 10^{27}\,\mathrm{erg\,sec^{-1}}$.

We see that the total downward heat flux, $2F_c\mathrm{A} \sim 1.5 \times 10^{28}\,\mathrm{erg\,sec^{-1}}$, is hardly reduced by a radiative loss of $P_{SXR} \sim 1.2 \times 10^{27}\,\mathrm{erg\,sec^{-1}}$. Thus, the EUV portion of the loop must radiate the bulk of the heat flux for this model to work. The heat flux into the EUV region is given by

$$F_c\ (5 \times 10^{6\circ}\mathrm{K}) = F_c\ (25 \times 10^{6\circ}\mathrm{K}) - P_{SXR}/2A \sim 1.1 \times 10^{10}\,\mathrm{erg\,cm^{-2}\,sec^{-1}}$$

At 1618 UT we infer the pressure from the SHC volume and emission measure to be

$$p = (EM_{SHC}/(L_{SHC}A))^{1/2}\, 2k\, T_{\max} = 400\,\mathrm{dy\,cm^{-2}}$$

The radiated power, per unit cross-section, is computed by integrating $R(T)$ over $n^2 ds$. Using (4-2) gives us ds/dt and replacing n with $p/(2kT)$ we obtain

$$\frac{P_{EUV}}{2A} = \int_{base}^{apex} n^2\, R(T)\, ds = \int_{T=T_0}^{T=5\times10^{6\circ}K} -p^2\, 10^{-6} R(T)\, T^{1/2}/(F_c(T)\, 4k^2)\; dT \qquad (4\text{-}5)$$

Here we clearly see that the larger F_c is, the smaller the radiated power. In fact, $\frac{P_{EUV}}{2A}$ (4-5) may be estimated by replacing $F_c(T)$ with 1/2 F_c incident on the EUV region from the SHC. Using an approximation of *Rosner et al.* [1978] for this integral over T,

$$\frac{P_{EUV}}{2A} \sim f_R(T^*)/F_c(T^*) \text{ for } T^* = 5\times10^{6\circ}\mathrm{K} \qquad (4\text{-}6)$$

where $f_R(T)$ is given by

$$f_R(T) = 4.16\times10^{6}\, p^2\, T \text{ for } T > 126{,}000^{\circ}\mathrm{K} \qquad (4\text{-}7)$$

Thus, $\frac{P_{EUV}}{2A} \sim 3\times10^{8}\,\mathrm{ergs\,cm^{-2}\,sec^{-1}}$ which is much less than the incident $F_c \sim 1.1\times10^{10}\mathrm{ergs\,cm^{-2}\,sec^{-1}}$. Clearly, the EUV loop cannot radiate this heat flux at this pressure. In fact for a consistent loop model, the pressure of the loop may be found by equating $\frac{P_{EUV}}{2A}$ and F_c incident on the EUV in (4-6). Thus, for a consistent loop model,

$$\frac{P_{EUV}}{2A} \sim (f_R(T{=}5\times10^{6\circ}\mathrm{K}))^{1/2} \qquad (4\text{-}8)$$

Moreover, F_c is the **minimum** heat flux incident on the EUV. The falling emission measure of the SHC after 1618 UT indicates downward mass flow carrying additional energy. This phenomenon is called coronal ‘condensation’. (The reverse process, indicated by a rising *EM* at high temperature, is termed chromospheric ‘evaporation’.) The additional convective energy flux is comprised of the material transport of plasma energy and pdV work done by the gas. This is given by the enthalpy flux

$$F_e = 5/2\ p\ v \qquad (4\text{-}9)$$

Thus, this model is not self-consistent. The EUV density is too low to radiate the incoming heat flux. To make this loop model consistent, either F_c must be lower or the plasma must be dense enough to radiate the high heat flux.

Duijveman [1983] examined a SHC loop model with a reduced F_c due to anomalous heat conduction. Equation (4-2) for F_c is not valid when the electron mean free path, l, is comparable to the temperature gradient scale length, $S=T(ds/dT)$. *Duijveman* [1983] expects a minor reduction (factor of ~2) from the classical conductivity for $l/S>.01$ and serious limitation of F_c for $l/S \sim .1$. If we take $ds/dT \sim 300$ cm as constant throughout the loop we may estimate l/S by

$$\begin{aligned} l/S &= (3.9\times 10^5\ T^{1/2}\ /\ 91\ n\ T^{-3/2})/\ 300\ T \\ &\sim 3\times 10^{-15}\ T^2\ /\ \mathrm{p} \end{aligned} \qquad (4\text{-}10)$$

For $T = 30\times 10^{6\,\circ}$K and $\mathrm{p} = 400 \mathrm{dy\,cm^{-2}}$, we find that $l/S < .007$ everwhere which means that the classical conductive flux is valid for the SHC. Also, for any smaller V_{SHC}, the classical formula for the conductive flux is valid for the SHC plasma at 1618 UT. Thus, we must investigate the other possibility of loops of higher density and smaller cross-section.

Filamentary Loop Models

In this filamentary model there are a collection of dense, identical loops distributed throughout the apparent HXIS 'volume'. The pressure is uniform along the loop and the physics is one-dimensional. The SHC and the SXR are totally contained within these loops. This time we choose the pressure/density of the loop high enough that the energy loss can be radiated.

The total energy flux out of the SHC is the conductive flux F_c plus the enthalpy flux F_e=5/2 pv. This must be balanced by the radiative energy loss per unit cross-sectional area by the SXR and the EUV plasmas. Since the loop pressure is falling everywhere, the SXR and the EUV are radiating their own energy loss, $dE/dt<0$, too. In short, the radiative loss must equal the energy input within the SHC and EUV portion of the loop,

$$P_{EUV} + P_{SXR} = 2\mathrm{A}(F_c + F_e) + dE/dt. \tag{4-11}$$

All of the terms in (4-11) may be expressed as either constant, linear, or quadratic in $\sqrt{\mathrm{A}}$ at 1618 UT. Since $\mathrm{L}_{SXR} >> \mathrm{L}_{EUV}$, $dE/dt \sim 1.5\mathrm{AL}_{SXR}\, d\mathrm{p}/dt$. Because the emission measure ratio of the SXR to the SHC is ~10/1 and the density ratio is ~2/1, the ratio of the volumes should be ~$10/2^2$~2.5. Thus, L_{SXR} is ~$2.5\mathrm{L}_{SHC}$. Computationally, it turns out that $dE/dt \sim 3\mathrm{A}F_e$. In cgs units, the other terms are

$$F_c \sim 1.2\times 10^{10},\ F_e \sim \mathrm{p}1.3\times 10^{7},\ P_{SXR} \sim 1.2\times 10^{27},\ \text{and}\ P_{EUV} \sim 2\mathrm{A}(f_R\,(T^*))^{1/2}.$$

p is given by

$$\mathrm{p} = (\ EM_{SHC}\ /\ \mathrm{L}_{SHC}\ A\ )\ 2\ k\ \ T = 3.2\times 10^{11}\ /\ \sqrt{\mathrm{A}} \tag{4-12}$$

Solving for A we obtain

$$\mathrm{A} = 1.3\times 10^{16}\,\mathrm{cm}^2 \text{ and } \mathrm{p} = 2850\,\mathrm{dy\,cm}^{-2}.$$

The energy loss from the SHC is $2\mathrm{A}(\ F_c + F_e\ ) + P_{SHC} \sim .88\times 10^{27}\,\mathrm{erg\,sec}^{-1}$ while $E_{SHC} \sim 1.5\times 10^{29}\,\mathrm{erg}$ at 1618 UT. The cooling time for the SHC is given by $t_c = 1.5\times 10^{29}\ /\ .88\times 10^{27}\,\mathrm{sec} \sim 170\,\mathrm{sec}$. But the SHC lasts with $T_{\max} \sim 30 \times 10^{6}$°K for ~ 300 sec and $T_{\max} > 25 \times 10^{6}$°K for ~600 sec. Because the SHC persists beyond t_c, there must be an additional heat input of the order of $5\times 10^{26}\,\mathrm{erg\,sec}^{-1}$.

In the previous chapter we learned that there are non-thermal electrons accelerated and stopped during the decay phase. However, even if their spectrum extends to as low as 15 keV they carry an average of less than $10^{26}\,\mathrm{erg\,sec}^{-1}$ over 1618-1622 UT and even less power afterwards. We note that the energy in the electron spectrum increases by about 10 for every 50% drop in the low energy cutoff. Another possibility is that there could be some other mode of energy input to the SHC. But observationally, there is no direct evidence of such a heat source.

We try a third filamentary loop model where we do not require the SHC and the SXR to come from the same identical loops. Instead, there are a set of loops with a distribution of maximum temperatures. The loops are modeled by a static model, where v and $F_e \sim 0$. This is consistent with the change in the conductive flux being given by the local radiative loss minus the local change in internal energy. The model is similar to that of *Rosner et al.* [1978] for steady-state coronal loops but we substitute the local energy loss for the heat input in their energy balance equation. In this model we are explicitly ignoring the fluid equations of motion and assuming that changes take place slowly between a series of quasi-static states. Since this model is best for small F_e, we match the model to the data at 1622-1623:30 UT when the SHC emission measure is barely changing (implying that $v \sim 0$). The differential emission measure of the loop plasma is determined analytically from the local energy balance. Using this differential emission measure, we find the total cross-section A of the SHC loops by matching the observed hard X-ray flux. Using this A, the total energy and the energy loss rate can be computed for the SHC plasma.

The local energy balance includes the local energy loss rate, $(\partial\epsilon/\partial t)\, ds$, the change in the conductive flux, dF_c, and the local radiative loss, $n^2 R(T)\, ds$,

$$dF_c = -n^2 R(T)\, ds - (\partial\epsilon/\partial t)\, ds. \tag{4-13}$$

We integrate (4-13) over T to find the conductive flux by replacing ds with $ds\, dT/ds$ using (4-2) and replacing n with $p/(2kT)$. Thus,

$$F_c^2(T) = f_R(T) - f_H(T) \tag{4-14}$$

because F_c is negligible at the low temperature boundary. $f_H(T)$ is given by

$$f_H(T) = \int_{T=T_0}^{T=T_{\max}} 2\times 10^{-6}\, (-\partial\epsilon/\partial t)\, T'^{5/2} dT' \tag{4-15}$$

During the decay, $-\partial\epsilon/\partial t$ is always greater than zero. To obtain s(T) we integrate (4-2) over T using (4-14),

$$s(T) = 10^{-6} \int_{T=T_0}^{T=T_{\max}} dT' T'^{5/2}\, (f_R(T') - f_H(T'))^{-1/2} \tag{4-16}$$

The denominator in the integral in (4-16) vanishes only at the loop apex, $s_{\max}$. Also, pressure balance should make $\partial\epsilon/\partial t$ constant over the loop so (4-16) is readily solved. The total loop length is

$$L/2 \sim 1/p \times (T_{max}/1400)^3 \text{ for } T > 10 \times 10^{6\circ}\text{K} \qquad (4\text{-}17)$$

We show the loop structure in Figure 4-5 where we display $F_c(T)/F_{c_{max}}$ and $s(T)/(L/2)$ vs. T/T_{max}. Normalized this way, these curves are valid for all L and $T > 10 \times 10^{6\circ}$K. The differential emission measure within the loop is given by

$$DEM(T) = \frac{p^2\, 10^{-6}\, T^{1/2}}{4\, k^2\, F_c} \qquad (4\text{-}18)$$

We can use this differential emission measure to compute the hard X-ray flux per unit cross-section at 1622-1623 UT. For the moment we assume that the total loop length, L, is 4×10^9cm (Later we show that this is consistent with $L_{SHC} \sim 2.6 \times 10^9$cm.). Using this L and $T_{max} = 29.3 \times 10^{6\circ}$K, then $p = 4500$dy cm^{-2} by (4-5). Since a single temperature spectral model was used to fit the hard X-ray flux, the cross-section A is obtained as a function of photon energy E when we compare the single temperature model to the model which is differential in T.

$$I(E,T_{max})\, EM_{SHC} = 2\, A \int_{T_0}^{T_{max}} DEM(T')\, I(E,T')\, dT'$$

Thus, $.8 \times 10^{15} < A < 1.4 \times 10^{15}\text{cm}^2$. $A \sim 1.2 \times 10^{15}\text{cm}^2$ is a representative value. From p, A, and EM_{SHC}, we compute $L_{SHC} = 2.7 \times 10^9$cm and locate $L_{SHC}/L = .67$ in Figure 4-5. Thus, in Figure 4-5, we see that the low temperature boundary of the SHC plasma is given by $T/T_{max} = .83$ for $T_{max} \sim 30 \times 10^{6\circ}$K. As promised the filaments are dense. For a total loop cross-section of $1.2 \times 10^{15}\text{cm}^2$, the density peaks at $\tilde{\ }10^{12}\text{cm}^{-3}$.

Furthermore, computing the response of the GOES 2 ionization chambers to the SXR emission from this collection of SHC filaments, we can account for most of the emission in the .5-4 Å channel, but not the emission in the 1-8 Å channel. Therefore, there must be filaments which have a peak temperature much less than that of the SHC plasma.

Energy Budget of Filamentary Loops

Now we can specify all of the energy balance terms for the SHC. We write the SHC energy balance

$$0 = \dot{E} + P_{SHC} + 2A\,(\,F_c + F_e\,) - H$$

$\dot{E}$ is the time rate of change of E_{SHC}, the total energy of the SHC. For the SHC where $T \sim 30 \times 10^{6\circ}$K, $R\,(T)\ \sim 2 \times 10^{-23}$ erg cm^3 sec^{-1}. H is the total heat input into the SHC. Note that for the largest EM_{SHC} of 5×10^{48} cm^{-3}, $P_{SHC} \sim 10^{26}$ erg sec^{-1} which is well below $P_{SXR} > 10^{27}$erg sec^{-1}. Table 4-2 lists these energy loss/gain rates from 1616:50-1626:48 UT for L$\sim 4 \times 10^9$ cm and $A = 1.2 \times 10^{15}$ cm^2. During the decay phase, Table 4-2 shows that the heat input rate to the SHC should be $\sim 5 \times 10^{25}$ erg sec^{-1} to account for the $\dot{E}$ observed. We see that H is of the same order as the observed power in the decay phase non-thermal electron spectrum if the low energy cutoff extends to 15 keV (as it does during the impulsive phase).

This additional heat input may maintain the SHC temperature from 1618-1622 UT when $T_{\max}$ remains nearly $30 \times 10^{6\circ}$K while the emission measure of the SHC falls by a factor of 4.

Table 4-2 SHC Energy Balance for Quasi-Static Model

Super-Hot Component Energy Balance											
Time After 1600 UT	16:50	17:00	17:12	17:24	17:36	18:00	19:00	20:00	22:00	23:30	24:20 -26:46
EM_{SHC} 10^{48} cm^{-3}	2	3.5	3.2	5	4.1	3.9	2.5	1.6	1.0	1.0	.85
T $10^{7\circ}$K	3.13	3.10	3.36	3.21	3.25	3.03	3.01	3.00	2.93	2.78	2.55
E_{SHC} 10^{28}ergs	2.9	3.8	4.0	4.7	4.3	4.0	3.1	2.5	1.9	1.8	1.6
E 10^{26}ergs sec^{-1}	9.1	1.7	5.8	-3.3	-1.3	-1.5	-1.0	-1.0	-0.1	-0.4	
P_{SHC} 10^{26}ergs sec^{-1}	0.4	0.7	.64	1.0	.82	.78	.5	.32	0.2	0.2	.17
$2F_e$A 10^{26}ergs sec^{-1}	7.8	-2.2	6.8	-2.2	-1.1	-.9	-.8	-.65	0.	-.23	
$2F_c$A 10^{26}ergs sec^{-1}	-.5	-.5	-.65	-.55	-.6	-.45	-.45	-.45	-.40	-.33	-.24
H 10^{26}ergs sec^{-1}	1.5	5.0	.55	.3	1.0	.35	.57	.25	.43	.24	
P_{e15} 10^{26}ergs sec^{-1}	280	220	120	130	5.2	.9	.9	1.4	.3	2.	.1

Terms involving derivatives (F_e, $\dot{E}$, and H) are computed by taking the difference between two values and dividing by the time.

Since the SHC plasma must expand as it pushes some of the hot plasma downward, the temperature would fall without some additional heating. It may be that all of this heat is deposited in a small region which would be somewhat hotter than the $T_{\max}$ indicated by the fit to the emission from the single temperature plasma model.

Determining the fraction of the SXR plasma in the SHC loops is difficult without precisely determining the response of the GOES ionization chambers to the distribution of SHC plasma. Probably, the hotter plasma distorts the measured temperature of the SXR emission by making it seem hotter. This, in turn, probably results in an under-estimate of the SXR emission measure. Still, we can roughly estimate this fraction. First, $L_{SHC} \sim 2L_{SXR}$ within the SHC loops. Since the SXR is cooler we estimate that the average density is twice that of the SHC. Thus, the SXR emission measure should be ~2 times the SHC emission measure. The overall ratio EM_{SXR}/EM_{SHC} is ~10, so ~20% of the SXR plasma resides in the SHC loops. Thus, 80% of the SXR plasma must reside in loops with significantly lower maximum temperatures.

The maximum energy content of the SHC filaments is computed from

$$E_{total}=3/2\,p_{\max}V_{total}$$

At 1617:24, $E_{total} = 8 \times 10^{28}$ ergs. We estimate the energy content of the SXR filaments by taking their radiative loss rate, $P_{SXR} \geqslant 10^{27}\,\mathrm{erg\,sec^{-1}}$, multiplying by 2-3 for the EUV power, and integrating over a decay time of 500-1500 seconds giving a total thermal energy of ~1-$5 \times 10^{30}\,\mathrm{erg\,sec^{-1}}$. The higher value is comparable to the energy in the non-thermal fast electrons (computed in Chapter 3).

Origin of the SHC

There are two scenarios suggested by the extremely high density (~$10^{12}\,\mathrm{cm^{-3}}$) of the SHC plasma for the origin of the SHC plasma. (The plasma pressure of ~$10^{4}\,\mathrm{dy\,cm^{-2}}$ corresponds to the magnetic pressure of an ~500 gauss field.) Strong acceleration may occur which produces an intense flux of fast electrons which stop in the chromosphere. The dense plasma may then arise from the chromospheric evaporation process and quench the electron acceleration process, leaving the SHC behind to slowly decay. Alternatively, the high density implies a high electron collisional loss rate which would make acceleration of the electrons extremely difficult. Thus, the SHC may arise from energy release in a filament which is too dense to support significant electron acceleration [*Tsuneta et al.* 1984].

Figure Captions

Figure 4-1 Hard X-ray spectra accumulated over 15 time intervals covering the impulsive and post-impulsive phase of the flare. The time intervals are marked on the 22-33 keV scintillator counting rate inset. The solid lines are model fits to the data. At high energy the model is a single power-law. After 1616 UT the curved thermal spectrum of the Super-Hot Component plasma is included at low energy.

Figure 4-2 Example of the isothermal fit. The power-law fit at high energies and the emission from the flare plasma at low energies ar also shown. The χ^2_ν 90% confidence contour is shown in the upper right corner.

Figure 4-3 Evolution of the SHC emission measure and temperature through the flare. Also shown are the soft X-ray plasma emission measure and temperature.

Figure 4-4 Counting rates in (a) the 8-11.5 keV channel of HXIS and (b) the 11.5-16 keV channel (G. Simnett private communication).

Figure 4-5 Structure of a static loop. The curves are normalized by their maximum value within the loop. For $L=4\times 10^9$cm and $T_{\max}=30\times 10^{6\circ}$K, $F_{c_{\max}}=3.4\times 10^{10}$ergs cm^{-2} sec^{-1}.

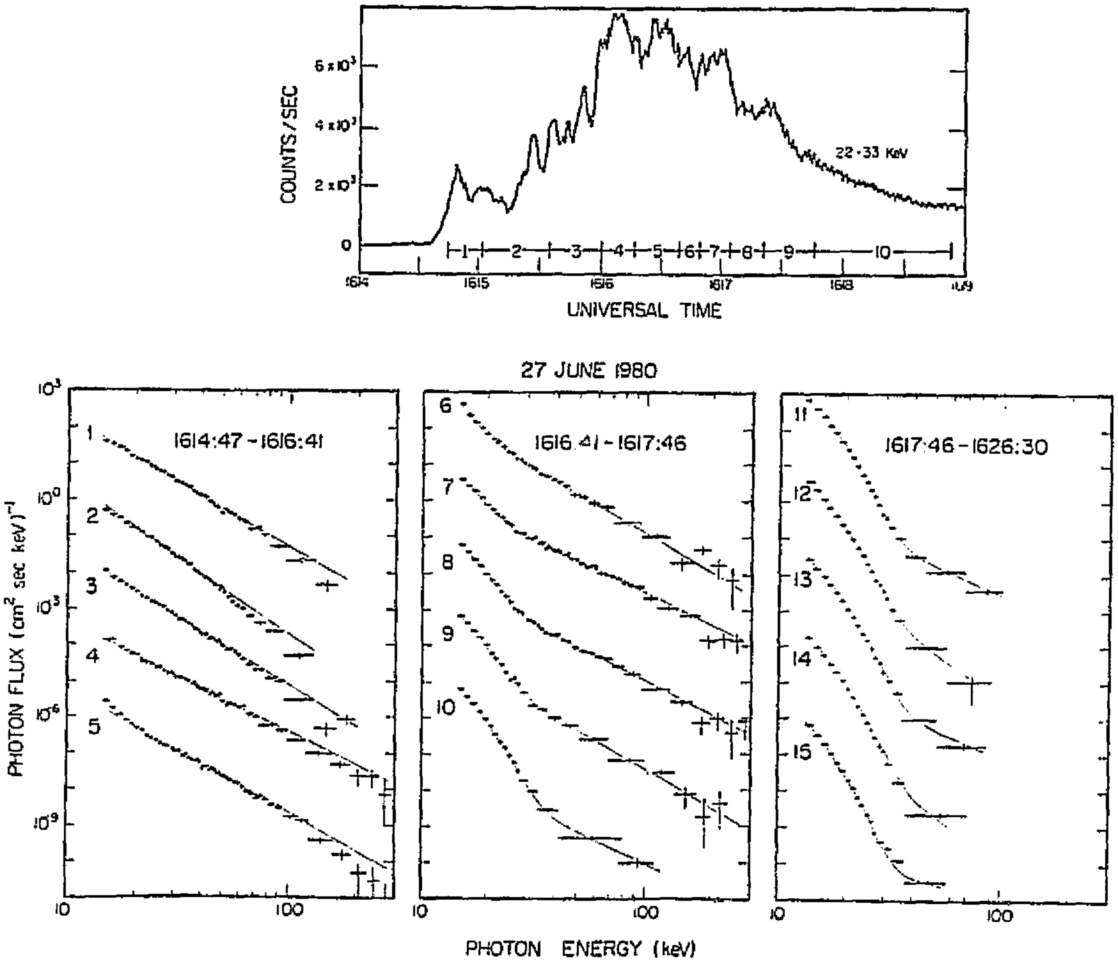
COUNTS/SEC
6×10³
4×10³
2×10³
0
22-33 KeV
1 2 3 4 5 6 7 8 9 10
1614
1615
1616
1617
1618
1619
UNIVERSAL TIME
27 JUNE 1980
PHOTON FLUX (cm² sec keV)⁻¹
10³
10⁰
10⁻³
10⁻⁶
10⁻⁹
1614:47 - 1616:41
1616:41 - 1617:46
1617:46 - 1626:30
1
2
3
4
5
6
7
8
9
10
11
12
13
14
15
10
100
PHOTON ENERGY (keV)

Figure 4-1

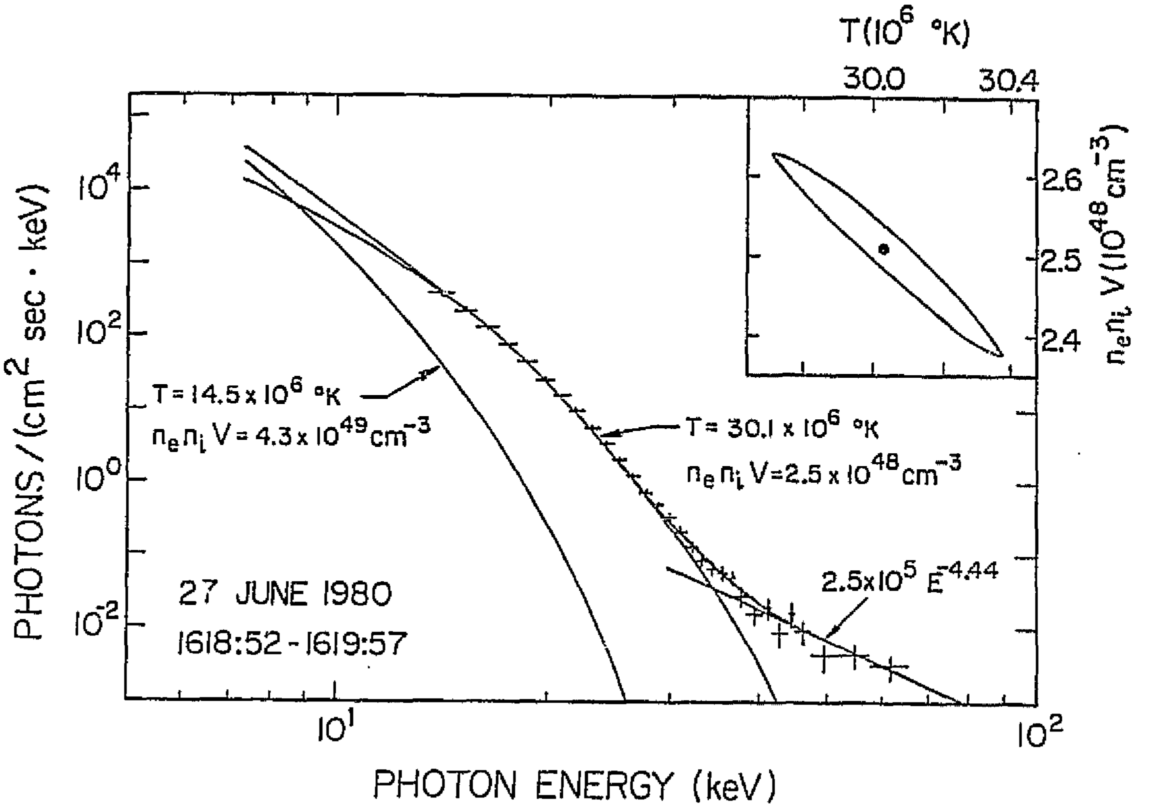
T(10⁶ °K)
30.0
30.4
2.6
2.5
2.4
$n_e n_i V (10^{48} cm^{-3})$
10^4
10^2
10^0
10^{-2}
PHOTONS / (cm² sec · keV)
$T = 14.5 \times 10^6$ °K
$n_e n_i V = 4.3 \times 10^{49} cm^{-3}$
$T = 30.1 \times 10^6$ °K
$n_e n_i V = 2.5 \times 10^{48} cm^{-3}$
$2.5 \times 10^5 E^{-4.44}$
27 JUNE 1980
1618:52 - 1619:57
10^1
10^2
PHOTON ENERGY (keV)

Figure 4-2

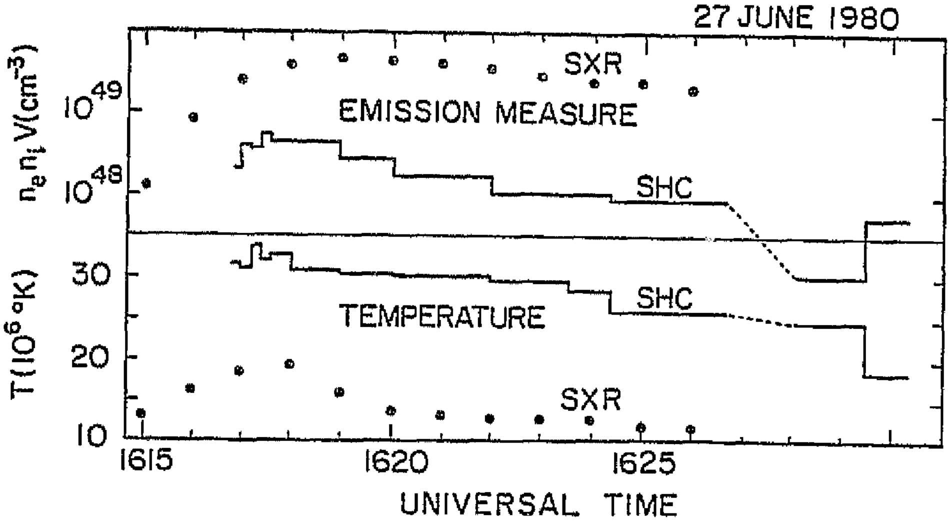
27 JUNE 1980
$n_e n_i V (cm^{-3})$
10^{49}
10^{48}
SXR
EMISSION MEASURE
SHC
$T (10^6 \, °K)$
30
20
10
SHC
TEMPERATURE
SXR
1615
1620
1625
UNIVERSAL TIME

Figure 4-3

HXIS Data 27 June 1980

1631:27 UT Accumulation Time 23.5 s
Coarse FOV 32" × 32" FWHM/pixel

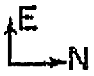

Band 3			0	0	0	0	0	0	0	0		
8.5-11 keV			0	0	0	0	0	0	0	0		
	0	0	0	0	0	0	0	0	0	0	0	0
	0	0	0	0	0	0	0	0	0	0	0	0
	0	0	0	0	0	0	0	0	0	0	0	0
	0	0	0	0	0	0	0	0	0	0	0	1
(a)	0	0	0	0	0	0	0	0	1	0	0	1
	0	0	0	0	0	0	1	48	41	4	0	0
	0	0	0	0	0	0	0	7	9	3	3	1
	0	0	0	0	0	0	0	0	1	3	5	0
			0	0	0	0	0	0	0	1		
			1	0	0	0	0	0	0	0		
Band 4			0	0	0	0	0	0	0	0		
11-16 keV			0	0	0	1	0	0	0	0		
	0	0	0	0	0	0	0	0	0	0	0	0
	0	0	0	0	0	0	0	0	0	0	0	0
	0	0	0	0	0	0	0	0	0	0	0	0
	0	0	0	0	0	0	0	0	0	0	0	0
(b)	0	0	0	0	0	0	0	1	0	1	0	0
	0	0	0	0	0	0	0	13	13	1	2	0
	0	0	0	0	0	0	0	2	6	3	1	0
	0	0	0	0	0	0	0	0	0	0	1	0
			0	0	0	0	0	0	0	0		
			0	0	0	0	0	0	0	1		

Figure 4-4

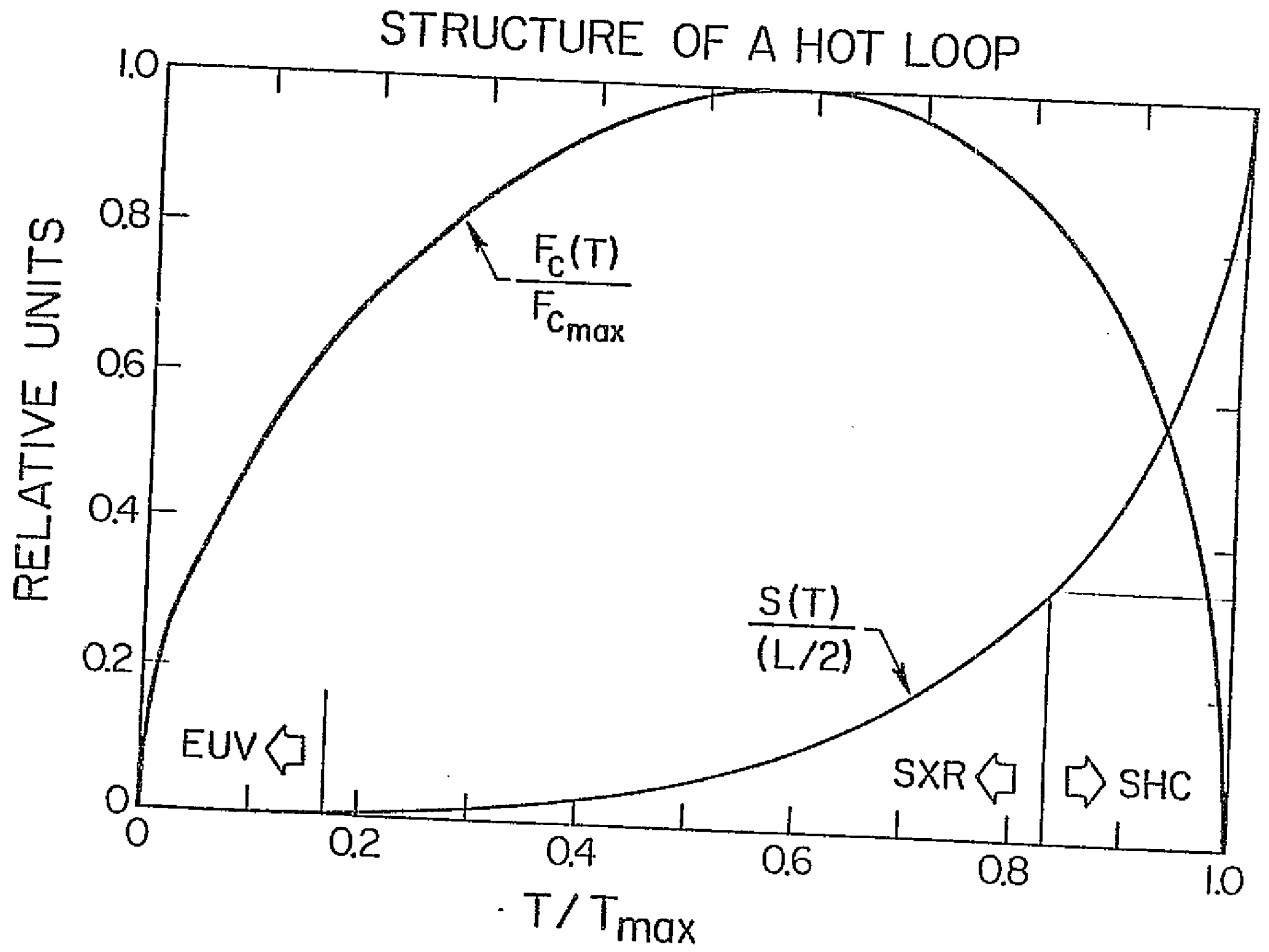
STRUCTURE OF A HOT LOOP
RELATIVE UNITS
1.0
0.8
0.6
0.4
0.2
0
0
0.2
0.4
0.6
0.8
1.0
T / Tmax
Fc(T) / Fcmax
S(T) / (L/2)
EUV
SXR
SHC

Figure 4-5

FIVE

Summary of Flare Results

Here we summarize the non-thermal and thermal results of the flare discussed in chapters 3 and 4. The unifying concept of these results is that electrons are accelerated in the corona and stream down to the denser chromosphere where they deposit a large portion of their energy [*Kane and Anderson* 1970, *Lin* 1974, *Lin and Hudson* 1976, *Brown* 1971 and 1973, *Kane et al.* 1980]. In fact, the first hard X-ray imaging detector, on board the Solar Maximum Mission spacecraft, has observed simultaneous hard X-ray brightenings at widely separated locations which spatially coincide with the bright Hα patches [*Duijveman et al.* 1982]. This observation greatly supports the concept that it is these fast electrons which are the initial carrier of a large fraction of the impulsive flare energy.

During the June 27, 1980 flare, $\sim 10^{38}$ electrons are rapidly accelerated to energies from ~ 15 to greater than 100 keV. Over the whole flare, $\sim 5 \times 10^{30}$ergs may be carried by these electrons. We also know that thermal plasmas are created in this flare with densities as high as $\sim 10^{12}\ \mathrm{cm}^{-3}$ and temperatures in up to 35×10^{6}°K. In addition to the soft and hard X-radiation, there is a wide range of accompanying electromagnetic and particle emissions during the flare.

The flare converts energy stored in the coronal magnetic field into electron energy [*see Svestka* 1976, *Van Hoven et al. Kahler et al.* 1980]. For a volume of $10^{27}-10^{28}\ \mathrm{cm}^3$ we require

PRECEDING PAGE BLANK NOT FILMED

that $B^2V/(8\pi) > 5 \times 10^{30}$ergs or $B > 100$-350 gauss. The first indication of the energy conversion process is the rise in soft X-rays at 1612 UT. This is followed by the first observation of the hard X-rays at 1613:30 UT. The soft X-ray flux may be produced by the heating from the linear stage of a current dissipation process, which is followed by the far more dynamic non-linear stage. During this non-linear stage, the conditions may exist for particle acceleration [*Alfvén and Carlqvist* 1967, *Kane and Anderson* 1970, *Carlqvist* 1972, *Spicer* 1977a and b].

The hard X-ray time profiles and spectra reveal several important characteristics of the energy conversion process. The rate of energy input into energetic electrons, computed in the thick target picture, remains nearly constant across any individual burst, and also changes very slowly from burst to burst. This temporal behavior is the same as shown by the *gradual* component of the impulsive phase non-thermal X-rays and is very different from the rapid variations seen in the ~35-100 keV hard X-rays. It may be that the energy release is slowly varying because the process depends on the global properties of the flare region. These global properties may evolve on a timescale given by the propagation of Alfvén waves across the flare site.

The spectral evolution of an individual burst reveals information about the acceleration process. This process appears to accelerate electrons to ≥ 100 keV within a fraction of a second. One possible way to achieve this rapid electron acceleration is by an electric field. Potential drops are known to exist along magnetic field lines in the Earth's magnetosphere [*Mozer et al.* 1980]. Conditions which maintain a large drop might also occur in the turbulent conditions of the flare plasma [*Gold and Hoyle* 1966, *Alfvén and Carlqvist* 1967, *Spicer* 1977a and b, *Colgate* 1978]. The number of higher energy (60-100 keV) electrons should depend strongly on the total potential drop along the field lines. Thus, the spectral hardening of a burst may reflect the growth of the total potential drop along the field lines. However, *De Feiter* [1972] and *Anderson and Mahoney* [1974] show that if the coronal magnetic field is rapidly dissipated, then there would be an inductive potential drop orders of magnitude higher than the 100-1000 kV one might infer from the fast electron population.

In any event, there are non-thermal electrons streaming along the field lines. Some of the fast electons may escape along open field lines to produce Type III radio bursts [*Lin* 1974]. Higher energy electrons will produce the intense 10.6 GHZ microwaves seen during this flare [*Takakura and Kai* 1966, *Ramaty* 1969, *Ramaty and Petrosian* 1972]. Some of the 10-100 keV electrons are stopped within the corona where their kinetic energy is turned into heat to produce the soft X-ray flare plasma [*Canfield et al.* 1980]. Some of the electrons strike the chromosphere where they produce impulsive radiation in H_α [*Canfield et al.* 1980] and the EUV [*Donnelly and Kane* 1978] from the collisional excitation of the protons and ions. After the flare plasma is heated, however, additional EUV and H_α appear as gradual emissions with a time profile similar to that of the soft X-rays [*Moore et al.* 1980].

The succession of discrete bursts indicates a small-scale structure to the flare in addition to the aforementioned global structure as in Figure 5-1. The flare structure may consist of a large loop or arch containing bundles of individual filamentary flux tubes similar to the individual wires within a cable. Much of the actual energy release may occur within a small subset of these filaments. This would imply energy fluxes from the non-thermal electrons of much greater than 10^{10} ergs $cm^{-2}\ s^{-1}$. Such an intense and penetrating energy flux would blow off the upper layer of the chromosphere [*Brown* 1973, *Lin and Hudson* 1976]. This explosion will drive some mass up the field lines and send shock waves outward through the solar atmosphere [*Fisher et al.* 1984]. These shock waves may provide the moving mirrors for the delayed second-step acceleration of electrons to several hundred keV energies [*Bai and Ramaty* 1979]. These shock waves could also accelerate the energetic protons to >30 MeV in a first-order Fermi process. Some of these protons escape along open field lines into interplanetary space. These shock waves are observed producing the Type II radio burst [*Wild et al.* 1954, *Wild et al.* 1963] seen at 1620 UT in the upper corona.

This filamentary model means that some flux tubes have a higher rate of energy release than others. Also, some of these filaments are characterized by peak temperatures typical of

C - 2

the soft X-ray flare plasma $(<20 \times 10^{6}\,^{\circ}K)$ and and other filaments contain the much hotter super-hot component plasma. The maximum temperature within a loop is governed by the steady-state balance between the loop losses and inputs. If the heat input, either by non-thermal electrons, or by some direct heating mechanism, is high enough and is sustained over a long enough time, then the super-hot component plasma will appear.

The late phase impulsive hard X-ray spikes are clear evidence of electron acceleration after the main impulsive phase ends at ~1617:30 UT. These non-thermal electrons might provide the power which maintains temperature of the super-hot component plasma from 1618 through 1622 UT. However, the super-hot component plasma does not appear to change during the larger late phase bursts at 1624 and 1630 UT. Also, the high density of the super-hot component may preclude acceleration in these filaments.

Despite the advances in our understanding which has come from the intense effort of the solar physics community during the latest solar maximum, the basic underlying problems of the flare process remain unresolved. How is so much magnetic field energy so rapidly converted into non-thermal kinetic energy? Are the electrons accelerated within a small region or all along the field lines? What triggers the energy release and what quenches it? How can such intense electron beams propagate through the corona? Is the rapid second-step acceleration of protons and electrons really a process distinct from the initial particle acceleration? These are only a few of the questions which need to be answered before one can say that a true understanding of solar flares exists.

Figure Captions

Figure 5-1 Schematic model of the flare region showing electrons streaming into the chromosphere, the reflection of electrons off of the flare explosion shock wave, the hard X-ray production region, the super-hot component filaments, and the soft X-ray plasma. The left hand side shows the impulsive phase phenomena and the right shows the thermal phenomena, but the actual loop will be nearly symmetric around the apex.

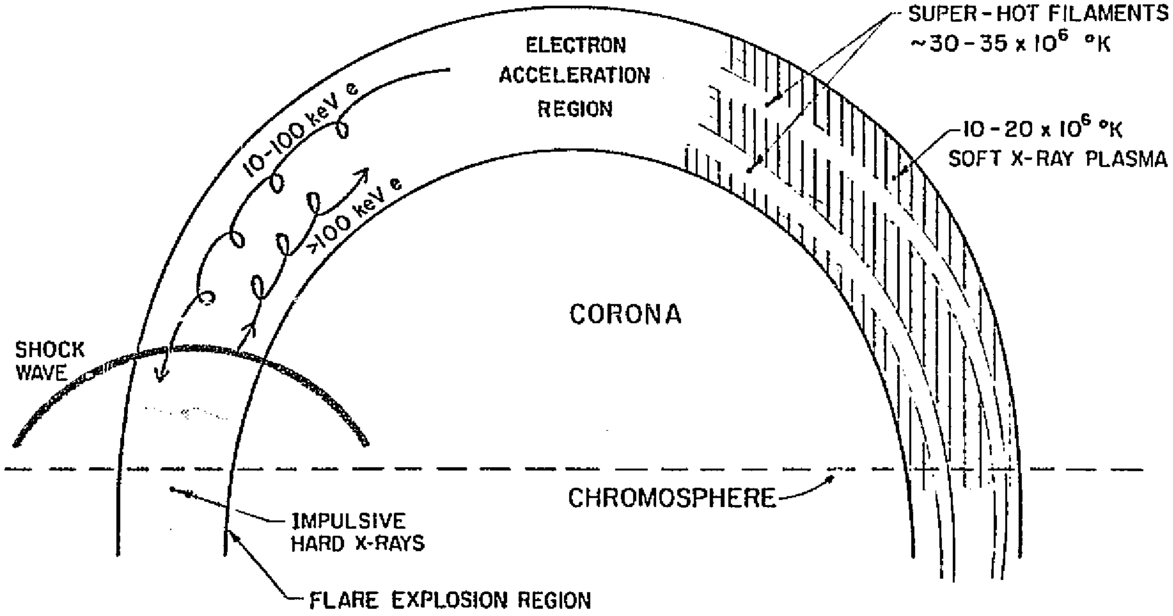
ELECTRON
ACCELERATION
REGION
10-100 keV e
>100 keV e
SUPER-HOT FILAMENTS
~30-35 x 10^6 °K
10-20 x 10^6 °K
SOFT X-RAY PLASMA
CORONA
SHOCK
WAVE
CHROMOSPHERE
IMPULSIVE
HARD X-RAYS
FLARE EXPLOSION REGION

Figure 5-1

SIX

Search for the 73 keV Line from the Crab Nebula

6-A. Introduction

The Crab Nebula has remained one of the most interesting and observed objects in astronomy. It was the first cosmic X-ray source to be identified with either a visible or a radio object [*Bowyer et al.* 1964]. It is the most intense hard X-ray source (15-200 keV) and has been repeatedly observed using many different instruments carried on balloons, rockets, and satellites [*Toor and Seward* 1974, *Dolan et al.* 1977, *Knight* 1981]. While most of the observations showed a very constant emission over this energy range there have been several observations which appear to exhibit extremely interesting transient phenomena.

The Crab Nebula is the product of a supernova explosion about 2 kiloparsecs away seen on the Earth in 1054. The X-ray emitting region is about 2' across with a central object pulsing every 33 msec identified as the radio pulsar NP 0531, which also pulses in visible light, soft X-rays, and gamma-rays. The ultimate power source for both the nebular and pulsar emission is thought to be from the rotational energy of the central neutron star. Most of the hard X-ray emission is unpulsed and thought to be of nebular origin from the synchrotron emission of energetic electrons moving along open field lines from the pulsar. Since the size of this emitting region is about 2 light years across, any variations on a short time scale probably originate within a volume near the pulsar.

Previous Hard X-ray Observations

The majority of previous observations are consistent with the view of the Crab as the standard candle of hard X-ray astronomy. *Toor and Seward* [1974] reviewed all of the previous X-ray observations and concluded that any observed variations in the Crab X-ray spectrum could be interpreted as due to systematic difficulties with those experiments. In fact, the three most current and most sensitive satellite observations of the Crab by OSO-8 [*Dolan et al.* 1977], HEAO-1 [*Pravdo and Serlimitsos* 1981, *Knight* 1982, *Gruber et al.* 1980], and [*Mahoney et al.* 1984], have not shown any temporal variation in this hard X-ray flux.

First Observation of Hard X-ray Line Emission

Ling et al. [1979] made an observation of the Crab on June 10, 1974 using an array of 3 moderately high resolution (2.2 keV FWHM) detectors. They reported a possible line feature at 73.3 kev with an intensity of $3.8 \pm .9 \times 10^{-3}$ ph cm^{-2} sec^{-1} in the total pulsed and unpulsed Crab spectrum. They estimate that no more than 25% (1σ) of the line flux could be pulsed [*Mahoney et al.* 1984].

During a balloon flight on June 21, 1974 a transient feature was observed in the pulsar light curve in an observation using a large area scintillation detector [*Ryckman et al.* 1977]. In an observation using a heavily shielded GeLi detector, *Leventhal et al.* [1977] reported a possible gamma-ray line at 400 keV with an intensity of $2.24 \pm .65 \times 10^{-3}$ and a FWHM $\leqslant$ 3keV. These features have not been reported in any other observations of the Crab.

There were subsequent balloon observations which tried to confirm the 73 keV line observation. A line at this intensity, at this energy, and of possibly narrow width makes a very attractive target for a high resolution hard X-ray spectrometer. Therefore, we looked at the Crab during two balloon flights on October 18, 1979 and June 27, 1980 with a combined observation time of approximately 25,000 seconds. The spectra from these observations do not show any line emission at 73 keV in either the total spectrum or in the pulsed component. We discuss these observations in more detail later. Using a high resolution detector similar to ours, with a 1.4 keV FWHM resolution, *Hameury et al.* [1983] set a 3σ upper limit of 6×10^{-4} ph cm^{-2} sec^{-1} to a narrow line at 73 keV during a September 25, 1980 balloon flight. Finally, the line was reported to have been observed in two separate balloon observations.

First, a balloon flight from Sicily [*Manchanda et al.* 1982] using a 900 cm^2 high presure Xenon proportional counter observed the Crab for thirty minutes on August 26, 1979. In the Crab spectrum they report a line near 73 keV with a flux of $5\pm1.5\times10^{-3}$ ph cm^{-2} sec^{-1} and an unresolved line width. Their data suggests that the line was pulsed at the pulsar frequency, although a timing problem makes that inconclusive. *Strickman et al.* [1979] observed the Crab on balloon flight from Palestine, Texas on May 11, 1976 using a 765 cm^2 scintillator. The spectrum, time averaged over their whole observation, was consistent with no line emission near 73 kev. However, after analyzing their data over a shorter time scale, they found evidence of a "flare" in the pulsed hard X-ray spectrum. During the 25 minutes of this "flare" they measured a pulse phase averaged (Pulse phase averaged means that the counts in the line are divided by the time of the pulse phase which is ~ .63 of the time on the Crab.) line flux of $4.1\pm1.2\times10^{-3}$ ph cm^{-2} sec^{-1} at 76.6 ± 2.5 keV with an 8 ± 18 keV FWHM [*Strickman et al.* 1982]. Note that both observations are consistent with 73 keV line emission which I believe lends considerable confidence to all three reported positive observations.

6-B. Statistical Validity of the June 10, 1974 Observation

The confidence level of a reported emission line at some previously unreported energy must correctly take into account the total number of independent statistical trial events represented by a given data set [*Cherry et al.* 1980, *Dolan* 1982]. The confidence level, C, of a particular line observation is the probability that the excess is not due to a random fluctuation in the data set. For M independent trials of the same measurement the probability that no single trial would have an excess so large $C' = C^M$. So, for a hard X-ray or a gamma-ray line observation, it is the many PHA channels which comprise the set of independent trials. Also, breaking the data set into time bins multiplies the number of independent trials. For example, for the June 10, 1974 observation of line emission at 73.3 keV [*Ling et al.* 1979], *Cherry et al.* [1980] have suggested that M should be 8192, the number of detector PHA channels. The reported line strength of 3.8×10^{-3} ph cm^{-2} sec^{-1} with a one σ deviation of $.9 \times 10^{-3}$ is an unnormalized 4.2 σ's greater than a null result. This corresponds to a confidence level $C = .999867$ which gives a $1-C = 1.33 \times 10^{-5}$ probability that the excess is just due to chance fluctuation. However if the confidence level is adjusted by choosing M=8192 we find that $1-C' = .1$ which would be weak evidence for a line.

However, choosing M=8192 is not valid for several reasons. First the energy resolution of the detector used was at best 2.2 keV FWHM which means at least 2 PHA channels per resolution element. Secondly, the reported feature is at less than 100 keV and is in the spectrum of a source which includes a neutron star, suggesting that the line may be due to quantized cyclotron radiation [*Ling et al.* 1979] as presumed in the case of the confirmed line emission from Her-X1 [*Trümper et al.* 1978], at ~58 keV. Although the Crab pulsar and nebula are powered by the rotational energy of the neutron star and not by the gravitational energy of material falling from a companion star, the presence of a strong magnetic field, 10^{12}–10^{13} gauss, is a necessary condition for hard X-ray cyclotron emission. In the simplest picture of cyclotron radiation

$$h\nu = 73 \text{ keV} = \hbar \frac{eB}{m_e c}$$

which yields a B of about 6.3×10^{12} gausss. Field values are not likely to be more than a few 10^{13} gauss, so cyclotron lines should be found at energies below about 200 keV. Also the highest field values should be close to the surface of the neutron star so the expected gravitational redshift of about 20% would further reduce the upper limit for cyclotron emission. One might also expect that the line to continuum flux ratio should be of the same order as for Her-X1. This restricts the energy range over which the hard X-ray detector has sufficient sensitivity to the lower energies since the continuum flux is falling. Taking these restrictions into account, along with the low energy cutoff of 50 keV for the spectrometer used, a value of M=70 seems more appropriate. Using this value of M, we find that $1-C' = 9.3 \times 10^{-4}$ or that there is less than one chance in a thousand that the excess flux was just due to a random fluctuation in the counting rate.

There is one additional piece of evidence which supports the observation by *Ling et al.* [1979]. The count rate excess due to the line is modulated by the aperture response of the detector's collimator in the same way the continuum flux is modulated. If the line is not of cosmic origin then this apparent modulation is another remarkable statistical fluctuation. Thus, this increases the statistical significance of their observation

6-C. Results

Crab Spectra and Search for Line Emission

We have concentrated the analysis of our observations of the Crab to search for evidence of narrow line emission at 73.3 keV in the total time averaged spectrum of each flight, the pulsed minus unpulsed spectrum, and over individual source observation segments. We have also searched our data for evidence of other line features in the 15-200 keV range. The unpulsed spectrum was also examined to determine whether a single power-law could be an acceptable fit or whether a break is needed in the spectrum [*Strickman et al.* 1979].

Our first observation was made during a balloon flight from Palestine, Texas on October 17-18, 1979. From 07:00:00 to 12:30:00 hours UT both the germanium spectrometer and the

300 cm^2 scintillation detector were pointed on and off the Crab for successive twenty minute periods. Each background interval consisted of two ten minute pointings to locations which were above and below the Crab in elevation angle.

The second flight was made on June 27, 1980 during which both the Crab and the Sun were alternately observed from 15:30:00 to 21:00:00 UT. The Crab pointings occurred from 16:40:00 U.T. until 19:30:00 U.T.; background pointings were interspersed about one-third of the time.

Pulse Phase Binning

This phase binning was done in the same manner for each flight. To separate the pulsed component of the Crab spectrum from the unpulsed component, we divided the Crab pointing data into 64 pulse phase bins. The events from the larger area scintillation detector were used to determine the pulsar timing parameters by constructing a pulsar light curve. The scintillator data was first binned by phase using trial values for the pulsar period and its first time derivative, and by correcting for the motion of the balloon relative to the Crab, where the Earth's motion around the solar system barycenter is the principal component. This binning yielded a light curve and the deviations from a constant rate were used to compute a value of the Chi-square statistic. The timing parameters were varied to maximize Chi-square to obtain the final light curves in Figure 6-1 which agree very well with other observations.

Data Reduction

We analyzed the spectra for each flight separately, but using nearly the same procedure. To determine the total flux from the Crab, we subtracted the background rate from the on-source rate, then deconvolved the spectrum for the instrumental response and normalized the result for attenuation and transmission (see the discussion on spectral deconvolution in Chapter 2). However, we constructed the background rate differently for each flight.

Examining the spectrometer counting rates over the 1979 flight we saw a gradual rise in the background rate with time. The predominant cause is the northward drift of the balloon in geomagnetic latitude during the flight; the background rate is known to increase by about 1% for every degree of northward latitude *Ling et al.* [1979]. Therefore, to minimize this effect, the background for each on-source interval was constructed from a time average of the adjacent background intervals. For the 1980 flight, the overall background rate was much lower (the 15 to 100 keV continuum was lower by ~50%) due to improvements in the cryostat design. Also, the flight trajectory was due west so that there was no large background variation. We have also included, as background for the Crab, times when we are pointing on the Sun and there is no solar activity above the smaller 'microflares' [*Lin et al.* 1984]. (These microflares are too small to affect the flux around 73 keV.) Using this larger background sample improves our sensitivity to line emission. We averaged these non-Crab rates together to determine a single background rate which was subtracted from each on-source rate. Then, the each difference spectrum is converted to a photon spectrum at the top of the atmosphere using the line-of-sight atmospheric depth, collimator transmission, and detector response function. Finally, to determine the total time averaged spectrum, each of the individual photon spectra is combined in a weighted average to obtain the total Crab flux.

Each on source time interval is an independent observation of the Crab spectrum. To find the best average spectrum [*Bevington* 1969] (based on the Maximum Likelihood principle) the weighting factors for each energy bin should be the inverse of the square of the standard deviation of the flux. Essentially, the weights were constructed from the product of the time on the source and the square of the transmission through the aperture and overlying atmosphere. These are the most important factors which do not change between the independent on source intervals.

The pulsed spectrum is obtained by subtracting the off-pulse rate from the on-pulse rate for each on-source interval. The pulsed region is defined here to be from 135 to 360 phase in the pulsar light curve in Figure 6-1. Then, the deconvolution procedure is applied to each pulsar count rate. These are combined in a weighted average to form the pulsar spectrum (in ph cm^{-2} keV^{-1} sec^{-1}) averaged over the on-pulse phase. This spectrum is normalized by multiplying by (360-135)/360 to obtain a pulsar spectrum averaged over the total pulsar phase. Then one defines the Crab nebular spectrum as the remaining unpulsed component; this is obtained by subtracting the total averaged pulsar spectrum from the total Crab flux bin by bin.

Spectral Fits

Parametric fits were made to the total Crab spectrum, the nebular spectrum, and the pulsar spectrum using the non-linear routines discussed by *Bevington* [1969]. Table 6-1 lists the best fits to the total Crab spectrum for both flights for a single power-law and for single and double power-law models for the nebular emission for the June 27, 1980 flight. Figure 6-2 shows the total Crab spectrum for June 27, 1980. The single power-law gives an acceptable value of χ^2_ν for the total Crab spectrum for both flights. The spectral index of ~2 verifies that we are able to successfully deconvolve the counting rate into a photon spectrum. Also, the flux at 70 keV for both flights is within 10% of the value obtained by *Ling et al.* [1979]. *Strickman et al.* [1979] claim that there is a spectral break at 80 keV in the nebular emission with the power-law index increasing by ~ .4. Our best double power-law fit shows a break at 70 keV with break of ~ .4. However, by the statistical criteria of *Lampton et al.* [1976] for a model with four

Table 6-1 Spectral Fits to Crab Data

Best-Fit Spectral Models

Single Power-Law: $\Phi = A\ E^{-\gamma 1}$
Double Power-Law: $\Phi = A\ E^{-\gamma 1}$ *for* $E < E_b$
$= (A\ E_b^{-\gamma 1})\ E^{-\gamma 2}$ *for* $E \geqslant E_b$

	Total Crab		Nebular Emission	
	10/18/79	6/27/80	6/27/80	
	Single Power-Law	Single Power-Law	Single Power-Law	Double Power-Law
Interval	35-150 keV	20-150 keV	20-150 keV	20-150 keV
A	12.7	4.86	4.26	3.54
E_b	NA	NA	NA	64 keV
$\gamma 1$	2.2±.1	2±.05	2±.05	1.95
$\gamma 2$	NA	NA	NA	2.32
χ^2_ν	χ^2_{11}=1.36	χ^2_{14}=1.11	χ^2_{14}=1.13	χ^2_{12}=1.11

free parameters, we find that the break energy could range from ~ 30-100 keV. Also, the reduction in χ^2 from the single power-law value is not large enough (by the F-test in *Bevington* [1969]) to mandate the additional two parameters of the double power-law. Thus, we find that our observation is consistent with that of *Strickman et al.* [1979], but that we cannot constrain their observation of a break. However, we can set observational limits to line emission which are below the observed line fluxes.

We visually examined the high resolution spectra for the total Crab and for the pulsar to look for a narrow line (~ 1 keV FWHM) from 71 to 75 keV. We fit the largest excesses above the Crab continuum spectrum with a gaussian profile but did not find any statistically significant flux. Thus, we list in Table 6-2 the three σ upper limits for these four spectra. We also looked unsuccessfully for evidence of the sort of line 'flare' seen by *Strickman et al.* [1982].

We have searched the data of both flights for evidence of other narrow line features. We have adopted the criteria of a line at 3σ during a single flight with an excess shown in each detector or a 2σ feature showing in both flights at the same energy. The search was done by visual inspection of the spectra for possible candidates and then by attempting to fit lines to any candidate lines. No narrow features were found that met these criteria.

6-D. The Sun as a Possible Source of the 73 keV Line

During the June 10, 1974 observation of the Crab the Sun was located very close to the Crab. Because of the wide field of view of about 30 degrees FWHM of the detector aperture [*Ling et al.* 1979], the Sun could not be excluded as a possible source of the line emission even

Table 6-2 Limits to Line Emission from the Crab

	Three σ Upper Limit to Narrow Line Emission (71 - 75 keV)	
	Total Crab	Pulsar
Oct. 18, 1979	1.9×10^{-3} ph cm^{-2} keV^{-1} sec^{-1}	2.7×10^{-3} ph cm^{-2} keV^{-1} sec^{-1}
June 27, 1980	1.4×10^{-3} ph cm^{-2} keV^{-1} sec^{-1}	1.8×10^{-3} ph cm^{-2} keV^{-1} sec^{-1}

Pulsar limit is for flux averaged over the pulse phase region.

though there is no record of any solar activity during the observation. Our 1980 flight observed the Crab and the Sun independently. The narrow field of view of our telescope precluded any confusion of the Crab with the Sun. We obtained a three σ upper limit to a solar line at 73 keV of 1.5×10^{-3} ph cm^{-2} sec^{-1} which is well below the reported Crab flux.

6-E. Discussion

The Crab seems to be a source of a transient emission line near 73 keV. Although our observation clearly shows that there was no flux at an intensity well below the reported level, the evidence of *Ling et al.* [1979], *Manchanda et al.* [1982], and *Strickman et al.* [1982] is strong. These three independent positive reports of an emission feature are extremely difficult to ignore by attributing the line to some systematic error. The total Crab spectrum measured during these observations agreed very well with all the other continuum measurements. None of these detectors have a background feature near 73 keV and *Strickman et al.* [1982] reported that the line emission was pulsed and in phase with the continuum pulsed emission. Also, if the effect were systematic, one would expect to have reports of line emission near 73 keV from other sources. Unfortunately, the three observations made with the best energy resolution (the two reported here and *Hameury et al.* [1983]) did not observe the feature. The transient nature of this line means that the source cannot be a radioisotopic decay with a decay time greater that ~10 minutes. It is more likely that the emission is more directly associated with the pulsar magnetosphere although *Strickman et al.* [1982] showed that the pulsar hard X-ray continuum remained unchanged during the line 'flare'. Clearly the measurement of the true width of this feature will give great insight to the possible phsical emission mechanism. For example, if the emission is of cyclotron origin then constraints could be placed on dB/B and the velocity distribution along the line of sight. The Crab remains as a primary target for continued observation by a high energy resolution instrument.

Figure Captions

Figure 6-1 Pulsar light curves from balloon flights of October, 1979 and June 1980 obtained from the scintillator data. The pulse phase region consists of two peaks and an interpeak region from 135 to 360 degrees. The off-pulse region extends from 0 to 135 degrees.

Figure 6-2 Total Crab spectrum for June 27, 1980.

ORIGINAL PAGE IS
OF POOR QUALITY

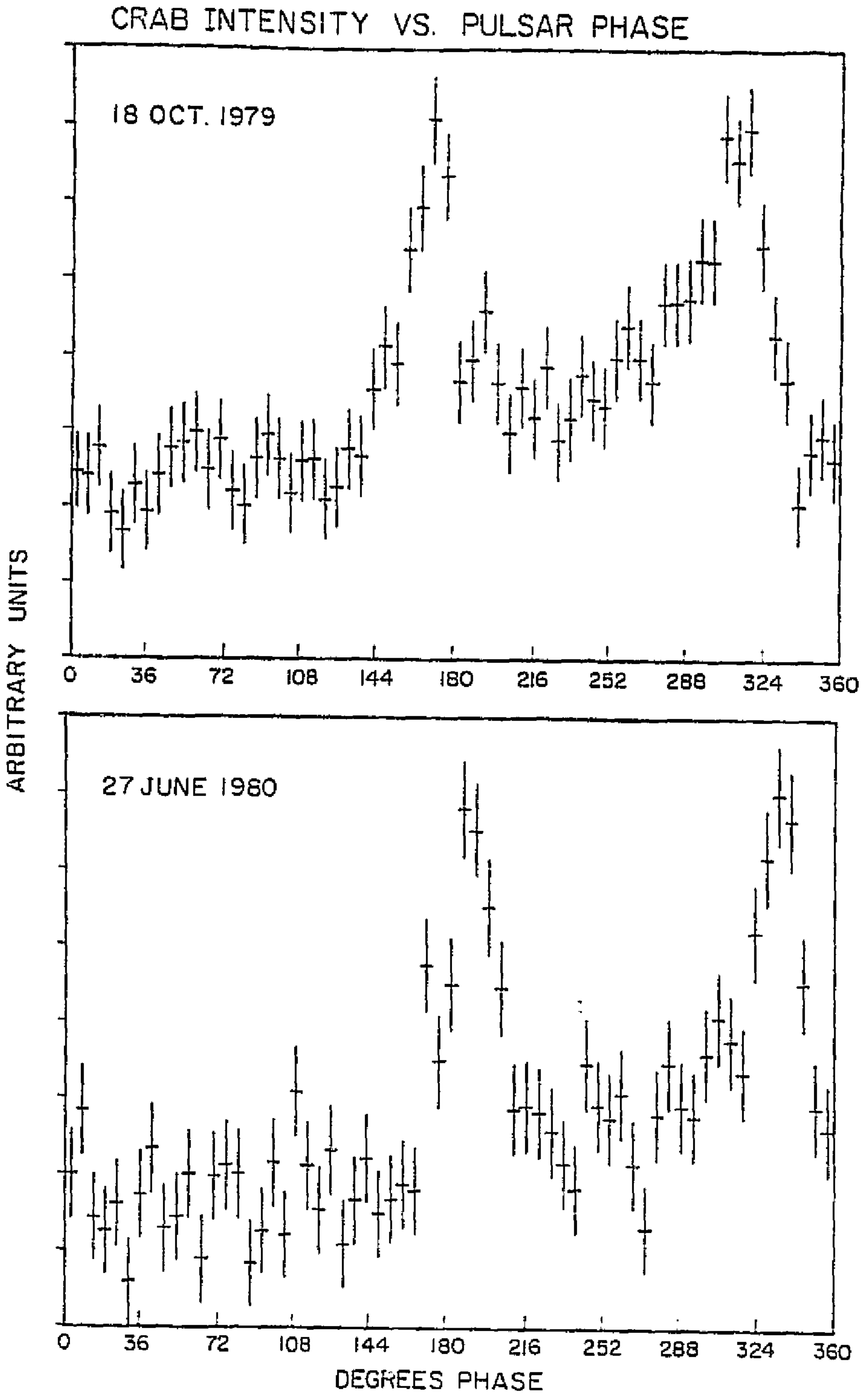

Figure 6-1

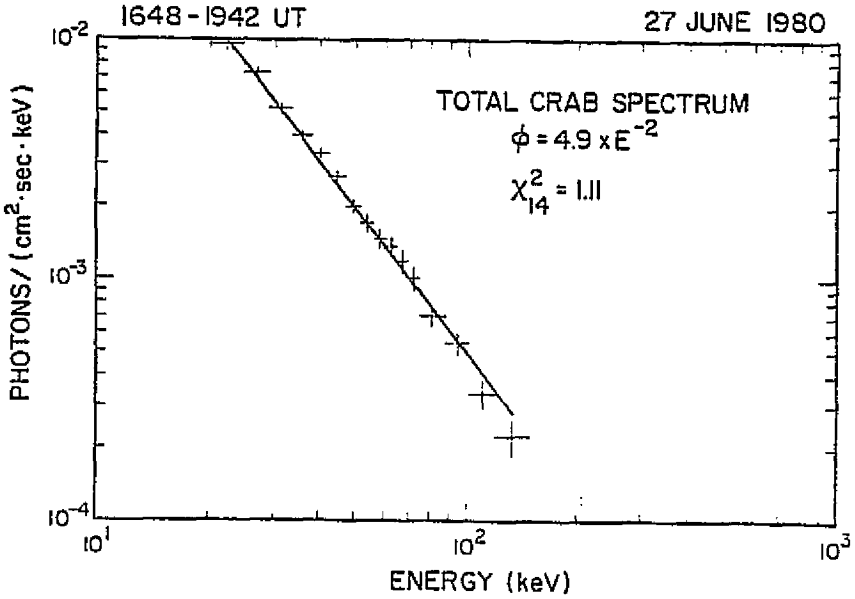
1648 - 1942 UT
27 JUNE 1980
TOTAL CRAB SPECTRUM
$\phi = 4.9 \times E^{-2}$
$\chi^2_{14} = 1.11$
PHOTONS/(cm^2·sec·keV)
10^{-2}
10^{-3}
10^{-4}
10^{1}
10^{2}
10^{3}
ENERGY (keV)

Figure 6-2

ORIGINAL PAGE IS
OF POOR QUALITY

References

Alfvén, H. and Carlqvist, P 1967, *Solar Phys.*, 1, 220.

Anderson, K. A. 1972, *Solar Phys.*, 27, 442.

Anderson, K. A. and Mahoney, W. A. 1974, *Solar Phys.*, 35, 419.

Bai, T., 1982, *Gamma Ray Transients and Related Astrophysical Phenomena*, ed. R. E. Lingenfelter (New York: American Inst. of Physics), p. 409.

Bai, T., and Ramaty, R. 1976, *Solar Phys.*, 49, 343.

Bai, T., and Ramaty, R. 1979, *Astrophys. J.*, 227, 1072.

Bai, T. and Dennis, B. R. 1983, *SUIPR Report No. 961*.

Bai, T., Hudson, H. S., Pelling, R. M., Lin, R. P., Schwartz, R. A., and von Rosenvinge, T. T. 1983, *Astrophys. J.*, 267, 433.

Bevington, P. R. 1969, *Data Reduction and Error Analysis for the Physical Sciences*, (New York: McGraw-Hill).

Bowyer, C. S., Byram, E. T., Chubb, T. A., and Friedman, H. 1964, *Science*, 146, 912.

Brown, J. C. 1971, *Solar Phys.*, 18, 489.

Brown, J. C. 1973, *Solar Phys.*, 31, 143.

Browne, E., Dairiki, J. M., Doebler, R. E. *et al.* 1978, *Table of the Isotopes* ed. C. Michael Lederer and Virginia S. Shirley, (New York: Wiley-Interscience).

Canfield, R. C. *et al.* 1980, *Solar Flares*, ed. Peter A. Sturrock (Boulder: Colorado Associated University Press), p. 231.

Carlqvist, P. 1972, *Cosmic Electrodynamics*, 3, 377.

Cherry, M. L., Chupp, E. L., Dunphy, P. P., Forrest, D. J., and Ryan, J. M. 1980, *Astrophys. J.*, 242, 1257.

Chupp, E. L. 1982, *Gamma Ray Transients and Related Astrophysical Phenomena*, ed. R. E. Lingenfelter (New York: American Inst. of Physics), p. 363.

Colgate, S. A. 1978, *Astrophys. J.*, 221, 1068.

Crannell, C. J., Frost, K. J., Mätzler, C., Ohki, K., and Saba, J. L. 1978, *Astrophys. J.*, 223, 620.

De Feiter, L. 1972, *Space Sci. Rev.*, 13, 337.

de Jager, C. 1969, *COSPAR Symposium on Solar Flares and Space Science Research*, ed. C. de Jager and Z. Svestka (Amsterdam: North Holland), p. 1.

de Jager, C. and de Jonge, G. 1978, *Solar Phys.*, 58, 127.

Dolan, J. F., Crannell, C. J., Dennis, B. R., Frost, K. J., Maurer, G. S., and Orwig, L. E. 1977, *Astrophys. J.*, 217, 809.

Donnelly, R. F., Grubb, R. N. and Cowley, F. C. 1977, *NOAA Technical Memorandum* (EJRL SEL-48).

Donnelly, R. F. and Kane, S. R. 1978, *Astrophys. J.*, 222, 1043.

Duijveman, A., Hoyng, P., and Machado, M. E. 1982, *Solar Phys.*, 81, 137.

Duijveman, A. 1983, *Solar Phys.*, 84, 189.

Elcan, M. J. 1978, *Astrophys. J. (Letters)*, 226, L99.

Elliot, H. 1969, *COSPAR Symposium on Solar Flares and Space Science Research*, ed. C. de Jager and Z. Svestka (Amsterdam: North Holland), p. 356.

Fenimore, E. E., Laros, J. G., Klebesadel, R. W., and Stockdale, R. E. 1982, *Gamma Ray Transients and Related Astrophysical Phenomena*, ed. R. E. Lingenfelter (New York: American Inst. of Physics), p. 201.

Fisher, G. H., Canfield, R. C., and McClymont, A. N. 1984, submitted to *Astrophys. J.*,

Forrest, D. J., Chupp, E. L., Ryan, J. M., Reppin, C., Rieger, E., Kanbach, G., Pinkau, K., Share, G., and Kinzer, R. 1981, *Proc. 17th Intl. Cosmic Ray Conf.* (Paris), 10, 5.

Gold, T. and Hoyle, F. 1960, *Monthly Notices of the Roy. Astron. Soc.*, 120, 89.

Gosling, J. T., Asbridge, J. R., Bame, S. J., Feldman, W. C., Zwickl, R. D., Paschmann, G., Sckopke, N. and Hynds, R. J. 1981, *J. Geophys. Res.*, 86, 547.

Gruber, D. E., Matteson, J. L., Knight, F. K., Rothschild, R. E., Nolan, P. L., Howe, S., Levine, A. M., and Primini, F. A. 1980, *BAAS*, 12, 541.

Haller, E. E. 1982, *IEEE Trans. Nucl. Sci.*, NS-29, No. 3, 1109.

Hameury, J. M., Boclet, D., Durouchoux, P., Cline, T. L., Paciesas, W. S., Teegarden, B. J., Tueller, J., and Haymes, R. C. 1983, *Astrophys. J.*, 270, 144.

Hudson, H. S., Canfield, R. C., and Kane, S. R. 1978, *Solar Phys.*, 60, 137.

Hurley, K., and Duprat, G. 1977, *Solar Phys.*, 52, 107.

Jacobson, A. S. 1977, *High Resolution Gamma-Ray Spectroscopy*, Invited paper, Am. Phys. Soc., Spring Mtg.

Kahler, S *et al.* 1980, *Solar Flares*, ed. Peter A. Sturrock (Boulder: Colorado Associated University Press), p. 83.

Kane, S. R. and Anderson, K. A. 1970, *Astrophys. J.*, 162, 1003.

Kane, S. R. and Hudson, H. S. 1970, *Solar Phys.*, 14, 414.

Kane, S. R. *et al.* 1980, *Solar Flares*, ed. Peter A. Sturrock (Boulder: Colorado Associated University Press), p. 187.

Kane, S. R., Kai, K., Kosugi, T., Enome, S., Landecker, P. B., and McKenzie, D. L. 1983 *Astrophys. J.*, 271, 376.

Kiplinger, A. L., Dennis, B. R., Emslie, A. G., Frost, K. J., and Orwig, L. E. 1983, *Astrophys. J. (Letters)*, 265 L99.

Knight, F. K. 1981, Ph. D. Dissertation, University of California, San Diego.

Knight, F. K. 1982, *Astrophys. J.*, 260 538.

Lampton, M., Margon, B. and Bowyer, C. S. 1976, *Astrophys. J.*, 208, 177.

Landis, D. A., Cork, C. P., Madden, N. W., and Goulding, F. S. 1982, *IEEE Trans. Nucl. Sci.*, NS-29, No. 1, 619.

Leventhal, M., MacCallum, C. J., and Watts, A. C. 1977, *Nature*, 266, 696.

Lin, R. P. 1974, *Space Sci. Rev.*, 16, 189.

Lin, R. P., and Hudson, H. S. 1976, *Solar Phys.*, 50, 153.

Lin, R. P., Schwartz, R. A., Pelling, R. M., and Hurley, K. C., 1981, *Astrophys. J.*, 251, L109.

Lin, R. P., Schwartz, R. A., Pelling, R. M., and Hurley, K. C., 1984, accepted by *Astrophys. J.*,

Ling, J. C., Mahoney, W. A., Willett, J. B., and Jacobson, A. S., 1979, *Astrophys. J.*, 231, 896.

Mahoney, W. A. 1974, Ph. D. dissertation, University of California.

Mahoney, W. A., Ling, J. C., and Jacobson, A. S. 1984, to be published in *Astrophys. J.*, 15 March 1984.

Manchanda, R. K., Bazzano, A., La Padula, D. C., Polcaro, V. F. and Ubertini, P. 1982, *Astrophys. J.*, 252, 172.

Mätzler, C., Bai, T., Crannell, C. J., and Frost, K. J. 1978, *Astrophys. J.*, 223, 1058.

Mewe, R. 1972, *Solar Phys.*, 22, 459.

Moore, R. *et al.* 1980, *Solar Flares*, ed. Peter A. Sturrock (Boulder: Colorado Associated University Press), p. 341.

Mozer, F. S., Cattell, C. A., Hudson, M. K., Lysak, R. L., Temerin, M., and Torbert, R. B. 1980, *Space Sci. Rev.*, 27, 155.

Nolan, P. L. 1982, *UCSD Technical Report*, 8215.

Pravdo, S. H. and Serlemitsos, P. J. 1981, *Astrophys. J.*, 246, 484. *Astrophys. J.*, 193, 729.

Ramaty, R. *et al.* 1980, *Solar Flares*, ed. Peter A. Sturrock (Boulder: Colorado Associated University Press), p. 117.

Ramaty, R., Lingenfelter, R. E., Kozlovsky 1982 *Gamma Ray Transients and Related Astrophysical Phenomena*, ed. R. E. Lingenfelter (New York: American Inst. of Physics), p. 211.

Ramaty, R., Murphy, R. J., Kozlovsky, B. and Lingenfelter, R. E. 1983, *Solar Physics*, 86, 395.

Ramaty, R. and Petrosian, V. 1972, *Astrophys. J.*, **178**, 241.

Rosner, R., Tucker, W. H., Vaiana, G. S. 1978, *Astrophys. J.*, **220**, 643.

Ryckman, S. G., Ricker, G. R., Scheepmaker, A., Ballintine, J. E., Doty, J. P., Downey, P. M., and Lewin, W. H. G. 1977, *Nature*, **266**, 431.

Smith, D. F., and Lilliequist, C. G. 1979, *Astrophys. J.*, **232**, 582.

Spicer, D. S. 1977a, *Solar Phys.*, **53**, 249.

Spicer, D. S. 1977b, *Solar Phys.*, **53**, 305.

Spitzer, L. 1962, *Physics of Fully Ionized Gases*, (New York: Wiley-Interscience).

Strickman, M. S., Johnson, W. N., and Kurfess, J. D. 1979, *Astrophys. J. (Letters)*, 230, L15.

Strickman, M. S., Kurfess, J. D., and Johnson, W. N., 1982, *Astrophys. J. (Letters)*, 253, L23-27.

Svestka, Z. 1976, *Solar Flares*, (Dordrecht, Holland: Reidel).

Takakura, T. and Kai, K. 1966, *Publ. Atron. Soc. Japan*, **18**, 57.

Toor, A. and Seward, F. D. 1974, *Astron. J.*, **79**, 995

Trubnikov, B. A. 1965, *Particle Interactions in a Fully Ionized Plasma*, Vol.1 (New York: Consultants Bureau).

Trümper, J., Pietsch, Reppin, C., Voges, W., Staubert, R., and Kendziorra, E. 1978, *Astrophys. J. (Letters)*, **219**,

Tucker, W. H. and Koren, M. 1971, *Astrophys. J.*, **168**, 283. L105.

Wild, J. P., Murray, J. D., and Rowe, W. C. 1954, *Australian J. Phys.*, 7, 439.

Wild, J. P., Smerd, S. F., and Weiss, A. A. 1963, *Ann. Rev. Astron. and Astrophys.*, **1**, 291.

Willett, J. B., Ling, J. C., Mahoney, W. A., and Jacobson, A. S., 1978, *Gamma Ray Spectroscopy in Astrophysics*, *NASA Tech. Mem. 79619*, ed. T. L. Cline and R. Ramaty, p. 450.

Van Hoven, G. *et al.* 1980, *Solar Flares*, ed. Peter A. Sturrock (Boulder: Colorado Associated University Press), p. 17.

Vilmer, N., Kane, S. R., and Trottet, G. 1982, *Astron. and Astro*, **108**, 306.